Mechanical Robustness
and
Hermeticity Monitoring
for
MEMS Thin Film Encapsulation

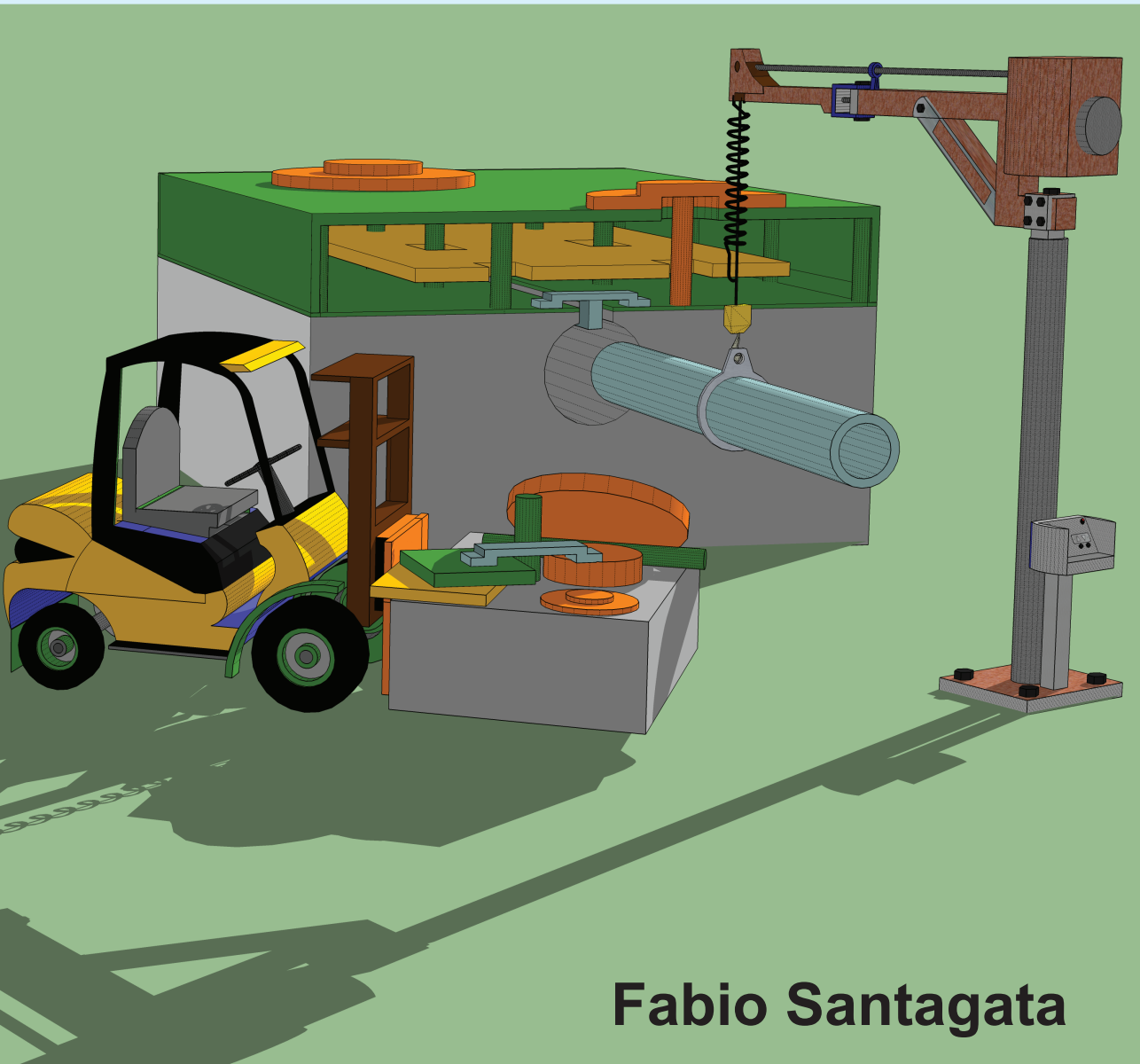

Fabio Santagata

Mechanical Robustness and Hermeticity Monitoring for MEMS Thin Film Encapsulation

Fabio Santagata

Mechanical Robustness and Hermeticity Monitoring for MEMS Thin Film Encapsulation

PROEFSCHRIFT

ter verkrijging van de graad van doctor
aan de Technische Universiteit Delft,
op gezag van de Rector Magnificus Prof. ir. K. C. A. M. Luyben,
voorzitter van het College voor Promoties,
in het openbaar te verdedigen

op dinsdag 6 december 2011 om 12.30 uur

door

Fabio SANTAGATA

Dottore Magistrale in Ingegneria Elettronica,
van Universita' degli Studi di Napoli Federico II, Italia
geboren te Napoli, Italia

Dit proefschrift is goedgekeurd door de promotor:
Prof. dr. P. M. Sarro

Samenstelling promotiecommissie:

Rector Magnificus, voorzitter
Prof. dr. P. M. Sarro, Technische Universiteit Delft, promotor
Prof. dr. ir. P. J. French, Technische Universiteit Delft
Prof. dr. U. Staufer, Technische Universiteit Delft
Prof. dr. G. Krijnen, Universiteit van Twente
Prof. dr. C. Hierold, Eidgenssische Technische Hochschule Zürich (ETH Zürich), Switzerland
Dr. ir. J. F. Creemer, Technische Universiteit Delft
Dr. H. Tilmans, IMEC, Belgium
Prof. dr. C. I. M. Beenakker, Technische Universiteit Delft, reservelid

Fabio Santagata,
Mechanical Robustness and Hermeticity Monitoring for MEMS Thin Film Encapsulation,
Ph.D. Thesis Delft University of Technology,
with summary in Dutch.

Keywords: Pirani gauge, Wafer Level Packaging, Thin Film Encapsulation.

ISBN: 978-90-8570-759-2

Printed in The Netherlands.

To Elina and Salvatore

Contents

Chapter 1

Introduction

1.1 Packaging of MEMS

Packaging of Micro-Electro-Mechanical-Systems (MEMS) is a determining factor in both the functional behavior and the production costs of the MEMS device [1]. In fact, it has not only to fulfill the same requirements of a package for Integrated-Circuits (ICs) but at the same time it has to accommodate additional functionalities that are specific to the application of the MEMS device.

Typical requirements valid for both ICs and MEMS devices concern a certain degree of protection and/or isolation. The package has to protect the device from the working environment and, at the same time, it has to protect the environment from the device itself and its operation [2]. In particular, as for the ICs, the packaging of MEMS devices may require:

- Mechanical protection to ensure structural integrity
- Electrical isolation or passivation from electrolytes and moisture
- Optical and thermal protection to prevent undesired effects on performance
- Chemical isolation from harsh environment

However, whereas there is a packaging standard for ICs, so far there is no unique and generally applicable packaging method for MEMS. In fact, each MEMS device works in a special environment and has unique operational specifications. Many MEMS devices consist of free-standing mechanical microstructures and this implies that MEMS packaging cannot follow the

procedures set by IC packaging industry. The device may not withstand the back-end processes, such as wafer dicing, wire bonding and high pressure overmolding of plastic [1].

MEMS devices often require to be hermetically packaged under a certain environment. These devices may require operation in a vacuum, at reduced pressure or in an inert ambient. In this case, the ambient of the cavity housing of the MEMS device play an important role in tuning its operating characteristics. In particular, an hermetic packaging provides

1. protection of MEMS structure from dust, humidity, corrosion, etc.
2. isolation from thermo-mechanical stress on the package (during handling, die bonding, during operation)
3. defined vacuum (reduction of damping effects, low power consumption, less temperature effects, long term stability)

To provide cost-effective solutions, the MEMS community is facing the challenge to find packaging methods applicable to a wide range of MEMS devices. So far, there are two types of MEMS packaging solutions: discrete packaging and wafer-level packaging [3].

1.2 Discrete packaging

Discrete packaging, or first-level packaging, consists of chip capsule and leads for interconnecting the chip to the outside world. Examples are ceramic, metal can or plastic molded packages (see Fig. 1.1). Cavity formation during first-level packaging is an established method that allows flexibility with respect to the composition of sealing gas and the sealing pressure. Drawbacks of this approach are the high cost of ceramic and metal can packages, and the danger of exposing the fragile MEMS device to handling and contamination during wafer dicing and subsequent cleaning [1]. Plastic packages, which are cheaper, are often not suitable for housing naked MEMS devices because of the nature of the overmolding process. In fact, during this step a plastic compound is inserted into the package exerting on the device a pressure of about 8 MPa (80 bar). This becomes critical when the device consists of free-standing microstructures.

1.3 Wafer-level packaging

The wafer-level packaging approach, or wafer-level encapsulation, consists of an encapsulation step carried out before discrete packaging, to protect

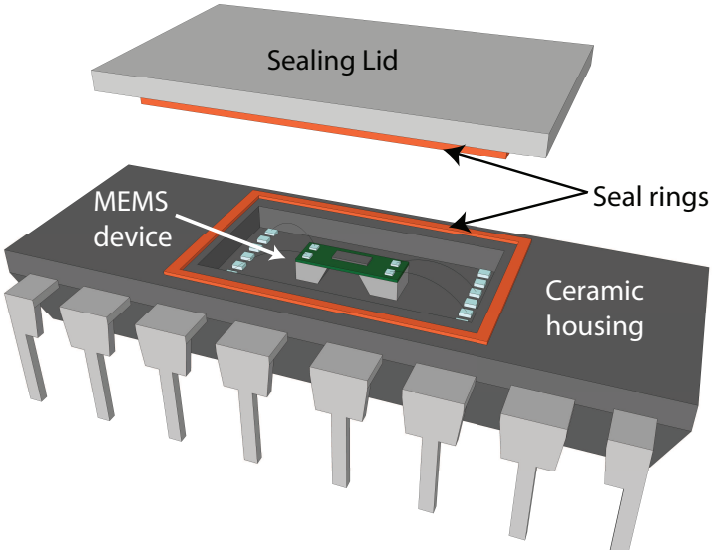

Figure 1.1: Schematic drawing of discrete packaging.

fragile moving parts during subsequent wafer processing. This approach allows the use of low-cost packaging for final encapsulation, like non-hermetic plastic overmolding. In this case, the wafer-level encapsulation has to provide the due hermeticity to the packaged device and it has to withstand the back-end processes.

Wafer level encapsulation [4] can be grouped in two categories, capping by means of wafer bonding and thin-film encapsulation (see Fig. 1.2). In the wafer bonding encapsulation [5–13], a separate substrate is bonded to the MEMS wafer to cap the MEMS components (Fig. 1.3). It is known to enable good vacuum quality (expecially for the high temperature bonding) and excellent mechanical robustness and this makes it suitable for plastic overmolding (Fig. 1.4). This is mainly due to the rather stiff cap and to the large seal ring area that goes all the way around the MEMS device. However, this leads to micropackages with rather large thickness and footprint. For small MEMS devices, such as resonators or accelerometers, this seal ring occupies too much surface of the wafer. In fact, for typical sealing processes, this seal ring has to be more than hundred microns wide all around the MEMS device.

In the thin-film approach [4] the encapsulation process is done on the same wafer where the MEMS devices are fabricated by adding extra thin-film processing steps. Sealed cavities are created by surface micromachining.

In particular, after the MEMS device is fabricated, a sacrificial layer and a capping layer are deposited on top of it (see Fig. 1.2). After the sacrificial layer is removed through the etch holes in the capping layer, the etch holes are sealed by thin-films deposited on top of the capping layer under appropriate pressure conditions.

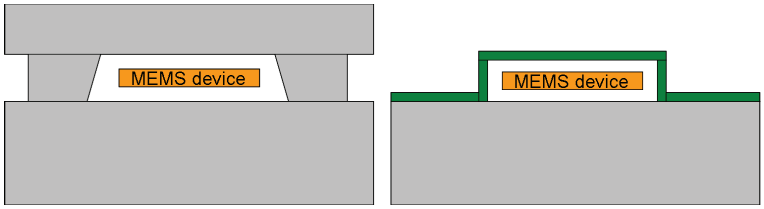

Figure 1.2: Schematic drawing of wafer-to-wafer bonding and thin-film encapsulation.

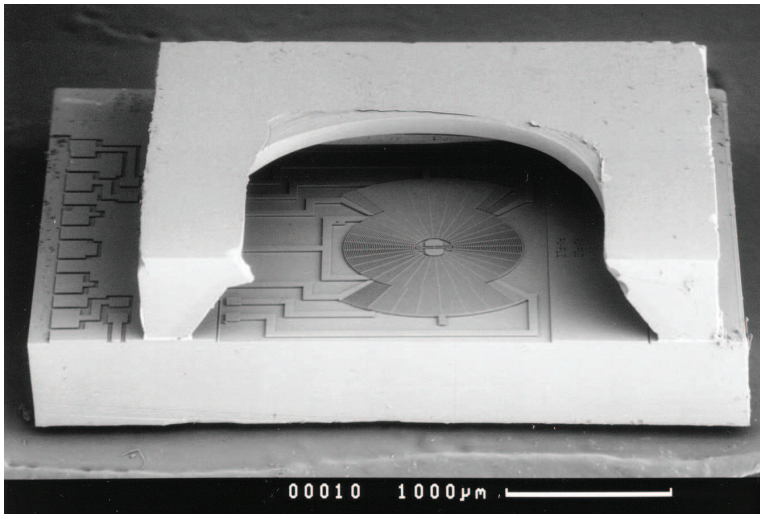

Figure 1.3: SEM cross section of a packaged automotive gyroscope from Bosch using glass frit bonding [14].

1.4 Thin-film encapsulation

Compared with hybrid wafer bonding, monolithic thin-film encapsulation has several advantages that render it a much simpler technology. For this

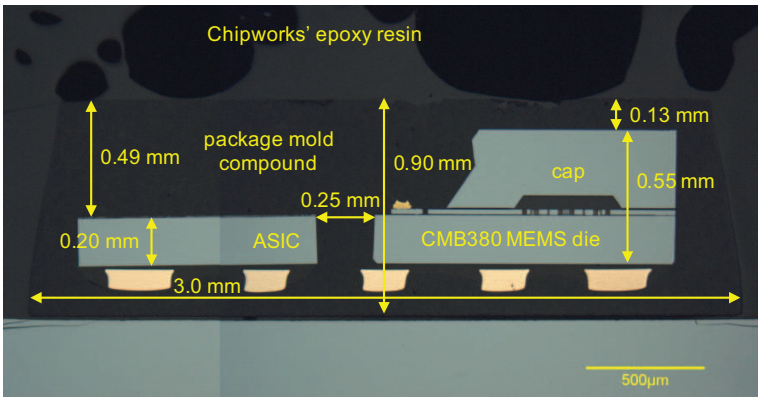

Figure 1.4: Bosch MEMS accelerometer packaged by plastic overmolding [15].

reason it is also more cost effective at the same performance. Technological advantages of thin-film encapsulation are [16]:

1. No need for a second substrate
2. It employs thin-film batch fabrication processes, avoiding the need for aligning two wafers and the challenges of bonding on processed (i.e., not smooth) surfaces.
3. It produces much lower topography, allowing for post-encapsulation processes for additional MEMS or IC steps.
4. It requires considerably less chip area because there is no need of seal ring when compared to the bonding approach.

The thin film encapsulation process allows the die to be separated with dicing cuts that are within tens of microns of the MEMS device. This opportunity for reduced area has allowed fabricating extremely small resonators and inertial sensors, opening the door for new applications, such as in catheters and in cochlear implants. This reduction in device area also has an important cost-related benefit. Since more devices can be obtained from the MEMS process wafer, the cost/device can be significantly reduced. This cost reduction can overcome the added cost of the encapsulation steps, depending on the details of the process and the device design. There is an added benefit to this encapsulation process: there are mechanical design opportunities within the thin-film encapsulation which can reduce the cost

of the secondary packaging. One example of this opportunity is the construction of structures that can ensure the thermal and mechanical isolation of the device from the package.

However, thin-film encapsulation poses a number of challenges, comprising the process compatibility, thermal budget, mechanical robustness and hermeticity monitoring. Furthermore, these issues are closely interrelated.

The kind of deposition process and the choice of the sacrificial layer are strictly linked to the thermal budget of the MEMS device itself. This means that encapsulation schemes that hermetically seal devices at the wafer level must be performed at a temperature that is compatible with the MEMS device inside the cavity. Due to the wide variety of MEMS technologies, this thermal requirement can vary between and 100°C and 1000°C. For this reason, thin film capping methods are generally divided in high-temperature ($> 400°$ C) and low-temperature thin-film encapsulation ($< 400°$ C). Also, the quality of the vacuum inside the package and its robustness to external loads depend on the type of processing techniques and materials used for the encapsulation.

1.5 Review of thin film encapsulation techniques

Several solutions to thin-film encapsulation have been presented in literature [11, 16–29]. Their focus is on the choice of materials for sacrificial, capping and sealing layers in order to meet the requirements of thermal budget and vacuum levels.

High temperature processes provide better vacuum but cannot be used in the cases of thermal budget limitations. Several high temperature packages based on Low Pressure Chemical Vapour Deposition (LPCVD) have been demonstrated [19, 20, 30, 31]. In [19] a free-standing filament has been encapsulated inside a LPCVD low-stress silicon nitride cavity to create a micro incandescent light source. A similar technique has been employed in [20] to seal a micro comb-drive resonator; whereas in [30] LPCVD polysilicon has been used to seal a diode device in a cavity and in [18] a resonator has been encapsulated by LPCVD silicon nitride. In [16, 25, 27, 28] a high temperature encapsulation process has been developed for inertial sensors and resonators. It has proven to provide a hermetic vacuum sealing with long-term stability by depositing a capping layer in an epitaxial polysilicon growth chamber. Because of the thickness of the capping layer (around 50 μm), this package can withstand the overmolding pressure. The thick polysilicon seal layer also helps to prevent diffusion of atmospheric contami-

nants. In [29,32] a high temperature thin-film encapsulation using polycrystalline silicon-germanium (poly-SiGe) as the base material, complemented with a metal seal, has been presented. Packages with a cavity pressure below 0.3 mbar have been demonstrated on a SOI-based torsional-mode Si resonator.

Low temperature thin-film encapsulation has also been presented in literature [21–23, 26, 33–36]. Low temperature encapsulation processes point not only to maximize the integration of MEMS devices in the IC processing, but also to package MEMS devices that cannot withstand a high temperature process. For instance, high temperature encapsulation methods do not suit such applications as RF MEMS, where aluminum is frequently used to build the MEMS devices and cannot withstand any high temperature processes. In [21] electroplated nickel film has been used as capping layer. In Ref. [22, 23] a Plasma Enhanced Chemical Vapor Deposition (PECVD) of SiN/SiO has been used for the capping layer, whereas in [35] PECVD SiC was used. In [36] an alumina sealing layer was deposited by sputtering. In the low temperature encapsulation approach also the sacrificial layer needs to be deposited at low temperature. Organic materials, which can be easily removed in oxygen plasma avoiding stiction, are an interesting choice. Liquid polymers like photoresist or thermally decomposable polycarbonates have been suggested [21, 22, 26], but spin coating of the materials on fragile structures and the thermal stability are crucial for process integration. Moreover the complete etching of these materials has to be ensured because the reaching of a good vacuum sealing can be highly affected by the presence of organic residues inside the cavity. This is the main disadvantage related to using organic materials as sacrificial layer.

A common issue to be addressed for thin-film encapsulation regards the sacrificial etching holes. Opening large holes in the encapsulation layer above the device area is not preferable, because a significant amount of sealing material will deposit on the device surfaces inside the cavity, changing the device characteristics. For this reason small access holes are preferable if allowed by lithography. In other cases, lateral etch channels are used although it takes a longer time to remove the sacrificial layer from the cavity. Another solution has been proposed in [24, 26, 33, 34, 37], where a free-standing porous membrane has been used as capping layer. By using a porous membrane, the sacrificial layer can be removed through the nanopores, which can be later sealed by a further deposition step.

Although several solutions have been presented in literature for more than 25 years, the thin-film encapsulation approach can still be considered in a research phase. In fact, despite the anticipated advantages over the hybrid approach using wafer-bonding, mechanical robustness, hermeticity and

process integration of thin-film encapsulation should be addressed before this approach can actually be extensively used in industry.

1.6 Research objective

This thesis addresses mechanical robustness, hermeticity monitoring and process integration for thin-film encapsulation. First, it provides the designer of thin-film encapsulation with guidelines for dimensioning of thin-film packages and Pirani vacuum sensors to be integrated into the packages. Then, it presents a new tube-shaped Pirani gauge that combines low detection limit and a strongly reduced footprint. Such sensor is integrated into a thin-film encapsulation process to evaluate its hermeticity. This thesis also provides a new sealing technique for MEMS thin-film encapsulation employing the bimorph effect and gives examples of process integration of the presented thin-film approach with different MEMS devices.

1.6.1 Mechanical robustness

Mechanical robustness of the thin-film packages is an important concern because a few microns thick capping layer does not make the packages strong enough for the back-end process. Pressures up to 80 bars are expected, especially during the overmolding.

Several solutions to thin-film encapsulation have been presented in literature [11,16,19–28,33,34]. However, their focus is on the choice of materials for sacrificial, capping and sealing layers in order to meet the requirements of thermal budget and vacuum levels whereas their mechanical robustness has not been tested. Indeed, most of the thin-film packages from literature consist of a single square or circular plate clamped on a wall, designed to withstand $1{\cdot}10^5$ Pa (atmospheric pressure) of differential pressure. They are not suitable for overmolding ($80{\cdot}10^5$ Pa).

In this thesis a thin-film encapsulation approach is presented. It is meant to provide MEMS devices with hermetic encapsulation that is sufficiently strong for overmolding. A flat slab structure supported by columns is considered as basic geometry for the mechanical model. In order to verify the model validity, thin-film packages are fabricated using silicon nitride as material for the capping layer. The packages are tested at different pressures up to 12.5 MPa. Moreover, the packages are carried through grinding, dicing and overmolding steps.

1.6.2 Hermeticity

To test the hermeticity of the thin film approach, the vacuum levels inside the packages are usually monitored over extended periods. Long-term stability and *in situ* pressure measurement of traditional platform packages are often evaluated using helium leak-rate tests and quality factor measurements from resonators integrated in the packages [38]. However, leak test based techniques require expensive equipment. They cannot monitor small changes inside wafer-level micropackages because they are generally limited to a leak measurement resolution of 10^{-12} Pa m^3/s [39, 40]. Quality factor measurements based on resonators are limited by sensor drift due to material instabilities, cannot reliably resolve small pressure changes, and are difficult to calibrate. Compared to resonators, Pirani gauges are easier to calibrate and test and usually have higher pressure sensitivities [41].

In this thesis, a new micromachined Pirani gauge is introduced. It that combines low detection limit and a strongly reduced footprint. It consists of a tube-shaped resistor that is buried in the silicon substrate.

Such Pirani gauge is integrated inside micro-packages sealed by PECVD silicon nitride. The vacuum level of the micro-packages is measured and the long-term hermeticity achieved with PECVD SiN is monitored over time.

Finally, a new fabrication technique for MEMS thin-film encapsulation that allows a LPCVD sealing without undesirable deposition on the inner surface of the microcavity is presented. In addition, this technique allows to perform the encapsulation step under arbitrary pressure conditions.

1.6.3 Process integration with different MEMS devices

As demonstrators a MEMS electron source and an infrared detector are encapsulated by means of the presented thin-film approach. The encapsulation design is performed together with the design of the MEMS device to be encapsulated. The results show how the developed thin-film approach can be employed for different applications.

1.7 Structure of the thesis

In this thesis, the issues of mechanical robustness, hermeticity and process integration of thin-film encapsulation are addressed.

Mechanical robustness of thin film encapsulation is analyzed in chapter 2, where a mechanical design and characterization of a thin film encapsulation approach is presented. By designing the package as a flat slab structure supported by columns gives the possibility to fabricate packages with very

thin capping layers that are robust enough for withstanding back-end processes.

In chapter 3 a new analytical model for the design of MEMS Pirani gauge is presented. This model expresses the pressure range as a closed-form analytical function of the design variables like geometry and biasing. This makes possible the design of the sensor for the specified pressure range required by the package. A Pirani gauge designed according to the presented model is fabricated and characterized in order to verify the validity of the model.

A new 3D micromachined Pirani gauge is introduced in chapter 4. It combines vacuum measurements with low detection limit with a strongly reduced footprint. These properties make it very suitable for vacuum measurement of thin-film packages.

In chapter 5 hermeticity of the thin film approach is studied. We integrated the presented 3D Pirani gauge inside SiN thin-film micro-packages. Packages containing Pirani tubes are designed and fabricated and their vacuum level is monitored.

In chapter 6 a new sealing technique for MEMS thin-film encapsulation is discussed. It allows to perform the encapsulation step under arbitrary pressure conditions without unwanted deposition of the sealing material on the device surface. This novel sealing technique is compatible with most of the thin-film encapsulation approaches. Microcavities are designed and fabricated to validate the proposed concept. Package are encapsulated and no deposition is observed inside the microcavity encapsulation.

Chapter 7 contains two examples of process integration of the thin-film encapsulation with two different devices: a MEMS electron source and an infrared detector.

Finally, the conclusions and some suggestions for future research are given in chapter 8.

Chapter 2

Mechanical Design of Thin Film Encapsulation

2.1 Introduction

As discussed in the introduction, besides the advantage of integrating the MEMS device and its package on a single substrate, the thin-film approach is considerably more efficient in terms of chip area compared to the bonding approach. However, the mechanical robustness of the thin-film packages is an important concern. Fabricating the capping layer of the packages by means of thin-film depositions (only a few microns thick) makes the packages rather fragile during the back-end process. Pressures up to 80 bar are expected, especially during the overmolding.

In all the thin-film packages presented in literature particular attention has been paid on the hermetic vacuum sealing of the packages whereas their mechanical robustness has not been evaluated. Most of them consist of a single square or circular plate clamped on a wall, designed to withstand 100 kPa (1 bar) of differential pressure [11, 19, 20, 22–24, 26]. They are not suitable for being placed into a overmolding plastic package.

In [16, 25, 27, 28] a high temperature encapsulation process based on a thick polysilicon capping layer has been developed for inertial sensors and resonators. Because of the thickness of the capping layer (around 50 μm), this package can withstand the transfer molding pressure. In that case only the maximum deflection of the cap was considered to dimension the package.

The thin-film approach is often preferable to the thick epi-poly encapsulation because can be applied later in the fabrication process and it is suitable for applications when lower thermal budget is required. Further-

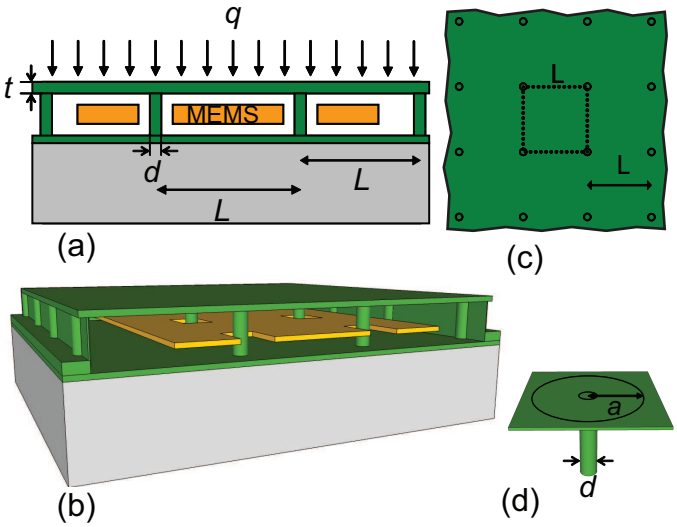

Figure 2.1: Thin-film package geometry consisting of a square plate with supporting columns. a) Package cross section. b) 3D sketch of the package. c) Package topview. d) 3D sketch of the column.

more, it leaves more freedom for the choice of the capping layer material that can suit to the application (optically transparent, low thermal conductivity, metal capping layer, etc.). However, for designing thin-film packages (a few microns thick), yielding of the capping layer should also be considered [42].

Here we model a thin-film encapsulation approach meant for withstanding the high mechanical loads during the back-end processes like plastic overmolding [43]. The proposed design solution consists of a capping layer supported by circular columns (Fig. 2.1a-d). This allows to strongly decrease the thickness of the capping layer compared to solutions where the capping layer is only supported by the perimetral walls.

The design of the package has to be done together with the design of the device (Fig. 2.1a-b). During the MEMS device design, it is necessary to reserve some space for placing the required columns. This is possible in many MEMS device. In [25] posts have been used in the encapsulation of a lateral piezoresistive accelerometer. In [44] a thin-film encapsulation based on distributed pillars is used to package an electron source. An array of pillars distributed around the silicon tips ensured the required robustness of the package (see chapter 7). For the encapsulation of an IR detector, columns were positioned between the thermocouple bridges and around the

Pirani heater bridge [45](see chapter 7). For accelerometers and gyroscopes often the space for the columns can be naturally found between the comb-drivers beams of the device. Devices based on microheaters offer space for the columns around the heater. In [24] for instance, a Pirani gauge is wrapped up into a serpentine. The space around the serpentine can be used for placing the columns. In [40] a ladder shaped Pirani gauge is presented. Columns could be placed between the rungs of the ladder.

In this chapter we first present a mechanical model for the package design, which considers both the maximum allowed deflection and the yield strength. Packages with different sizes were designed and fabricated according to the presented model. The packages were sealed under vacuum (see chapter 5 for the hermeticity monitoring). Pressure tests were performed on the packages to verify the validity of the mechanical model. Finally, the fabricated packages were demonstrated to survive a commercial grinding/dicing/overmolding process.

2.2 Mechanical Model

Most of the thin-film encapsulation solutions found in the literature consist of a single square or circular plate clamped on a wall. Most of them [11, 19, 20, 22–24, 26] would not survive the transfer molding pressure unless a very thick capping layer is used [21, 27].

Here we propose a design consisting of a capping layer supported by circular columns (Fig. 2.1a-d). With this geometry, the thickness of the capping layer can be strongly decreased compared to capping layer only supported by the perimetral walls. To study the mechanical behavior of such structure, a flat slab supported by columns is considered as basic geometry for the mechanical model. The slab consists of a planar distribution of square panels (Fig. 2.1c) and if the dimensions of the slab are large in comparison with the distances L between the columns, the bending in all panels, which are not close to the boundary of the plate, may be assumed to be identical, so that the problem can be limited to the bending of one panel only.

The model expresses the column diameter d and the capping layer thickness t as a function of the distance between the columns L, the capping material properties, and the distributed load q (Fig. 2.2).

$$(d, t) = f(L, q, d, \sigma_t, \sigma_c, D), \tag{2.1}$$

where σ_c, σ_t are the compressive and the tensile strengths of the capping

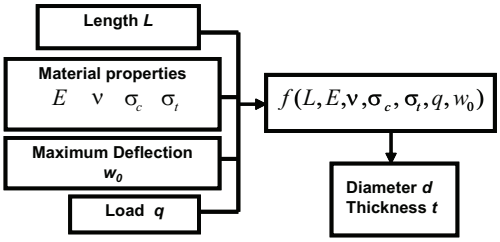

Figure 2.2: Mechanical model for thin-film encapsulation. The column diameter d and the capping layer thickness t are function of the distance between the columns L, the capping material properties, and the distributed load q.

material, respectively and D is its flexural rigidity, given by

$$D = \frac{Et^3}{12(1-\nu^2)}. \tag{2.2}$$

where E is the Young's modulus and ν is the Poisson's ratio. The distance between columns L is usually determined by the size of the encapsulated device. When the package is loaded the capping layer deflects and if the stress overcomes the material strength it breaks and can crash on the encapsulated device. The presented model takes both these failure mechanisms into account. In fact, the expression of the deflection of the capping layer and the yield strength criterion constitute the basic equations of the model. In the following subsections the relevant stresses and the deflection of the capping layer are calculated (Fig. 2.3).

2.2.1 Deflection and stress in the center of a plate

When applying a pressure difference on the capping layer, it deflects according to the plate equation [46]. In the case of a slab supported by equidistant columns, with the assumption of small deflections ($w < 0.3t$) and if the dimensions of the plate are large in comparison with the distances L between the columns, the expression for the deflection w_0 and the stress σ_0 at the middle of each panel are (Fig. 2.4a)

$$w_0 = \frac{\alpha q L^4}{D}; \tag{2.3}$$

$$\sigma_0 = \beta \frac{(1+\nu) q L^2}{t^2} \tag{2.4}$$

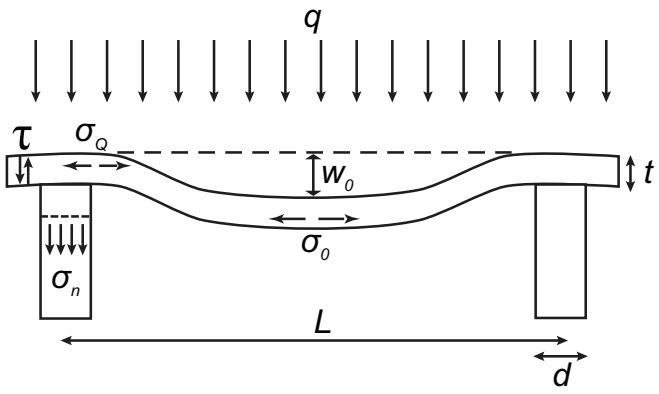

Figure 2.3: Stress components and the deflection of the capping layer taken into account in the mechanical model.

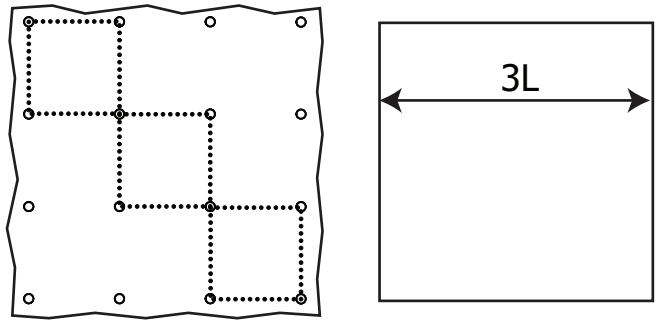

Figure 2.4: Comparison between a slab with supporting columns (a) and a square panel clamped on all the edges (b).

where $\alpha = 0.00581$ and $\beta = 0.1655$ [46].

There is a clear benefit in terms of deflection and stresses in using the column approach in comparison with a conventional thin film encapsulation that does not make use of columns (Fig. 2.4). To evaluate the deflection and the stresses for a package without columns a square-panel geometry clamped on all the edges and subjected to an uniform pressure q is considered (Fig. 2.4b). In this case the expression for the deflection and the stress at the middle of the plate are the same as for the case with the columns (Eqs. 2.3, 2.4). However, L coincides with the length of the square side and not with the columns pitch and the constants α and β have different values ($\alpha = 0.00126$ and $\beta = 0.0513$, [47]). By adding four columns in the middle of the plate (Fig. 2.4) the pitch becomes one third of the side length of the square package. According to Eqs. 2.3 and 2.4, the deflection and the stress at the center of the plate would be approximately one order of magnitude smaller.

A first condition on the capping layer thickness is derived from the limitation on the deflection. Since the maximum deflection is achieved in the center of the panel, the equation for the thickness can be derived from Eq. 2.3. By solving this equation the following expressions for the capping layer thickness is obtained:

$$w_0 < w_{max} \quad \Rightarrow \quad t > \sqrt[3]{12\frac{\alpha\, qL^4(1-\nu^2)}{Ew_{max}}} \tag{2.5}$$

where the maximum allowed deflection w_{max} is related to the distance between the cap and the encapsulated MEMS device.

2.2.2 Normal stress on the column

In order to calculate the normal stress on the column due to vertical load, a basic square cell with four columns is considered (Fig. 2.5). The area L^2 of the plate is supported by four quarters of column. From static's laws, the vertical forces applied over the plate qL^2 result in the following normal compressive stress in the columns:

$$\sigma_n = 4\frac{qL^2}{\pi d^2} \tag{2.6}$$

We use this expression to choose the minimum value of the column diameter which prevents the collapse of the column, i.e.:

$$d_{min} = f(L, q, \sigma_c) = 2\sqrt{\frac{nqL^2}{\pi\sigma_c}} \tag{2.7}$$

where σ_c is the compressive strength of the material and n is a safety factor.

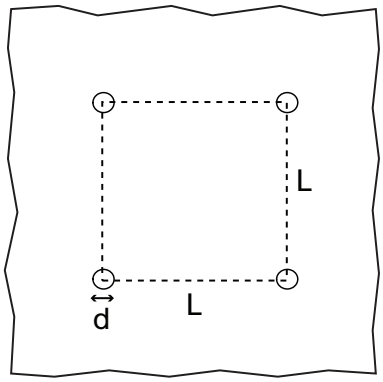

Figure 2.5: Basic cell considered for the calculation of the normal stress on the column.

2.2.3 Bending and shear stress around the column

Around the column the slab experiences bending stress. The larger the deflection, the larger is the bending stress around the column. In first approximation it can be calculated by assuming the reactive forces to be distributed uniformly over the area of a circle representing the cross section of the column [46]. This assumption is needed otherwise the bending moments at the center of the pillar become infinitely large. The derived expression according to the customary theory for the stresses σ_{CT} on the columns is the following

$$\sigma_{CT} = \frac{3}{2} \frac{qL^2 (1+\nu) \ln\left(\frac{0.62\, k\sigma_c}{q}\right)}{t^2 \pi} \tag{2.8}$$

A better estimate of this contribution is obtained by considering quasi-rigid connection between the column and the plate [46, 47]. This approach considers that the portion of the plate around the column and inside a circle of radius $a = 0.22L$ is in the state of an annular plate simply supported along the outer circle and clamped along the inner one. The reason is that the bending moments in the radial direction practically vanish along the circle of radius a. We used the solution presented in [48] to calculate the radial and tangential components of the bending moment. The tangential contribution M_t of the bending moment is always smaller than the radial

one M_r and for this reason its value will not be considered here; M_r is calculated as follows:

$$M_r = \frac{1}{8}\frac{(1-k^2)(3+\nu-(1-\nu)k^2)+4(1+\nu)k^2\ln k}{1+\nu+(1-\nu)k^2+C_b\frac{D}{b}(1-\nu^2)(1-k^2)} \tag{2.9}$$

and $k = b/a$; where b is the inner radius of the annular plate coinciding with $d/2$ and C_b is the value of flexibility [17] given by the following expression:

$$C_b = 5.306\frac{1-\nu^2}{Et^2} \tag{2.10}$$

Considering that $\sigma = 6M/t^2$ [46] and taking into account that $k^2 << 1$, the radial bending stress around the column is calculated as follows

$$\sigma_Q = \frac{3}{4}\frac{qL^2(3+\nu)}{t^2(1+\nu+\frac{1}{12}\frac{CbEt^3}{b})} \tag{2.11}$$

The last stress component to be considered is the shear stress τ around the columns (Fig. 2.3) [47]. It is given by $\tau = 0.613\frac{qL}{2\pi t}$. However, it is very small compared to the bending stress σ_Q.

2.2.4 Capping layer thickness

Now that the different modes of failure have been identified, we need to evaluate which limit they impose on the column diameter d and the plate thickness t. The calculation requires some data from the device design of which the encapsulation is part. The maximum tolerable deflection of the capping layer w_0 and the distance between the columns L depend on the geometry of device to be encapsulated. The other parameters like the ultimate strength, the Young's modulus and the Poisson's ratio are defined by the material chosen for the capping layer.

In this work, silicon nitride has been chosen as capping material because it has a rather high tensile strength and a good gas tightness [49, 50]. The capping layer has to be thick enough to ensure that the package can withstand the loads during the back end processes. To calculate the minimum capping layer thickness, a yield criterion has to be chosen. SiN is a brittle material, so the most suitable yield criterion is the Coulomb-Mohr criterion [47]. It states that the material collapses when the first (tensile) or the third (compressive) principal stress reaches the tensile or compressive strength of the material in a certain point within the plate, respectively. The maximum compressive stress is acting on the columns (see Eq. 2.3). By choosing the right size for the diameter of the columns, according to

Table 2.1: Column distances L and column diameters d for all the designed packages

L [μm]	d [μm]
20	2, 4, 6
40	4, 6, 8, 10
60	4, 8, 12, 16
80	8, 12, 16, 20
100	10, 20, 28

Eq. 2.5, the stress on the column does not reach the compressive strength limit. Regarding the tensile stress, its values at the center of the panel is lower than the value reached around the columns. In fact, comparing Eqs. 2.4 and 2.9, it is possible to evaluate that the bending stress around the columns is always about 20 times larger than the tensile stress at the center of the plate. For this reason the minimum value for the capping layer thickness has to be calculated by solving Eq. 2.9:

$$\sigma_Q < \frac{1}{n}\sigma_t \quad \text{implying that} \quad t > \frac{L}{2}\sqrt{\frac{3nq(3+\nu)}{\sigma_t(1+\nu)}} \tag{2.12}$$

where n is a safety factor. The minimum thickness value has to be chosen between those two values given by the deflection at the center of the plate (Eq. 2.4) and the one calculated with the yield strength criterion (Eq. 2.12). However, in most practical cases, the yield strength criterion leads to a more strict condition on the capping layer thickness than the one related to the maximum plate deflection.

2.3 Design and Fabrication

The presented model provides rules for the mechanical design of thin-film encapsulation that makes use of supporting columns. In particular it provides the designer with the minimum columns diameter and the minimum capping layer thickness needed to design a package that can stand a certain uniform pressure. This information is contained in the Eq. 2.7 and Eq. 2.12. To verify the model validity, arrays of square packages with and without columns were designed and fabricated (Table 2.1). In the array of square packages without columns the span is ranging between 20 and 200 μm with steps of 20 μm. Packages with columns instead vary for columns diameter and columns distance. For all the packages the capping layer thicknesses varies from 3 μm to 7 μm. The geometry of the square

Table 2.2: Young's modulus E, Poisson's ratio ν, intrinsic stress σ_i and tensile strength σ_t of SiN [50, 51]

E [GPa]	ν [-]	σ_i [GPa]	σ_t [GPa]
329	0.3	0.16	6

package supported by columns is depicted in Fig. 2.1. Columns have been included also on the sidewalls of the package. This has been done to obtain a symmetric stress distribution around the columns in the middle and simulate an infinite column array. In fact, if columns are not placed also on the sidewalls, an asymmetric deflection is indeed present on the panels. This is illustrated in Fig. 2.6 by means of a finite element analysis (FEA) simulation. The simulation compares the deflection and stress distribution for the two cases of packages with and without columns also on the sidewalls. The result shows that if those columns are not placed also on the sidewalls, the deflection of the plate is larger on the outer part of the packages and the four columns in the middle are asymmetrically loaded (see Fig. 2.6). By including the columns on the square edges and the corners, these stresses are significantly decreased and the package can be treated as a infinitively extended package, e.g. the contribution of the perimetral walls can be neglected. This problem could also be resolved by increasing the space between the perimeter walls and the last column ring.

Only two or three masks are needed to fabricate the packages. The first mask is used to etch patterns in the sacrificial layer to define the pillars and the walls. Since pillars and perimetral walls are defined by the same mask, adding columns does not add any extra steps (and thus cost) to a conventional thin-film encapsulation approach which does not make use of columns. A second mask is used to etch the access holes on the capping layer to perform the sacrificial etching. And finally, a third mask can be used if it is necessary to confine the plugging layer only to the sacrificial holes.

The properties of the capping layer are influenced by the kind of deposition process. PECVD SiN (deposited at 400°C) has been used for capping the low temperature packages and a stack of LPCVD SiN (deposited at 850°C) and PECVD SiN for the high temperature packages (Fig. 2.7). The strength of both high and low temperature SiN layers have been investigated. The residual stress σ_i of the capping layer was measured on test wafers with the wafer curvature method. The other SiN parameters like Young's modulus, Poisson's ratio and tensile strength were measured in [50] and are listed in Table 2.2.

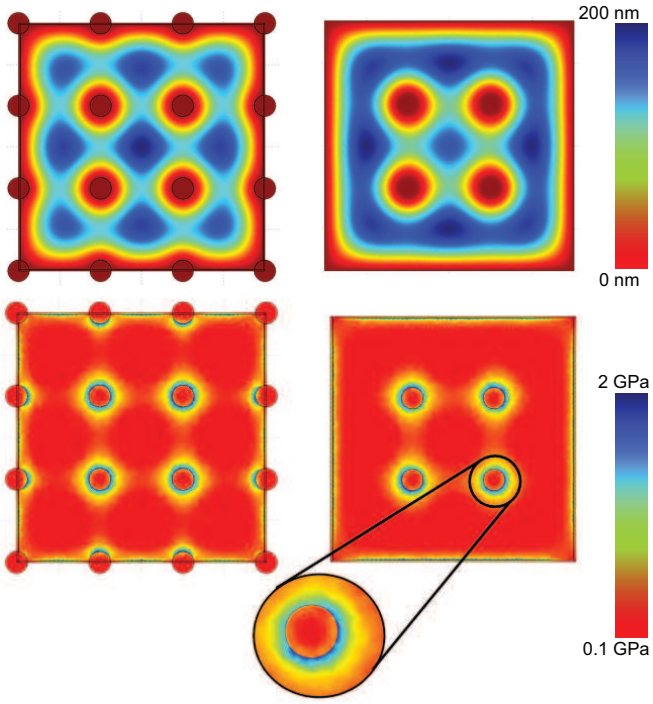

Figure 2.6: FEA simulations of the stress achieved for square panels with and without columns along the perimetral walls. The package with columns on the sidewalls show a more symmetric deflection and stress distribution.

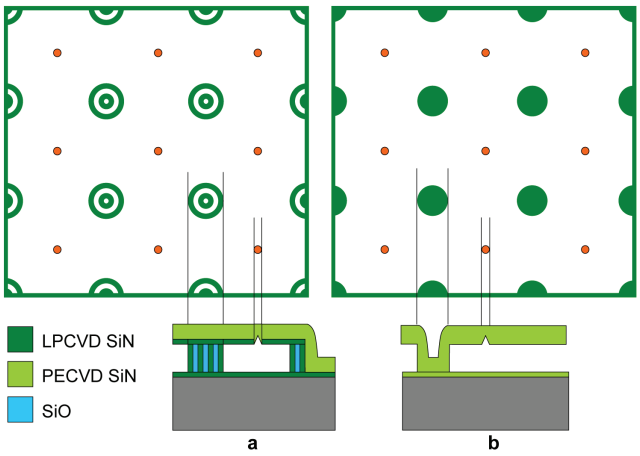

Figure 2.7: Top view and cross section for thin-film encapsulation processes. a)High temperature. b)Low temperature.

2.3.1 High Temperature Packages

The manufacturing process for the high temperature packages (Fig. 2.8, left side) started with a 500 nm silicon nitride deposited by LPCVD to define the floor of the package. Then, a 2.5 μm silicon oxide sacrificial layer was deposited by PECVD. A lithographic step was then performed and the trenches for walls and pillars were etched into the sacrificial layer by Reactive Ion Etching (RIE). Pillars and walls were defined by means of a LPCVD deposition of SiN in the trenches.

To fabricate solid columns, the trench in the sacrificial layer should be filled in completely. Since this is not possible for columns with too big diameters due to limitation in the deposition rate of the process, the columns were made with consecutive rings etched in the silicon oxide. The silicon oxide in the inner rings is not etched away during the sacrificial etching because it is protected by the outer ring of silicon nitride. A LPCVD SiN mechanical layer (1 μm thick) was deposited in the trenches. The access holes were opened on the capping layer by a RIE etching step. The releasing of the structure was performed in BHF 1:7 solution for 150 minutes. Once the sacrificial etching was finished, the sealing was done by a 1 μm PECVD SiN. The deposition was made at 400°C under a pressure of 350 Pa with a gas composition of $N_2/SiH_4/NH_3$. This would suggests that the initial pressure inside the packages is around 180 Pa at room temperature (see

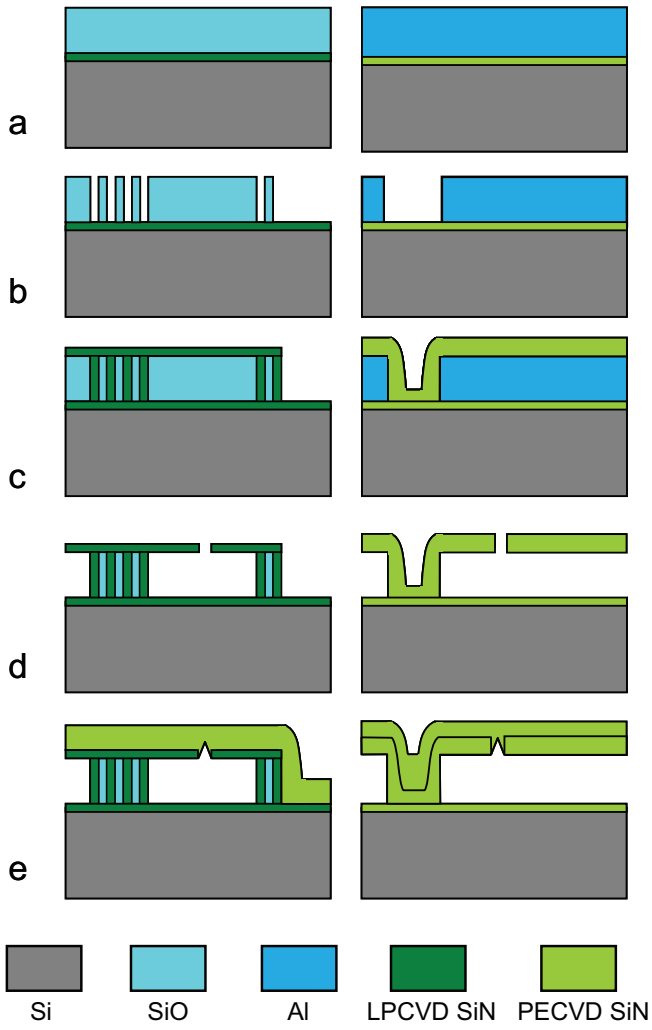

Figure 2.8: Schematic flow-chart for the high (left) and low (right) temperature thin-film encapsulation processes. a) Sacrificial layer deposition. b) Trench etching defining columns. c) Capping layer deposition. d) Etching of the access holes and sacrificial etching. e) Sealing layer deposition.

chapter 5 for the hermeticity monitoring of this encapsulation approach).

In order to get different values for the capping layer thickness, an additional PECVD SiN step is necessary to increase the thickness of the packages up to the desired value (see Table 2.3 and Fig. 2.9). Fig. 2.10 shows the columns with their concentric rings and the plugged access holes.

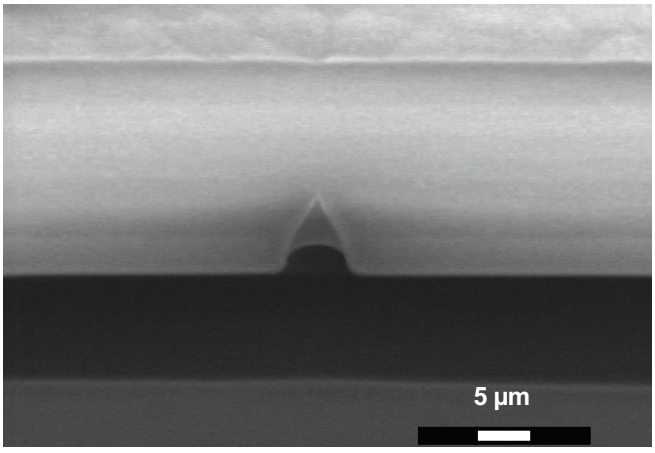

Figure 2.9: SEM cross-section of a high temperature package where a plugged sacrificial hole is visible. The capping layer consists of stack of two layers: LPCVD SiN (1 μm) and PECVD SiN (5 μm).

2.3.2 Low Temperature Packages

For the low temperature packages the fabrication process is similar (Fig. 2.8, right side). Aluminum deposited by sputtering is used as sacrificial layer, whereas SiN deposited by PECVD is employed as capping layer. The sacrificial aluminum layer was etched in a potassium hydroxide (KOH) solution. The columns in this case are not defined by concentric rings as for the case of LPCVD SiN packages. In fact, it is difficult to fill completely the columns trenches by means of PECVD SiN deposition since it is not as conformal as the LPCVD SiN. For this reason, the columns are defined by a single ring, and have more the shape of a hollow cylinder (Figs. 2.11-2.12).

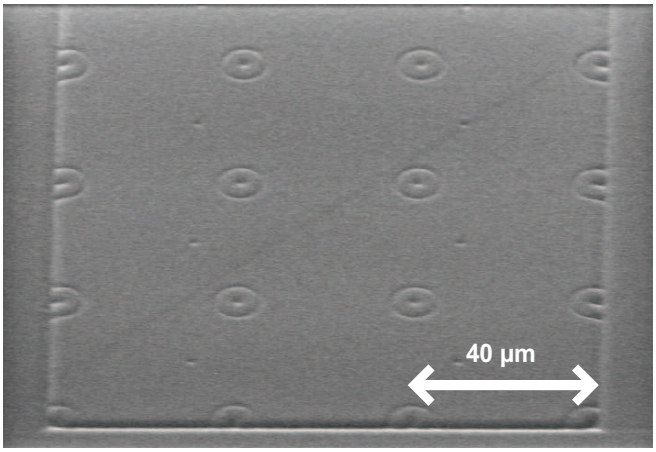

Figure 2.10: SEM topview of the high temperature package. Columns consist of concentric rings.

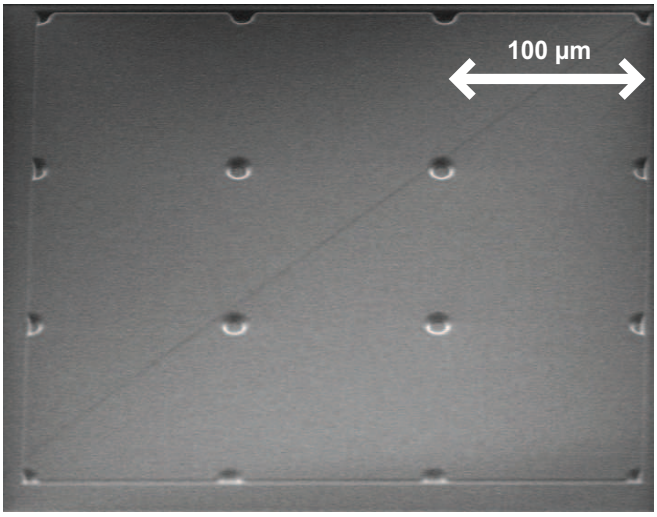

Figure 2.11: SEM topview of the low temperature package. Columns have a cylindrical shape.

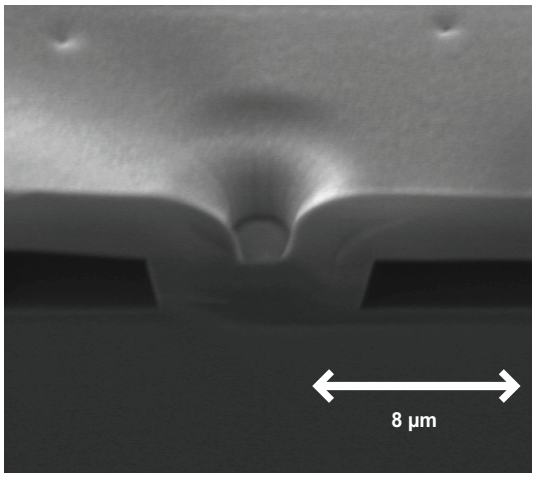

Figure 2.12: SEM cross-section of a column of a low temperature package.

Table 2.3: List of the samples

Package	High Temperature	Low Temperature
Thickness [μm]	3, 5, 6	4, 5, 7
Load [10^5 Pa]	25, 50, 75, 100, 125	25, 50, 75, 100, 125

2.4 Measurement Set-up

2.4.1 Uniaxial Loading

First, a pressure test at wafer level was performed by means of a bonding machine in order to evaluate the compressive strength of the SiN. The wafer with the packages to be tested was placed on the bottom and a bare silicon wafer was placed on the top. To prevent stress concentration, a 3 μm layer of photoresist is applied on top of our samples to better distribute the load all over the surface. Photoresist has been chosen due to its low Young's modulus (about 3-5 GPa). The maximum force that can be applied by the bonding machine (AML AWB-04) is 15 kN.

2.4.2 Hydrostatic Loading

A set-up for hydrostatic pressure tests has been assembled in order to characterize the mechanical robustness of the packages during overmolding. The setup consists of a pressure vessel with a pressure sensor and an external

hydraulic press (Fig. 2.13). The pressure vessel consists of a stainless-steel piston-cylinder system with a diameter of 1.8 cm. The samples containing the fabricated packages are placed inside the pressure vessel. The cylinder was then filled with oil. Samples containing high and low temperature packages and with different capping layer thickness were tested at different hydrostatic pressures (25, 50, 75, 100 and 125 $\cdot 10^5$ Pa). All the tested samples are listed in the Table 2.3. During the pressure test, the force is applied on the piston of the pressure vessel by means of a hydraulic press and it is measured by an external pressure sensor.

2.4.3 First-level Packaging

The packages were tested under a commercial first-level packaging process, at NXP Semiconductors, in a process developed for MEMS devices. It consists of wafer thinning, dicing, die-attaching and overmolding. To perform the wafer thinning, the wafer was hold on a vacuum chuck and a two layer foil were applied to the front side of the wafer. The wafer thinning was then performed on the back side. When the thinning was finished, the tape was removed and dicing and overmolding were then performed.

The overmolding process consists of inserting the leadframe and the die in the mold. The mold was then put in the machine and clamped between two hot plates at 180°C. The molding compound was injected at 8 MPa plunger pressure. The die was then cured for 3 minutes at 180°C inside the mold. The samples were removed from the mold and a post mold cure was then performed in an oven at 180°C for 4 hours. To inspect the packaged samples, the plastic compound was first removed by means of sulfuric acid.

2.4.4 Inspection

After performing the uniaxial and hydrostatic loading tests, the samples were cleaned and inspected. A visual inspection is done with an optical microscope. Cross-sections and more detailed images are achieved by Scanning Electron Microscope (Fig. 2.9-2.12). A DekTak 150 profilometer and a Wyko NT3300 optical profiler are used to characterize the deflection of the capping layer when the packages were loaded.

2.5 Measurement Results and Discussion

2.5.1 Deflection

To demonstrate the benefit of the column-based approach a comparison in terms of deflections has been made between the packages fabricated with and without columns. As showed in 2.2.1 section, a square-panel simply supported on all the edges without columns shows a bigger deflection than a plate supported by four columns in the middle of the plate, when loaded with a certain load q. After sealing the packages, the capping layer is uniformly loaded under 100 kPa atmospheric pressure. The measured deflection of the capping layer for packages with and without columns confirm that by using columns the deflection of the cap decreases by one order of magnitude (Fig. 2.14).

2.5.2 Uniaxial Loading

A distributed load of 37.5 MPa was applied by the bonding machine. By using Eq. 2.6, a maximum normal stress of 6 GPa is calculated on the weakest columns. After loading the samples by the bonding machine, the inspection revealed that no package was broken. Although it was not possible to achieve pressures higher than 37.5 MPa, this test gives a lower limit of 6 GPa to the compressive strength of SiN.

2.5.3 Hydrostatic Loading

Both the arrays of square packages with and without columns were loaded with hydrostatic pressure. After the loading test, the samples were inspected for deformations and cracks. The array of packages without columns mostly fail for deflection and not because of the stress. Instead, the array of packages with columns mostly fail for stresses, because by using columns the cap deflection is kept very small (small deflection assumption). However, when the load is large enough, in some cases the caps get attached to the bottom of the package cavity. Permanent deflection were observed by optical profilometry. In Fig.2.15 a reconstructed 3D image of the packages shows the stiction of the capping layer to the bottom of the package.

When the stress is higher than the strength of the capping material, cracks originate in the layer. In most cases cracks are clearly visible and sometimes the columns are broken (Fig. 2.16). When the cracks were not visible ethanol was used to reveal if the packages were leaky. Indeed, when packages with tiny cracks were wet by ethanol, liquid fringes could be

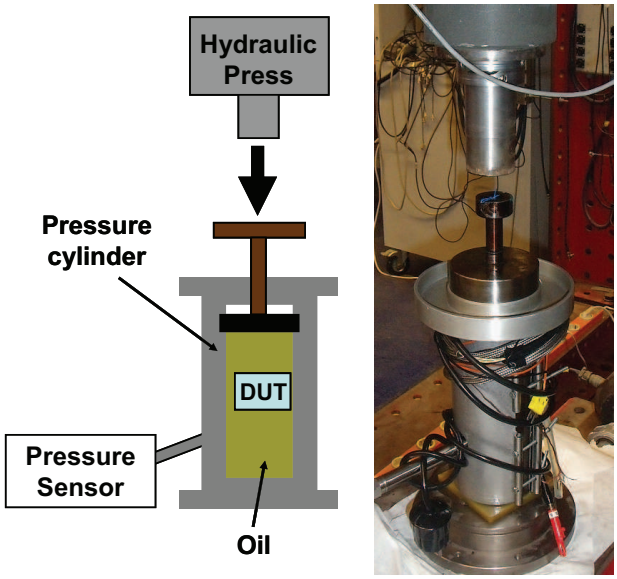

Figure 2.13: Sketch of the setup for the pressure test.

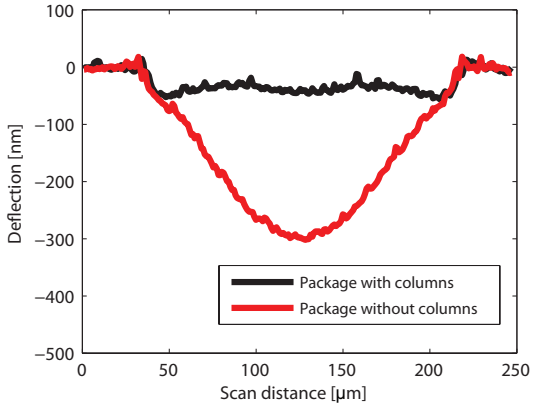

Figure 2.14: Deflection of the package under 100 kPa (1 bar) load. Comparison between two square packages (180 μm side length) with and without columns (4 μm diameter). Already at this pressure the deflection of the package with no columns is too large for many applications.

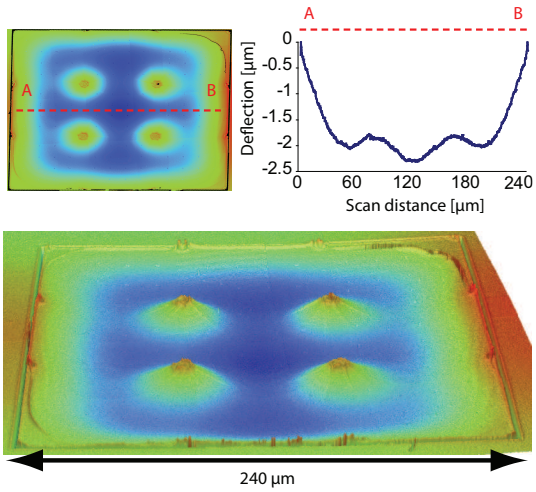

Figure 2.15: 3D imaging of the packages by optical profilometry after loading. The cap deflects and is stuck to the bottom of the package.

seen through the capping layer, indicating that the ethanol could penetrate through the cracks into the cavity. Fig. 2.16d shows a close-up of a column of a broken package. The cracks are formed around the pillar. This is in good agreement with the theory, as the weakest part of the flat slab structure is the interface between column and plate, where most of the cracks originate. Both tangential and radial cracks were observed. The tangential cracks appear on the column circumference and they are due to the radial component of the bending stress. The radial cracks instead are due to the tangential component of the bending stress. As said previously, the tangential component is slightly smaller than the radial one.

The results of the pressure test are shown in Fig. 2.17 for LPCVD processed packages with capping thicknesses t of 3 μm and 6 μm, and in Fig. 2.18 for PECVD processed wafers, with capping thickness t of 5 μm. The graph shows which samples pass or fail the test. Results have been ordered by geometry and maximum bending stress around the columns (calculated according to Eq.2.11). The red markers represent the packages that fail during the pressure test, i.e. the packages that appeared to be cracked or leaky after inspection. As it can be seen from the figures, there is no stress value that sharply divide the broken and not broken packages. This scatter is due to the statistical nature of the failure mechanisms [50]. In fact, an ideal (defect-free) material would always fracture at the same stress, due to breaking of bonds every time it is loaded. The failure of a real mate-

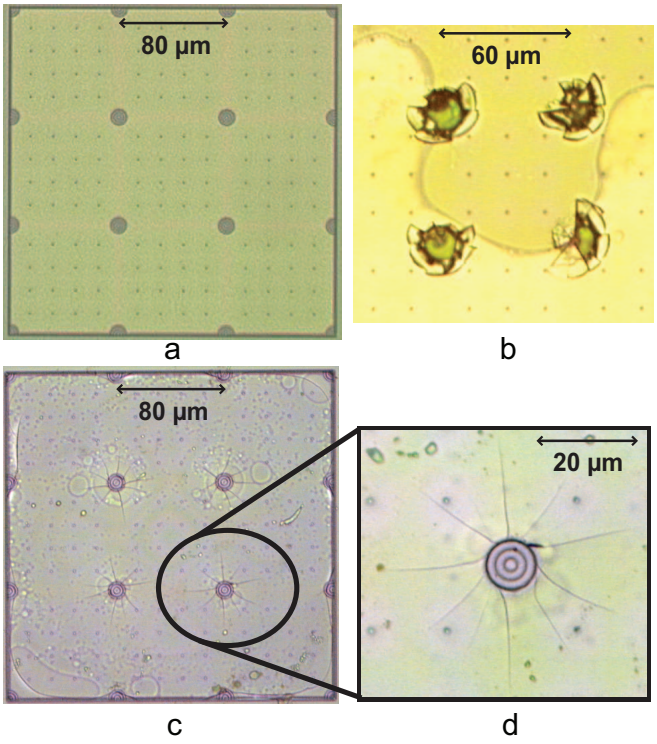

Figure 2.16: Optical microscope inspection of packages. a) Image of a package before loading test. b) Broken columns. Radial and tangential cracks are visible. c) Image of a package after the loading test with cracks. d) Zoom-in of one column. The crack is circular around the column and becomes radial moving away from the column.

rial however, is dominated by randomly distributed defects and hence the fracture properties are treated statistically. The fracture strength of brittle materials like SiN is generally characterized by a probability distribution. Weibull distribution assumes that the whole sample fails when a critically sized defect is encountered anywhere in the sample. The Weibull strength is the strength corresponding to a certain failure probability (typically higher than 60%). A fundamental study of the strenght of SiN is reported in [50]; it shows a Weibull strength of 6 GPa, with a rather small scattering in fracture points. To evaluate the Weibull strength of the capping material we used, dedicated test structures have been fabricated. They consist of an array of circular and square packages. The span is ranging between 20 and 200 μm with steps of 20 μm. All caps are produced with and without supporting pillar in the center (circular shape and 5 μm diameter). Four different cap thicknesses have been chosen for the capping layer: 1, 3, 5 and 7 μm. The samples have been hydrostatically loaded and inspected. The Weibull strength has been inferred fitting the failure results with the theory. Those inferred strength values are in agreement with [50].

The stress value corresponding to the dashed line in both Figs. 2.17 and 2.18 is the maximum tensile stress over which about 90% of the packages fail. This roughly corresponds to the Weibull strength of the capping material. A strength of 3 GPa is inferred for the high-temperature packages, whereas it is 1.5 GPa for low-temperature packages. Due to their smaller robustness, low-temperature packages require about 40% thicker capping layer (see Eq.2.12) compared to high-temperature packages in order to withstand the same load. This difference is probably due to different properties of the silicon nitride layers deposited with different deposition techniques. In short, a high temperature square package with 4 middle columns (10 μm diameter) and with 100 μm distance between columns, will withstand overmolding only if its cap thickness is at least 6 μm. If a thinner capping layer is preferred then the space between the columns has to be decreased. For instance, a package with a 3 μm thin capping layer can withstand the overmolding only if the distance between columns is maximum 60 μm.

2.5.4 First-level Packaging

The packages were tested under typical back-end processes, like wafer thinning, dicing, die-attaching and overmolding. The maximum pressure is around 8 MPa and coincides with the overmolding step pressure. The packages designed to withstand a pressure of at least 10 MPa were indeed not damaged during the thinning/molding steps 2.19. This confirms the validity of the presented mechanical model and demonstrates that the pre-

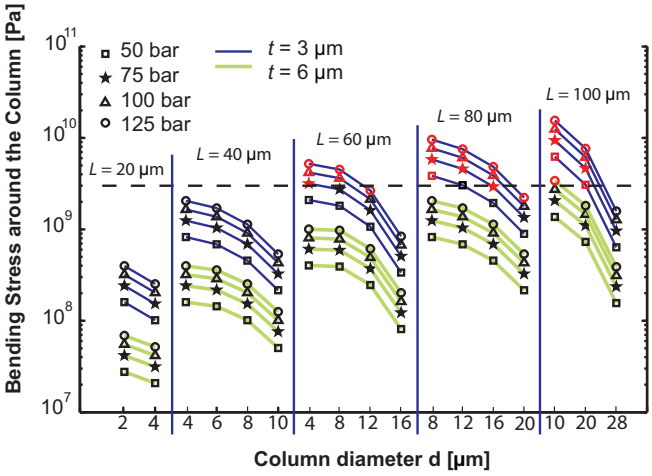

Figure 2.17: Results of the hydrostatic pressure test for high-temperature packages. The red markers represent the broken packages. The dashed line divides the broken and not broken packages. On the vertical axes the calculated bending stress around the columns (see Eq.2.11) is reported as a function of the column spacing L, column diameter d, capping thickness t and applied load q.

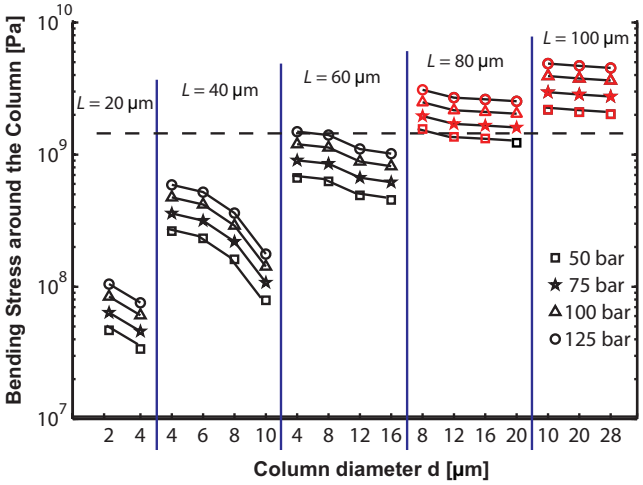

Figure 2.18: As for Fig.15. Results of the pressure tests for low-temperature packages with 5 μm capping layer.

sented thin-film encapsulation approach is robust enough for withstanding the loads on the back-end processing steps.

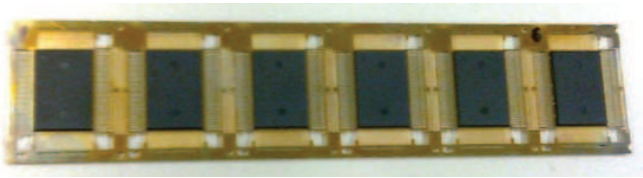

Figure 2.19: Strip of six QFP100 molded packages ready for the overmolding step.

2.6 Conclusions

In this chapter, we presented a model to design MEMS thin-film encapsulation that is sufficiently strong for overmolding. The basic geometry considered for the mechanical model is a flat slab structure supported by columns. The structure was dimensioned by taking into account both the deflection of the capping layer and the generated stresses. Different packages based on the presented design were fabricated. The packages differ for the diameter of the columns, the distances between columns and the capping layer thickness. Both packages made by high and low temperature encapsulation processes were fabricated.

The packages were pressure tested with different loads up to 12.5 MPa (125 bar). The tests show that the weakest points in the packages were the ones identified by means of the presented mechanical model. Moreover, the packages were carried through wafer thinning, dicing, die-attaching and overmolding, demonstrating that the proposed thin-film encapsulation design is robust enough for withstanding the commercial first-level packaging processes.

Besides the mechanical robustness also the hermeticity of thin-film encapsulation is an important aspect to be considered. In order to monitor the hermeticity, the vacuum levels inside the micro-packages have to be measured. Pirani gauges are vacuum sensors that can be easily integrated inside the micropackages to monitor their internal pressure. In the next chapter, an analytical model for MEMS Pirani gauges is presented. It represents the starting point for the design of a new tube-shaped Pirani gauge ideal for the vacuum monitoring of micropackages fabricated by thin film encapsulation as explained in chapters 4 and 5.

Chapter 3

Modeling of MEMS Pirani Gauges

3.1 Pirani gauges

Long-term stability and *in situ* pressure measurement of traditional platform packages are often evaluated using helium leak-rate tests. However, helium leak testing equipment is expensive and is generally limited to leak rates greater than 10^{-12}Pa m^3/s [39,40]. Consequently, for such micropackages, vacuum measurements are performed mostly by sensors integrated in the packages such as resonators [39,52,53] and Pirani gauges [26,54]. In general, Pirani gauges are easier to calibrate and test and usually have higher pressure sensitivities [41] than resonators.

Pirani gauges consist of suspended resistors of which the heat loss provides a measure for the surrounding pressure [55]. Micromachined Pirani gauges have the advantages of a wide pressure range, small dimensions, and low power consumption when compared to conventional Pirani gauges [40]. Besides the *in situ* monitoring of the hermeticity of packages for MEMS devices, they are mostly found in equipment where the vacuum has to be measured. Moreover, Pirani gauges are used even above atmospheric pressure. They can therefore substitute diaphragm-based pressure sensors [56, 57].

A large number of micromachined Pirani gauges has been developed so far [26, 40, 41, 54, 56–69], using a variety of processes and geometries. With respect to their geometry, however, they can be divided into two groups. In the first group a serpentine metal [58–60] or poly-Si [61,62] thin-film resistor is patterned on top of a rectangular dielectric membrane. The dielectric is used as a mechanical support and is needed because of the high residual

stress and low mechanical rigidity of many metal and poly-Si thin films. The second group of gauges has polysilicon or doped-silicon microbridges, such as the vertical designs presented by Mastrangelo *et al.* [64,65], Stark *et al.* [41,63,66], Mitchell *et al.* [40] and the lateral design presented by Chae *et al.* [41].

Mathematically, most MEMS Pirani gauges can be reduced to a bridge with constant cross section (Fig. 3.1). This geometry was used by Mastrangelo *et al.* [64,65,70] to derive an analytical expression for the transfer function of the sensor. However, this transfer function is transcendental. Therefore, it is not straightforward to evaluate how the geometry influences the performance of the gauge and in particular its pressure range. So far, therefore, the device performance has mainly been evaluated by numerical simulations [40]. For designing sensors this is rather time-consuming and obscures insight into the physical mechanisms by which the performance is determined.

3.2 Analytical Model

This work extends the model of Mastrangelo and expresses the pressure range as a closed-form algebraic function of the bias current and of the geometrical parameters of the sensor [71]. In this way, designers can trade-off the performance of the gauge against the costs, represented by design variables such as the chip area and the bias current. The function is obtained by modeling the temperature profile of the sensor with a rational function. The model also yields simplified expressions for other performance parameters such as the sensitivity, output swing and power consumption. The validity of the model is verified by the design of a Pirani gauge, which is fabricated and experimentally characterized.

Fig. 3.1 shows the geometry of a MEMS Pirani gauge suspended at the edges on two anchors. The geometry parameters are the bridge length L, the width w, the thickness t and the gap g between the bridge and the substrate. When a current I passes through the bridge, the temperature increases and, therefore, the resistance changes. The heat is conducted to the substrate both through the gas and the anchors. When the pressure p changes, the conduction through the gas changes accordingly. This leads to a different average temperature of the resistor and thus to a different resistance value. In this way, the voltage change across the resistor is a measure of the gas pressure.

The sensor can be operated in constant-temperature or constant-current mode [70]. In the first mode a feedback loop is used to eliminate effects of thermal expansion, thereby increasing the range of operation of the sensor.

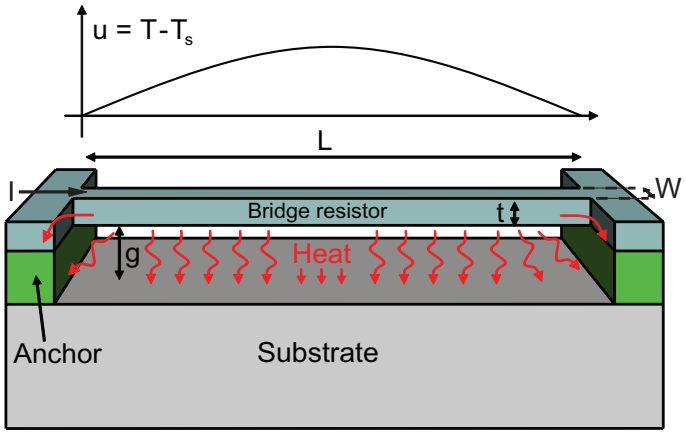

Figure 3.1: Sketch of a micromachined Pirani gauge and typical temperature profile along the bridge.

The constant-current mode, however, is simpler to implement. Here, we only model the constant-current mode. The model can nevertheless be extended to the constant-temperature mode.

3.2.1 Existing model

The transfer function of the sensor is represented by:

$$V(p) = IR(p) = IR_0(1 + \xi\bar{u}(p)), \quad \text{with} \quad R_0 = \rho\frac{L}{tw}, \tag{3.1}$$

where ρ is the electrical resistivity of the bridge material, ξ is the temperature coefficient (TCR) of the Pirani gauge resistance $R(p)$ and $\bar{u}(p)$ is the average temperature rise of the resistor that changes with the pressure p. The average temperature $\bar{u}(p)$ can be calculated from the heat balance differential equation with homogeneous boundary conditions $u(0) = u(L) = 0$ [65]. This yields:

$$\bar{u}(p) \equiv \frac{1}{L}\int_0^L u dx = \frac{\delta}{\epsilon(p)}\left(1 - \frac{\tanh(\sqrt{\epsilon(p)}\ L/2)}{\sqrt{\epsilon(p)}\ L/2}\right), \tag{3.2}$$

in which δ represents the ohmic heat generation:

$$\delta = \frac{I^2 R_0}{kwLt}, \tag{3.3}$$

and ϵ represents the heat loss through the gas:

$$\epsilon(p) = \frac{\eta k_c p}{kgt(p + p_0)} - \delta\xi. \tag{3.4}$$

The thermal conductivity of the bridge material is k whereas k_c is the thermal conductivity of the gas at ambient pressure. The correction factor η accounts for the fringing of the heat flux through the gap [70] (typically close to one) and p_0 is the so called transition pressure [65],

$$p_0 = \frac{\eta}{g}\frac{w}{t+w}\frac{k_c T_s}{v} \tag{3.5}$$

where T_s is the substrate temperature and v is the average molecular gas velocity.

The transfer function of Eqs.3.1-3.5 is a transcendental function and for this reason it is not possible to express the pressure range, sensitivity and output swing as algebraic function of the geometrical parameters of the sensor. So far, therefore, those performance parameters have mainly been evaluated by numerical simulations [40].

3.2.2 Extension of the model

To come around this limitation, the transcendental expression of $\bar{u}(p)$ (given in Eq. 3.1) has to be transformed into an algebraic function. We have replaced the hyperbolic tangent with its third-order Pade‘ series expansion [72]:

$$tanh(x) \approx \frac{\frac{1}{15}x^3 + x}{\frac{2}{5}x^2 + 1}. \tag{3.6}$$

Fig. 3.2 shows the validity of the approximation as a function of x and for different orders. The approximation changes the average temperature $\bar{u}(p)$ of Eq. 3.2 to:

$$\bar{u}_p(p) = \frac{5}{6}\frac{L^2\delta}{10 + \epsilon(p)L^2} \approx \bar{u}(p). \tag{3.7}$$

The error e_r introduced by this series approximation is shown in Fig. 3.3. Analytically it equals:

$$e_r = |\bar{u}_p - \bar{u}| = \left|\frac{\delta L^2}{2\alpha^3}(p_n(\alpha) - \tanh(\alpha))\right| \tag{3.8}$$

where

$$\alpha = \frac{\sqrt{\epsilon(p)}\ L}{2}. \tag{3.9}$$

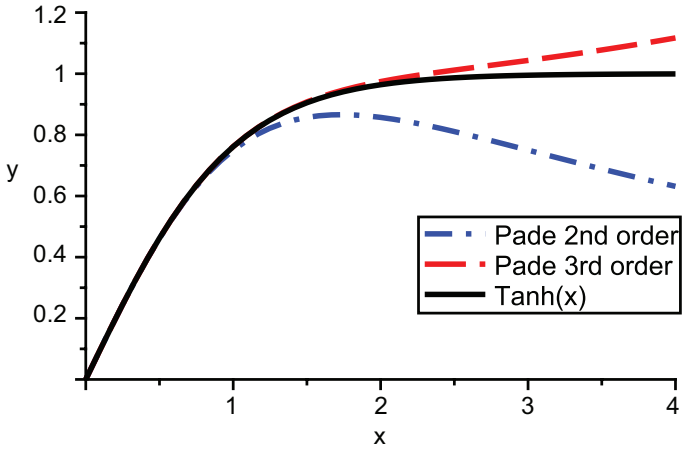

Figure 3.2: Comparison between the hyperbolic tangent function and its Pade' series expansion of second and third order.

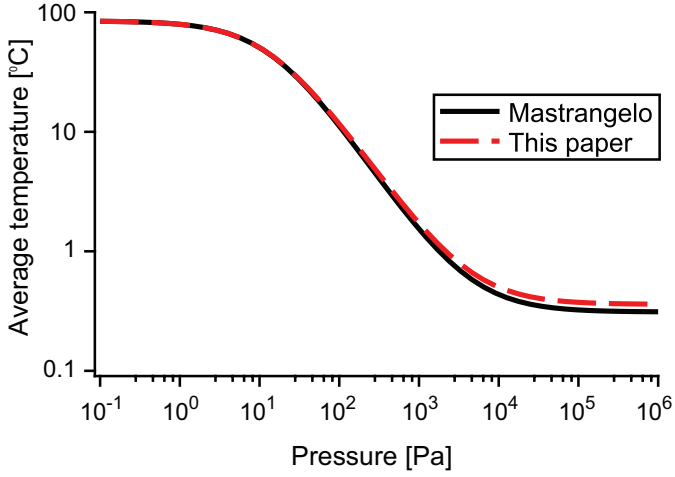

Figure 3.3: Comparison between the average temperature calculated according to the Mastrangelo model and the one obtained following the model presented here.

Considering that [72]

$$|\tanh(x) - p_n(x)| \leq |p_{n+2}(x) - p_n(x)| \tag{3.10}$$

where $p_n(x)$ is the n$^{\text{th}}$-order Pade series, the fractional error relative to the maximum temperature difference $\bar{u}_{max}$ is:

$$\frac{e_r}{\bar{u}_{max}} \leq 6/5 \frac{\alpha^4}{(63 + 28\alpha^2 + \alpha^4)(5 + 2\alpha^2)} \leq M \tag{3.11}$$

where

$$\bar{u}_{max} = \lim_{p \to 0} \bar{u} = \frac{\delta L^2}{12}. \tag{3.12}$$

M is the maximum of the error function and equals 0.011. This means the error is always less then 1.1% of u_{max}, independent of any variable.

The transfer function $V(p)$ of a Pirani gauge is typically "S"-shaped (Fig. 3.4(a)). It varies between two asymptotes V_{min} and V_{max}, which are typically at a few percent from each other. In fact, it is useful to specify two alternative transfer functions, $v_1(p)$ and $v_2(p)$, as plotted schematically in Fig. 3.4(c-d),

$$v_1(p) = V_{max} - V(p); \quad v_2(p) = V(p) - V_{min}. \tag{3.13}$$

$v_1(p)$ is more useful at lower pressures, whereas $v_2(p)$ is better applied at higher pressures. The functions have a common point of maximum sensitivity at p_s (Fig. 3.4(b)). Therefore p_s can be defined as the pressure of maximum sensitivity. This is also the pressure where $v_1(p)$ and $v_2(p)$ are half of their maximum value. In other words, p_s is the '-3 dB point'. In fact, plotted on a logarithmic scale, $v_1(p)$ and $v_2(p)$ have a constant part and a part rising and falling, respectively, with 20 dB/dec.

To design a Pirani gauge for a specified pressure range, it appears to be useful to find an analytical relation that links p_s to the geometric parameters of the structure. It can be calculated from the definition of sensitivity S and equaling its derivative to zero:

$$\frac{dS}{d(log_{10}p)} = 0 \quad \Leftrightarrow \quad p_s = \frac{(L^2\delta\xi - 10)p_0}{L^2\delta\xi - 10 - \frac{\eta k_c L^2}{kgt}}. \tag{3.14}$$

Taking into account Eq. 3.12, the term $L^2\delta\xi$ in the Eq. 3.14 equals to $12\bar{u}_{max}\xi$. Considering that ξ is in the order of 10^{-3}, and that $\bar{u}_{max}$ is generally kept under 100 K, to limit the thermal expansion, this yields

$$L^2\delta\xi = 12\bar{u}_{max}\xi << 10. \tag{3.15}$$

Considering also that generally $w >> t$, Eq. 3.14 can be further simplified:

$$p_s = \frac{p_0}{1 + \frac{\eta k_c L^2}{10kgt}} \tag{3.16}$$

and the maximum sensitivity S_{max} is given by:

$$S_{max} \equiv S(p_s) = \frac{\ln 10}{48} \frac{\xi (IR_0)^3}{k\rho}; \tag{3.17}$$

It is possible now to show that S_{max} is proportional to the output voltage swing ΔV:

$$\Delta V = V_{max} - V_{min} = IR_0 \xi (\bar{u}_{max} - \bar{u}_{min}), \tag{3.18}$$

$\bar{u}_{max}$ is given by Eq. 3.12 and $\bar{u}_{min}$ is calculated as

$$\bar{u}_{min} = \lim_{p \to \infty} \bar{u}_p = \frac{\bar{u}_{max} p_s}{p_0}. \tag{3.19}$$

Combining Eqs. 3.18 and 3.19, yields:

$$\Delta V = IR_0 \xi \bar{u}_{max} (1 - \frac{p_s}{p_0}) \tag{3.20}$$

and replacing the values for $\bar{u}_{max}$, p_s and p_0 given in Eqs. 3.5, 3.12 and 3.16, respectively in Eq. 3.20, the output voltage swing is derived as

$$\Delta V = \frac{1}{12} \frac{\xi (IR_0)^3}{k\rho} = \frac{4 S_{max}}{\ln 10}. \tag{3.21}$$

It can be noticed that $\Delta V / S_{max}$ does not depend on the geometrical parameters of the sensor because it is equal to 4/ln10. This means that increasing the sensitivity S_{max} will produce a proportional increase of the output voltage swing ΔV.

3.2.3 Pressure range

The design of a Pirani gauge requires an equation that relates the pressure range to the geometrical parameters of the sensor and to the biasing current. The lower detection limit p_l but also the upper pressure limit p_h of the pressure range are determined by the transfer function and the voltage detection limit N (Fig. 3.4(d)). N is determined by noise, ambient temperature fluctuation, piezoresistive effects, and/or the resolution of the electronic equipment. The detection limit p_l is found from the intersection

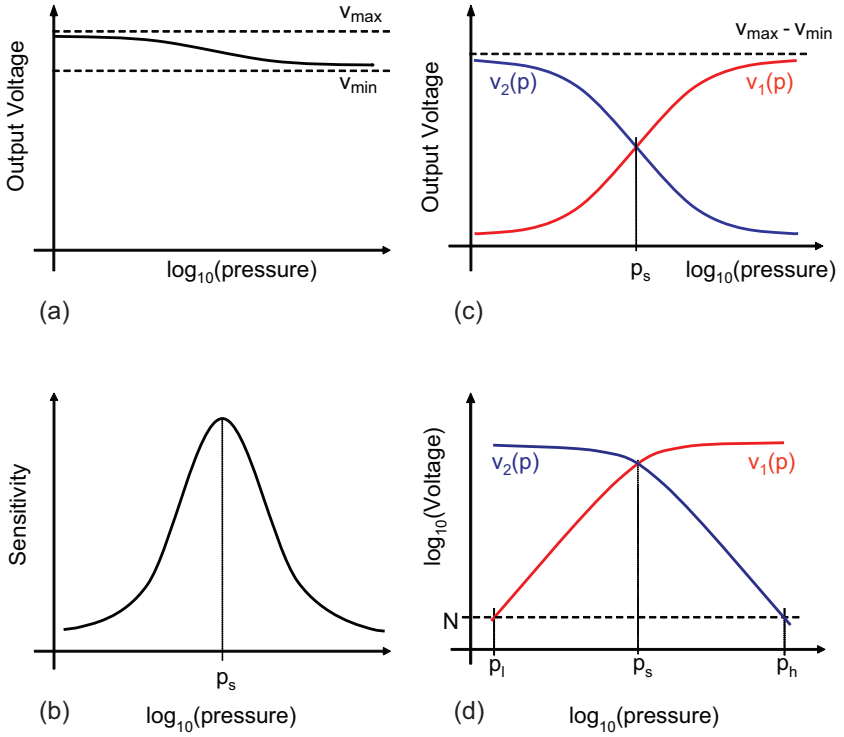

Figure 3.4: (a) Transfer function of a Pirani gauge. The voltage change with the pressure $V(p)$ is typically few percent. (b) Sensitivity of the Pirani gauge. (c) Alternative transfer functions $v_1(p)$ and $v_2(p)$. (d) Double logarithmic plot of the transfer functions; N represents the limit with which the output voltage difference can be measured.

between the horizontal line N and the transfer function $v_1(p)$, while for p_h the function $v_2(p)$ is considered:

$$p_l = p_s \frac{N}{\Delta V - N}; \quad p_h = p_s \frac{\Delta V - N}{N}. \tag{3.22}$$

ΔV and p_s are calculated from Eqs. 3.16 and 3.21, while p_l, p_h and N are usually given by the specifications. From Eq. 3.22 it can be shown that $\log(p_s)$ is the middle point (on the logarithmic scale) of the pressure range determined by the pressure limits $\log(p_l)$ and $\log(p_h)$ ($p^2{}_s = p_l p_h$).

The dynamic range is defined as the ratio between the upper and lower pressure limits and can be expressed as

$$\Delta = \frac{p_h}{p_l} = \left(\frac{\Delta V - N}{N} \right)^2. \tag{3.23}$$

3.2.4 Implications for Pirani gauge design

The design of a Pirani gauge should consider the specification of the pressure range of operation and the wish to keep the cost as low as possible. This requires the optimal dimensioning of the geometry, choice of materials, bias current, and read-out circuitry. Quite often, the cost are directly related to chip area, so to the size of the gauge. Moreover, the dimensioning should be done within certain boundary conditions. Those include e.g. the maximum temperature of a given construction material.

As can be seen in Eq. 3.22, the center of the pressure range is determined by p_s, the pressure of maximum sensitivity. The possibilities to dimension this parameter are given by Eq. 3.16 and Eq. 3.5. Eq. 3.16 basically has two distinct areas of operation:

$$\frac{\eta k_c L^2}{10kgt} << 1 \quad \text{and} \quad \frac{\eta k_c L^2}{10kgt} >> 1 \tag{3.24}$$

In the former case the device is relatively short and thick. Then, p_s almost uniquely depends on p_0. Usually, the width w is larger than the layer thickness t, and η, T_s and k_c are given. This means that the only effective way to influence p_s is through the gap size g: $p_s \propto 1/g$.

In the latter case the device is relatively long and thin. This cancels the influence of the gap size, but makes p_s proportional to t/L^2. Thus, the pressure range can be tuned by the thickness and particularly by the length of the gauge. In particular, considering a certain given value for t, in order to shift the pressure range towards low pressure the gauge length L has to be increased. On the other hand, for a higher pressure range, the length has to be decreased.

As stated by Eqs. 3.22 and 3.23, both the detection limits and the dynamic range depend on ΔV. According to Eqs. 3.21 and 3.17 it depends to the power three on the voltage drop caused by the bias current, IR_0. It also depends linearly on the material parameters k_c, k, and ρ, but those parameters cannot always be influenced to a sufficient amount. Thus, for a high dynamic range it is advisable to bias to the maximum and make the bridge of a low-resistivity material.

Finally, the pressure range (Eqs. 3.22 and 3.23) depends on the voltage detection limit N. This parameter is strongly dependent on the read-out electronics, the fabrication technology, and the environmental conditions. In this work it is assumed to be a given constant.

3.2.5 Boundary conditions

According to Eq. 3.23, the dynamic range Δ is determined by the voltage detection limit N and the output voltage swing ΔV. The pressure range can in theory be centered to any value according to Eq. 3.16. Pirani gauges with gap as small as 50 nm are reported [56, 57] leading to a high pressure range centered around 200 kPa, whereas bridges as long as 40 mm [54] show a detection limit of 1.3 Pa.

In practice, however, there are a number of boundary conditions limiting the degrees of freedom, like the fabrication process, the footprint available, the mechanical stability, the power consumption and the voltage detection limit N. Geometrical parameters like the gap size and the bridge thickness may be imposed by the technology, whereas the bridge length deals with the footprint of the device. An important boundary condition may be the maximum power consumption allowed bu the system, P_{max}:

$$R_0 I^2 < P_{max} \tag{3.25}$$

The limit on ΔV is given by the limit on the temperature, since ΔV is proportional to $\bar{u}_{max}$ (see Eq. 3.20). A first limit on the operating temperature is given by the maximum temperature of the resistor material that depends on the fabrication process.

A second limit to the temperature is imposed by thermal expansion that may cause buckling of the bridge. Buckling is an event that changes the gap and may even cause a thermal "short circuit". Buckling occurs when the stress in the beam is compressive and exceeds a critical value σ_c. The stress consists of a residual stress σ_r from fabrication and a thermal stress σ_t, due to thermal expansion during operation [73]:

$$\sigma_t + \sigma_r < \sigma_c = \frac{\pi^2 E t^2}{3L^2} \quad \text{with} \quad \sigma_t = E C_T \bar{u}_{max} \tag{3.26}$$

where E is the Young's Modulus of the resistor material and C_T its linear thermal expansion coefficient.

3.2.6 Non-idealities

Since the geometry of many MEMS Pirani gauges does not consist just of a bridge resistor, there are some non-idealities that have to be taken into account in order to successfully use the model.

Multilayer-bridges

When the Pirani bridge consists of a stack of multiple layers, many model parameters have to be corrected. In fact, the effective values for Young's Modulus E_{eff}, intrinsic stress σ_{eff} and thermal conductivity k_{eff} should be calculated as follows (see [73–75]):

$$\sigma_{eff} = \frac{\sum \sigma_i t_i}{\sum t_i} \quad E_{eff} = \frac{\sum E_i I_i}{I_{eff}} \quad k_{eff} = \frac{\sum k_i t_i}{\sum t_i} \tag{3.27}$$

where t_i is the thickness of the i-layer, I_i is the second moments of area with respect to the neutral axis and I_{eff} is the effective moments of area of the layer stack.

Different resistor geometry

Under certain assumptions the presented model can still be used even if the resistor does not consist of just a straight wire. In serpentine-based resistors supported by a mechanical layer, if the bridge width w is much smaller than the bridge length L and the distance between the serpentine wrinkles d is small enough, the resistor can be approximated by a multilayer-bridge. It should be noticed, however, that the resistance value R_0 cannot be expressed in terms of length L, width w and thickness t of the bridge. If the serpentine resistor is not supported by any mechanical layer, then the model can be used only if $d >> g$. This condition ensures that there is almost no heat flux between the serpentine wrinkles through the gas. In this case, the serpentine behaves like a bridge with length, width and thickness coinciding with the ones of the serpentine itself.

Fringing factor

As said before the factor η takes into account the fringing of the heat flux from the heater to the heat sink. Its value is exactly one only if the distance between the heat sink and the Pirani resistor is uniform across the section and along the whole length of the Pirani gauge. This is not likely the case. However, the value of η can be predicted by considering the transverse heat transfer rate from the heater to the sink. In many cases, the two dimensional conduction problem in the transverse section can be solved by utilizing some existing analytical solutions that are usually reported in terms

Table 3.1: Constants used in the equations

c_T [ppm]	ξ [ppm/K]	k_c [W/mK]	ρ [$\mu\Omega$m]	k_{eff} [W/mK]	E_{eff} [GPa]
2.7	740	0.022	15	27	203

of a *shape-factor* [74]. However, in cases where a more accurate prediction of the effective gap size is needed, a FEM simulation should be carried out, restricted to the cross section domain.

3.3 Verification of the model

A Pirani gauge was designed with the presented model and experimentally characterized (Fig. 3.5). The main requirement was to design a gauge able to resolve pressure measurements from 50 Pa up to atmospheric pressure. In order to resolve pressure measurements with a signal-to-noise ratio of least 3, we solved the design equations considering a voltage detection limit of 150 μV that is three times bigger than the nominal detection limit of our source meter (Keithley 34567). This pressure range is logarithmically centered around p_s =2400 Pa.

In order to avoid the buckling, the Pirani resistor is coated with a layer of silicon nitride (70 nm) with tensile residual stress (250 MPa). In such a way the residual stress of the structure is close to zero. Furthermore, the thermal compressive stress σ_t is kept at one half of the buckling critical stress. The values of the material constants are listed in the Table 3.1. It should be noticed that since our Pirani bridge consists of a stack of two different materials, the effective values for Young's Modulus, intrinsic stress and thermal conductivity were considered.

The length, width and the thickness coming from these specifications are obtained by solving Eqs. 3.16, 3.17, 3.21 and 3.22. The solution is given by a Pirani gauge with $L = 250$ μm, $w = 4$ μm and $t = 1.4$ μm. The gap size $g = 1$ μm is imposed by the fabrication process. A Pirani gauge with such specifications has been fabricated and tested.

3.4 Fabrication

The starting material is a 525 μm thick silicon wafer of 100 mm diameter. First a 100 nm SiN layer is deposited by LPCVD with a $3SiCl_2H_2 + 4NH_3$ chemistry at a temperature of 850 °C at 19.9 Pa. It is used as electrical insulator between the polysilicon and the silicon substrate. A layer of 1.5 μm silicon oxide deposited by PECVD is used as sacrificial layer. Then a litho

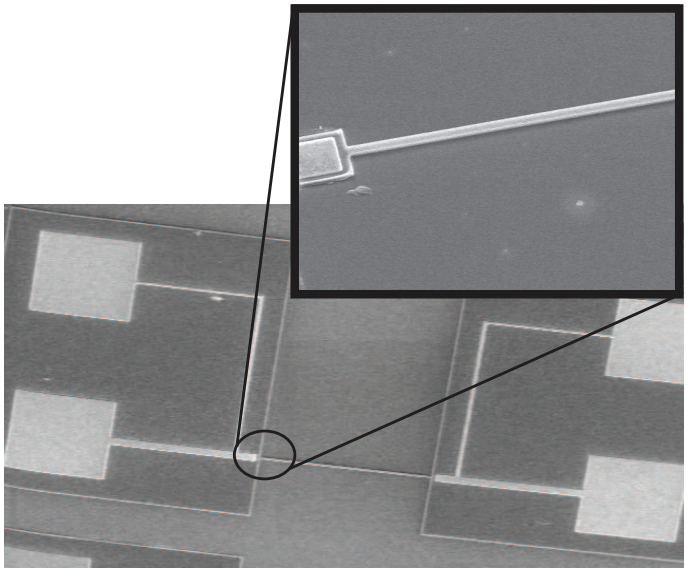

Figure 3.5: SEM image of a released Pirani bridge. It is 4 μ m large and 250 μ m long. The gap to the substrate measures 1 μ m.

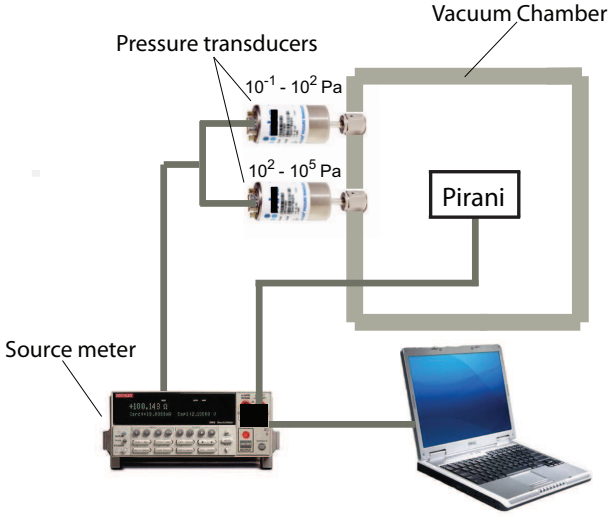

Figure 3.6: Sketch of the calibration setup. The Pirani gauges were tested in a four-point probe configuration inside a vacuum chamber. Two separate pressure sensors were used for measuring the pressure in two different ranges.

step is used to etch the oxide in order to define the anchors regions. The sacrificial layer is covered by 70 nm LPCVD SiN followed by a deposition of 1350 nm LPCVD poly-Si to form the resistor. The deposition makes use of SiH_4 gas at a temperature of 570 °C at 19.9 Pa. This poly-Si layer is phosphorous-doped using a liquid $POCL_3$ source via a nitrogen carrier gas, with a 30-min deposition time and a 30-min soak time at 950 °C. A sheet resistance of 12 Ω/square is achieved after the annealing step. After doping, the poly-Si is covered by another 70 nm LPCVD SiN deposition and the SiN/Poly-Si/SiN stack is dry etched landing into the sacrificial layer to define the bridge. The contact openings are dry etched into the SiN layer landing on the poly-Si and a sputtering deposition of aluminum is performed. The aluminum layer is then patterned by dry etching to define the metal lines and the pads. Finally, the sacrificial etch is performed to release the bridge by means of vapour HF. A SEM image of a Pirani bridge in its final stage is showed in Fig. 3.5. The bridge is released from the substrate and the gap is visible and uniform.

3.5 Measurement set-up

For a pressure calibration, first the temperature coefficient of resistance (TCR) was measured according to the measurement method reported in [76]. The gauges were inserted into a metrology well (FLUKE 9173), and the temperature was monitored with an external PT25 temperature sensor (FLUKE 5628). The electrical signals were handled with a 6.5 digit digital multimeter (Agilent 34401A). All the instrumentation was controlled by a LabVIEW program. The resistances of the Pirani gauges were biased with a low current (1 μA) so that ohmic heating was kept very low during the TCR measurement. The measurements were performed in the temperature range 35-200°C with 25°C intervals. The TCR value ξ used for the model is listed in the Table 3.1.

For the pressure calibration the devices were placed in a Pfeiffer TSH 071 vacuum chamber with a base pressure of 10^{-3} Pa. During testing, the vacuum chamber was backfilled with dry nitrogen. Although many commonly used gases have almost the same thermal conductivity as nitrogen, light gases such as He and H_2 have thermal conductivities that are two and four times higher [58], thus changing the measured pressure signals by factors of 2.5 and 5, respectively. This should be taken into account in the calibration of the Pirani gauges for applications where the pressure measurement is performed in a predominantly helium or hydrogen environment.

A schematic of the calibration setup is depicted in Fig. 3.6. The pressures were measured using two absolute pressure transducers MKS 722A,

one working up to 0.1 kPa and the other up to 100 kPa. In most cases, a Wheatstone bridge is used to measure the resistance change during the operation of a Pirani gauge. This configuration allows for accurate resistance measurements and can be easily integrated with circuitry. An alternative method for Pirani gauge resistance measurement is to use the four-point probe configuration [40] to eliminate the influence of the resistance of the contacts. For this purpose, a source meter (Keithley 2611) was used to provide the bias current and to measure the voltages drop across the Pirani resistance. Its voltage resolution is 50 μV.

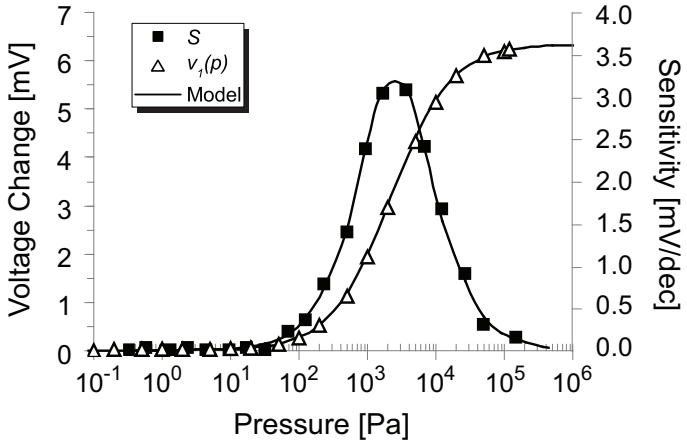

Figure 3.7: Output voltage and sensitivity as a function of pressure; measurements (points) and model (lines) on a semilogarithmic scale. The maximum sensitivity is at 120 Pa as designed.

3.6 Measurement Results and Discussion

The bridge is biased by a constant current $I = 0.5mA$. The measured voltage change across the Pirani gauge has the expected shape when plotted as a function of pressure (Figs. 3.7-3.8). Moreover, a very good quantitative match can be obtained when adjusting the fringing factor η. This means that the fringing of the heat flux cannot be neglected. In fact, although the vertical gap is 1 μm, the closest match is obtained with a fringing factor $\eta = 0.8$, that indicates an effective gap size of $g/\eta = 1.25\mu m$. The sensitivity at each measurement point was calculated as the discrete derivative of the transfer function with respect to the pressure logarithm. The pressure of

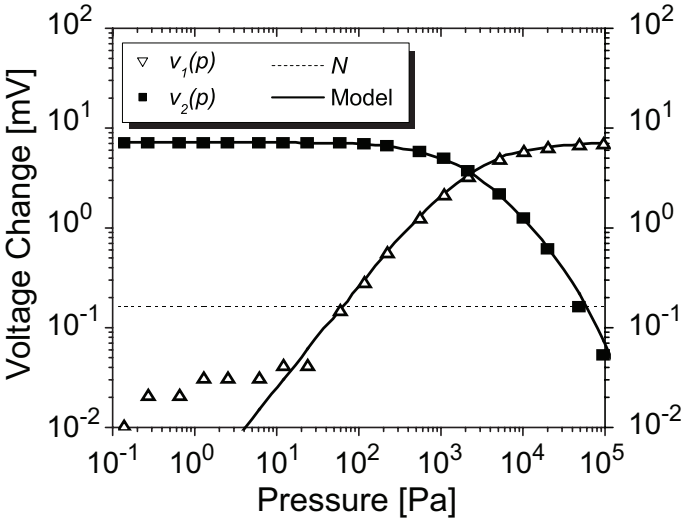

Figure 3.8: Measured and modeled transfer functions $v_1(p)$ and $v_2(p)$ on a double-logarithmic scale. N shows the detection limit.

maximum sensitivity is around 2 kPa very close to the predicted value, and the maximum sensitivity is approximately 3.4 mV/decade.

To better visualize the intersection between the output voltage and the detection limit N, the data are plotted on a double-logarithmic plot (Fig. 3.8). The lower detection limit is around 50 Pa as designed. At this pressure the signal-to-noise ratio is approximately $S/N = 3$. Pressure measurements could be resolved up to atmospheric pressure.

Fig. 3.8 suggests that to use the working range of the sensor effectively a logarithmic amplifier should be employed. In this way a signal is obtained that is linearly proportional to the logarithm of the pressure on the whole range between the noise limits. At the pressure p_s a switch should be made between the transfer functions $v_1(p)$and $v_2(p)$. Literature, on the contrary, quite often proposes linear amplification of only the central part of the S-shaped output voltage $V(p)$. In our opinion this is sub-optimal in terms of dynamic range and linearity.

3.7 Conclusion

In conclusion, we presented a new analytical model for the design of MEMS Pirani gauges operating in constant current mode. This model contains

closed-form analytical expressions for the most important performance parameters, such as pressure range, sensitivity, output swing and power consumption. The model is verified with experimental results and provides a very good match. Its main benefit is that it provides a rapid insight into the relations between the performance parameters and the design variables, such as length, width, thickness, gap and bias current. The model will therefore be very useful to designers of Pirani gauges who need to trade off the performance against the costs associated with chip area and biasing power. These requirements are very important for the application of such sensors to the *in situ* monitoring of the hermeticity of packages for MEMS. In the next chapter a new Pirani gauge specially designed for such application is presented.

Chapter 4

Buried 3D Pirani Gauge

4.1 Introduction

As said in the previous chapter, one application of interest for Pirani gauges is the *in situ* vacuum measurement of the packaging of MEMS devices [11, 26, 40, 54, 63] such as resonators and inertial sensors. For this kind of application, it is important to monitor the pressure inside the package during long-term operation. For such kind of application, very low detection limit is needed to measure accurately the pressure of the micro-packages. Furthermore, because the volume of micropackages is scaling down, to measure accurately the outgassing rate, the vacuum sensor must have also a high pressure sensitivity.

Unfortunately, shifting the pressure range of the Pirani gauge towards lower pressures is not straightforward and requires some trade-offs, as showed in the previous chapter. The range of operation of the Pirani gauge depends on the geometrical parameters of the resistor like length, thickness, width and the gap between the resistor and the substrate. In order to shift the range towards lower pressures, a gauge should be as long and thin as possible.

However, increasing the length of the Pirani gauge reduces the stiffness of the suspension, making it more vulnerable to buckling and more in general to beam deflections. Moreover increasing the ratio between length and gap augments the stiction forces. If stiction occurs, it creates a thermal shortcut between the resistor and the substrate, affecting the proper behavior of the device. Another disadvantage is that longer resistors occupy valuable real estate on the silicon substrate.

In the past, a variety of processes and geometries were used in order

to fabricate Pirani gauges [11, 26, 40, 54, 56, 57, 63, 65, 71, 77]. These devices can be grouped into two categories: resistor on dielectric membrane and microbridge structure. In the first case, a serpentine thin-film resistor is patterned on top of a dielectric membrane, usually LPCVD SiN and/or SiO (Fig. 4.1a). The dielectric is used to improve the mechanical rigidity of the thin film resistor (usually metal or poly-Si) against buckling or stiction, and it permits to fabricate longer resistors, thus suitable for high vacuum measurements. The main drawback for this category is the footprint. The second category consists of a suspended microbridge resistor (Fig. 3.1). Often the resistor is sandwiched in between SiN or SiO dielectric layers. The gap can be formed by bulk silicon etching or by surface micromachining to achieve smaller gaps. The microbridge structure is straightforward to fabricate, but since it is not mechanically supported by a membrane, long thin thermally insulated structures are difficult to make without causing buckling and/or stiction. For this reason low pressure measurements are not possible. In order to achieve this without complicating the fabrication process, a ladder geometry has been proposed (see Fig. 4.1b) that shows a higher stiffness [40]. Like in the membrane-based structures, the footprint is here the main issue.

We have developed a novel Pirani geometry [78, 79], consisting of a polysilicon tube buried inside the silicon substrate (Fig. 4.1c). The tube shape increases the structural stiffness by a factor 10^4 compared to a bridge-based Pirani gauge with the same footprint. This geometry allows for much longer Pirani gauges with smaller gaps without incurring in buckling or stiction problems. For this reason the pressure range is shifted toward lower pressures. In addition, the fact that the tube is buried in the substrate strongly reduces the footprint of the device.

4.2 Design

The design of the Pirani tube has been performed extending the model presented in chapter 3 to the tube geometry. The main parameter of a vacuum sensor is its pressure range of operation, which is specified between its lower p_l and the upper detection limit p_h. In section 3.2.3 equations relating the pressure range limits and the minimum output resolution N were presented; according to those equations, the pressure range can in theory be tuned to any value. In order to shift the pressure range towards lower pressures, a gauge should be as long and thin as possible. In practice, however, there are a number of boundary conditions limiting the degrees of freedom (see section 3.2.5).

One trade-off regards both the detection limit of a Pirani gauge and

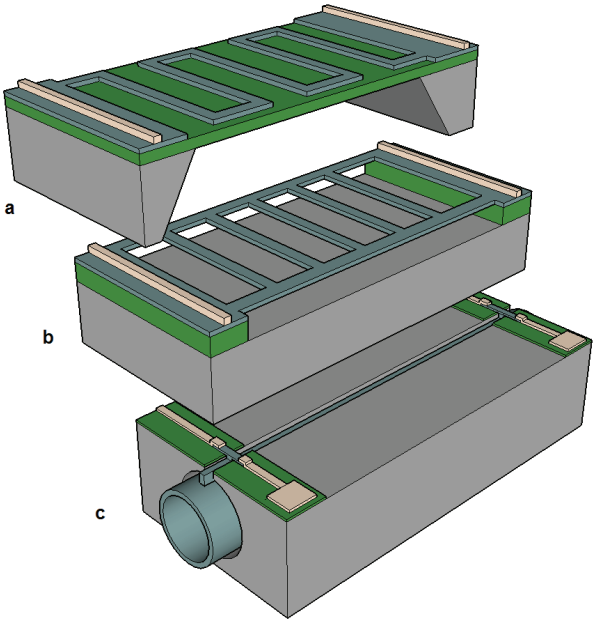

Figure 4.1: Sketch of different Pirani gauge geometries: a) resistor on membrane, b) microbridge structure (ladder configuration), c)tube-shaped Pirani gauge.

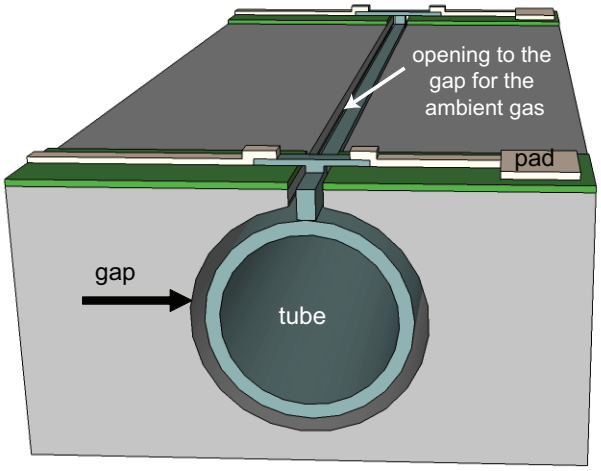

Figure 4.2: Sketch of the Pirani Tube.

its stiffness. In fact, increasing the resistor length would also make it more vulnerable to buckling. A regular polysilicon bridge with a thickness of 2 μm and an intrinsic compressive stress of 50 MPa has a critical length for buckling of 200 μm according to Eq. 3.26, which we also report here:

$$\sigma_t + \sigma_r < \sigma_c = \frac{4\pi^2 E I_A}{A L^2} \quad \text{with} \quad \sigma_t = E C_T \bar{u}_{max} \tag{4.1}$$

where A and I_A are the cross section area and the areal moment of inertia respectively; E is the Young's Modulus of the resistor material, C_T is its linear thermal expansion coefficient and $\bar{u}_{max} = \delta L^2/12$ is the maximum temperature increase. This maximum length limits the minimum p_s that is possible to achieve with such a bridge to few kPa.

A change of the geometry has been considered to improve the mechanical stiffness of the resistor and design a Pirani gauge for much lower pressure ranges. A tube-shaped 3-D geometry has been employed in order to get a strongly increased structural rigidity. A sketch of the structure is depicted in Fig. 4.2. The new geometry consists of a poly-Si hollow tube buried inside a cylindrical cavity in the silicon bulk suspended on opposite ends with anchors at a depth of 5 μm under the silicon surface. The anchors provide the mechanical stability and the electrical contact for the Pirani gauge.

The tube shape increases the areal moment of inertia which, for a tube and a solid beam with rectangular cross section are, respectively:

$$I_t = \pi r^3 t \quad I_b = \frac{w t^3}{12}, \tag{4.2}$$

where w and t are the bridge width and thickness whereas r is the tube radius (assuming $r \gg t$). It can be derived from Eq. 4.2 that a tube becomes already advantageous over a solid rectangular beam with the same outer surface area when $r > t/\sqrt{6}$. The ratio I_t/I_b increases with the square of the tube radius r. The critical load for buckling scales up with the same factor, since it is proportional to the areal inertia (Eq. 4.1). At the same time, the ratio between the critical length for buckling for the tube and bridge geometry Lc_t/Lc_b increases linearly with r. Comparing our design to a bridge with the same thickness and footprint, the areal inertia improves more than 14,000 times and the critical length of buckling increases more than 25 times.

Three different Pirani gauges were designed. They differ for their length, but they have the same thickness, gap size and tube radius. In Table 4.1 the main material parameters are listed. The length L, the tube radius r, the thickness t, and the biasing current I for such Pirani tubes are obtained

by solving Eqs. 3.16, 3.17, 3.21 and 3.22 respect to the specifications on the required pressure range and considering the boundary conditions concerning the stresses and the dissipated power.

The longest Pirani gauge was designed to measure a pressure range going from $p_l = 0.1$ Pa to $p_h = 0.1$ MPa, considering a voltage detection limit N of 50 μV. This pressure range is centered at the pressure $p_s = 100\ Pa$ on the logarithmic scale ($p_s = \sqrt{p_l p_h}$). The critical stress for buckling σ_c for such Pirani tube is set at three times larger than the thermal induced stress (≈ 100 MPa; the intrinsic stress of the polysilicon used in the process can be neglected). For the maximum over-temperature u_{max} a value of 35 K was chosen. The solution is given by a 3 mm long Pirani tube with $r = 17.5$ μm, $t = 1.8$ μm and biased by a current of 1.8 mA. The Pirani tubes of 1.6 and 0.4 mm were designed for measuring ranges going from 0.2 Pa to 0.2 MPa and from 2 Pa to 2 MPa, respectively.

Table 4.1: Material parameters used in the model.

c_T[-]	k_c[W/mK]	k [W/mK]	ρ [Ω m]	E [GPa]
2.7 μ	22 m	45	25 μ	160

4.3 Fabrication

The devices were fabricated using the process flow depicted in Fig. 4.3 [79]. First a SiN layer is deposited by LPCVD with a $3SiCl_2H_2 + 4NH_3$ chemistry at a temperature of 850 °C at 19.9 Pa. It is used as electrical insulator between the polysilicon tube and the silicon substrate. It will also serve as mask material for the further etching step. A trench is etched in the substrate (step a) by means of deep reactive ion etching (DRIE). The depth of the trench defines the distance from the center of the channel towards the surface of the substrate. The wafer is then conformally coated with an LPCVD SiN layer (step b). The SiN is used as mask in the further Si etching step. The coating is removed only at the bottom of the trench (step c) by dry etching.

A wet silicon etch is performed to define the cylindrical cavity (step d), using a solution based on HF and HNO_3 [80]. In Fig. 4.4 a SEM cross section of the cylindrical cavity resulting after the isotropic silicon etching is shown. The LPCVD SiN coating used as masking layer during the etching (still visible in Fig. 4.4) is etched in orthophosphoric acid. After stripping the

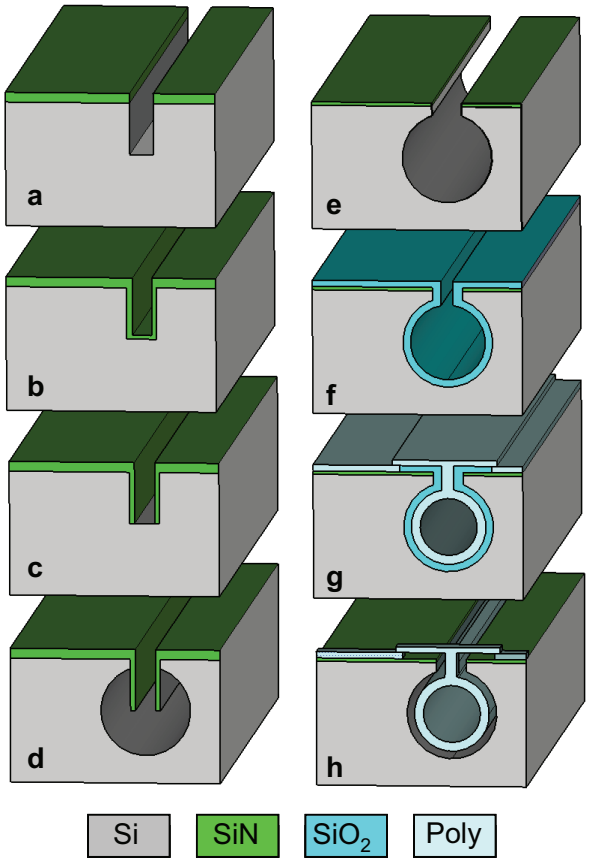

Figure 4.3: Schematic flowchart. A Dry+wet Si etch defines the cylindrical cavity (a-d). A deposition of sacrificial LPCVD SiO defines the gap (f). LPCVD poly-Si doped by $POCl_3$ forms the resistor (g). A sacrificial wet etch is performed to release the poly-Si tube (h).

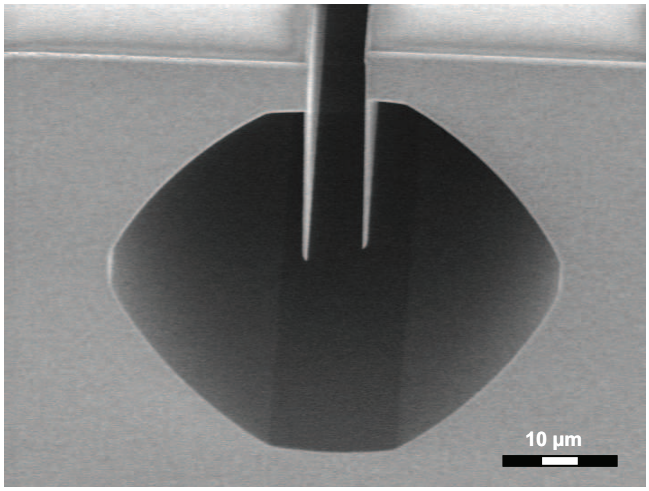

Figure 4.4: SEM cross section of a tube after the wet silicon etching. The LPCVD SiN coating used as masking layer for the sidewalls of the trench during the etching is still visible. As can be see, the etch was not completely isotropic.

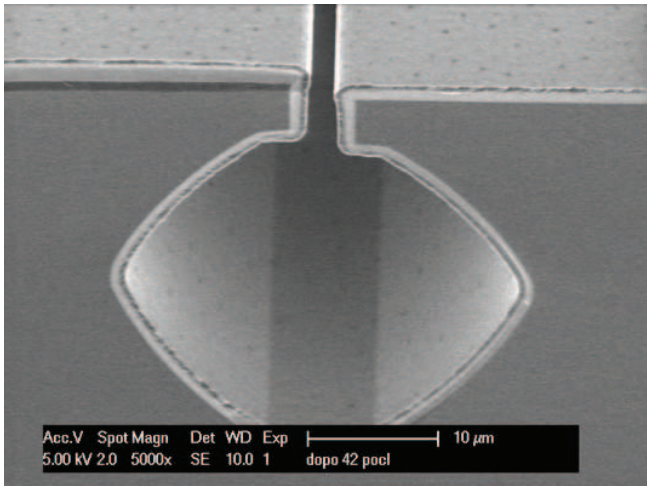

Figure 4.5: SEM cross section of a tube after the poly-Si deposition and $POCl_3$ doping.

LPCVD SiN layer (step e), a sacrificial SiO layer is deposited conformally inside the cavity by LPCVD TEOS (step f) at 33.3 Pa and 700 °C. Then a lithographic step is used to etch the oxide in order to define the anchors regions.

At this point, LPCVD poly-Si deposition is performed in order to form the resistor, without completely sealing the trench. The deposition makes use of SiH_4 gas at a temperature of 570 °C at roughly 19.9 Pa. This poly-Si layer was phosphorous-doped using a liquid $POCL_3$ source via a nitrogen carrier gas, with a 30-min deposition time and a 30-min soak time at 950 °C. Remarkably, the $POCl_3$ coats the interior of the cavity with good uniformity (Fig. 4.5). A further deposition of poly-Si is performed in order to seal the trench (step g). Then an aluminum layer is sputtered to define the contacts. The Al and poly-Si layers are dry etched, landing in the oxide layer.

Finally, the sacrificial wet etch is performed to release the poly-Si tube (step f) by means of HF 73%. After this step the open trench provides the access to the gap for the ambient gas. During the release, no stiction of the tubes is observed, most likely due to the very high stiffness. A SEM cross section of a Pirani tube in its final stage is shown in Fig. 4.6. The tube is released from the substrate and the gap is visible and uniform all around the tube. Fig. 4.7 shows a SEM picture of the edge of the Pirani tube and part of the anchor. During the cutting of the substrate, part of the silicon surrounding the tube was removed making visible the edge of the tube. A top view of a 400 μm long Pirani gauge is showed in Fig. 4.8. The footprint of the device is only 4 μm $\times$ 400 μm, without considering the bondpads.

4.4 Measurement Results and Discussion

For the pressure calibration the measurement setup presented in section 3.5 was used. A schematic of the calibration setup is depicted in Fig. 3.6. Considering the measured TCR values, the biasing current was chosen to generate the same average temperature across the tubes with different lengths in order to compare their performance (Table 4.2). Fig. 4.9 shows the fractional resistance change (relative to the resistance value measured at vacuum) versus the measured pressure for three tubes with different lengths. All curves show the S-shape characteristic of Pirani gauges. The measurement points closely match the curves of the analytical model. Going from 0.4 mm to 3 mm long tube, there is almost a two decades shift toward lower pressures.

In Fig. 4.10 is plotted the measured sensitivity for the fabricated Pirani gauges. The sensitivity at each measurement point was calculated as the discrete derivative of the transfer function with respect to the pressure log-

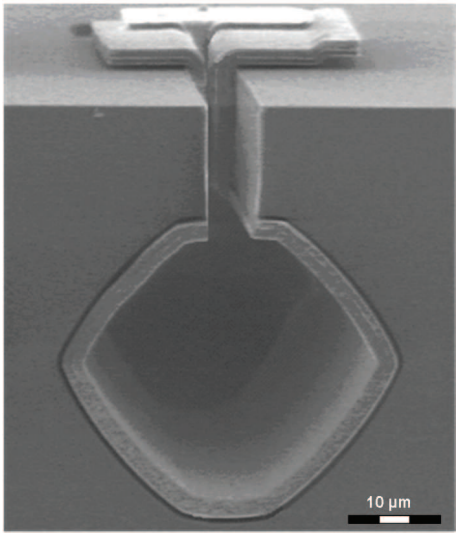

Figure 4.6: SEM cross section of a released poly-Si tube. It is 1.8 μm thick with a diameter of 35 μm. The gap to the substrate measures 1 μm.

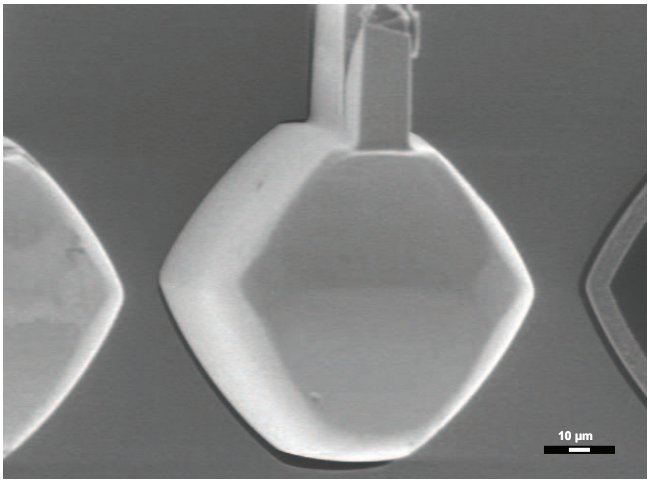

Figure 4.7: SEM picture of the closed edge of the Pirani tube protruding from the cut substrate.

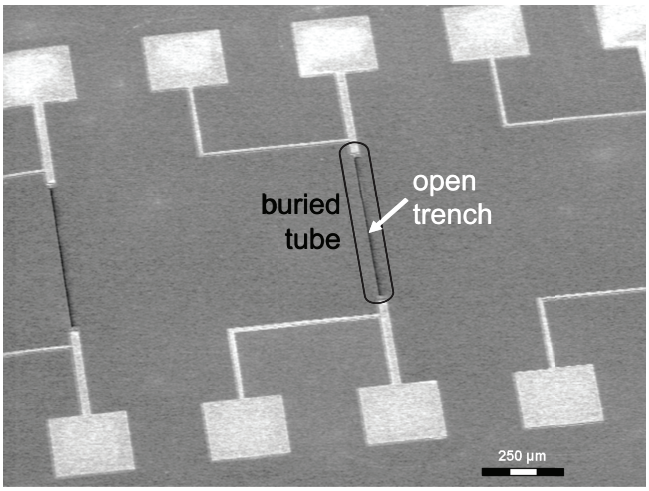

Figure 4.8: SEM Top view of 400 μm long Pirani gauges. The footprint of the device is 4 μm $\times$ 400 μm (without the bondpads).

Table 4.2: Measured pressure range, nominal resistance, TCR value for three Pirani tube geometries.

Length [mm]	0.4	1.6	3
Resistance [Ω]	85	240	390
TCR [ppm/K]	1320	1420	1470
Current [mA]	8	2.8	1.8
Pressure range [Pa]	2 - 2 M	0.2 - 0.2 M	0.1 - 0.1 M
Max. sensitivity press. $p_s = \sqrt{p_l p_h}$ [Pa]	2000	200	100

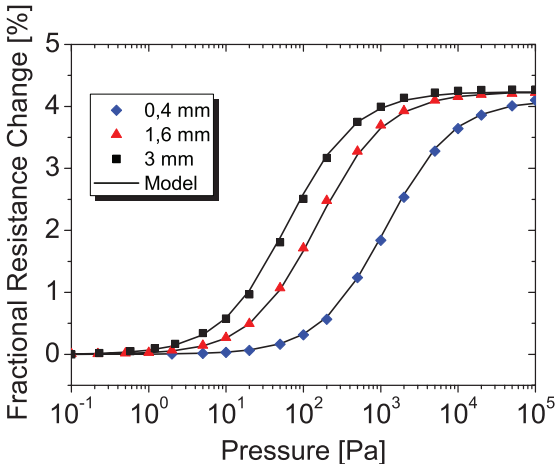

Figure 4.9: Fractional resistance change versus pressure on a semilogarithmic scale for three tubes with different lengths. The measurements agree very well with the model curves.

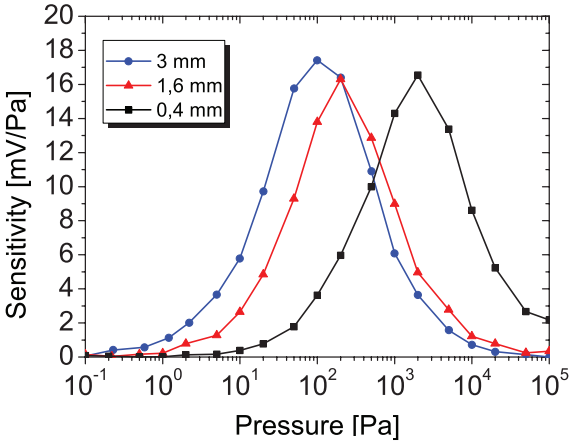

Figure 4.10: Sensitivity versus pressure. The maximum sensitivity is approximately 17.5 mV/decade for all the three tubes.

arithm. The maximum sensitivity is approximately 17.5 mV/decade and it is the same for all the three tubes. For the 3 mm long tube the pressure of maximum sensitivity falls around 100 Pa as designed. It is around 200 Pa for the 1.6 mm long tube and around 2000 Pa for the 0.4 mm long one, respectively.

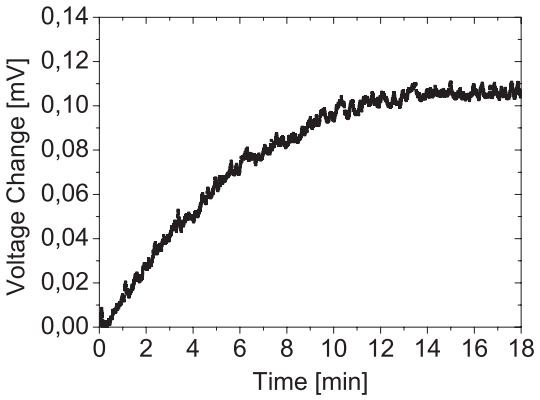

Figure 4.11: Output voltage versus time for the 3 mm long tube biased by a constant current of 2 mA.

Fig. 4.11 reports the output voltage of the sensor versus time, when the sensor is biased by a constant current. The voltage increase related to the resistance increase is due to an augmentation of the resistor temperature over time. We believe that the thermal drift is mainly due to the slow heating up of the silicon substrate around the Pirani tube. In order to reduce this effect, a pulse measurement was performed. Before choosing the pulse width, the time response of the sensor was measured applying a square wave current. A time constant of 0.1 ms was obtained. Consequently, a pulse of 200 ms was used to perform the sensor calibration.

The lower and upper limit of operation is set by N and in our case it is dominated by the voltage resolution of the Keithley source meter. In order to better visualize how this voltage resolution affects the dynamic range of the device, the data are plotted on a voltage-pressure double-logarithmic plot (Fig. 4.12). The dashed horizontal line at 50 μV represents N). As can be seen, the match with the values from the model is very good.

The 0.4 mm long tube shows a low pressure limit of 2 Pa, whereas the tube of 1.6 mm shows a low pressure limit of 0.2 Pa. For the 3 mm long Pirani tube, the low pressure limit of the dynamic range is at 0.1 Pa and it coincides with the resolution of our vacuum measurement system (pressure values less then 0.1 Pa could not be measured accurately). For the 3 mm

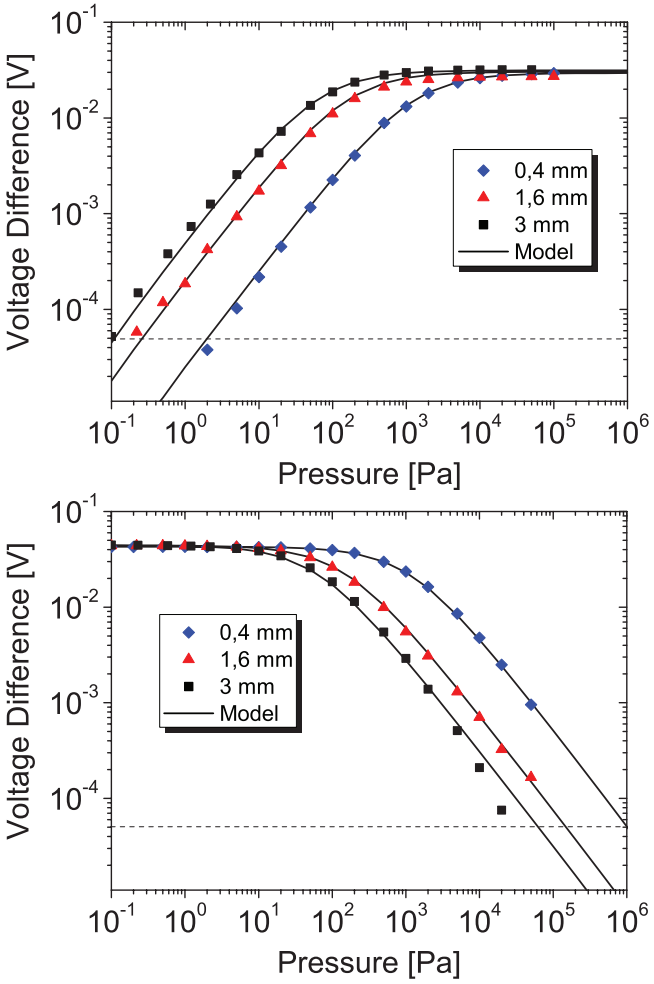

Figure 4.12: Double-logarithmic Voltage-Pressure plot representing the transfer functions $v_1(p) = V_{max} - V(p)$ (graph above) and $v_2(p) = V(p) - V_{min}$ (graph below) for the three Pirani gauges. Considering the interception of the dashed horizontal line representing N with the transfer functions, the values of the low and high pressure limits are obtained.

long tube the high pressure limit is 0.1 MPa, whereas the 1.6 mm tube can resolve pressure measurements up to 0.2 MPa. It was not possible to measure the high pressure limit for the 0.4 mm long tube since the measurement setup is not suitable for pressures higher than ambient. Yet again an extrapolation gives a value of 2 MPa which is close to the calculated one. The dynamic ranges are summarized in Table 4.2.

The 3D-shaped Pirani tube can indeed reach a low detection limit without increasing the chip area. A comparison with literature in terms of detection limit and footprint is shown in Table 4.3. The 3-mm long Pirani tube presented has a footprint of only 0.012 mm^2, which is an improvement of at least 20 times compared to Pirani gauges with the same detection limit. To make full advantage of the reduced footprint in many applications it is necessary to fold the tube into e.g. a spiral shape (saving chip area). However, care should be taken that thermal expansion of the tube does not close the gap in the curvatures and that the folding density is limited by the tube width (30 μm) below the surface. However, as the tube is buried, a large part of the silicon region upon it can be used as active chip area.

Table 4.3: Footprint and detection limit of Pirani gauges

Researcher	Geometry	Footprint [mm^2]	Detection limit [Pa]
Stark et al. (2003) [63]	Platinum on membrane	0.25	0.13
Stark et al. (2005) [66]	Poly Bridge (serpentine)	0.10	1.3
Mitchell et al. (2008) [40]	Poly Bridge (ladder struct.)	0.50	0.13
Topalli et al. (2009) [54]	Silicon Bridge	0.56	1.3
This work	Buried Tube	0.012	0.10

4.5 Conclusions

We have designed and fabricated a novel micromachined Pirani vacuum gauge with low detection limit but with a strongly reduced footprint. This was obtained by employing a tube-shaped 3D geometry buried in the substrate that increases the structural rigidity by approximately 10^4 times compared to a bridge-based Pirani gauge with the same footprint.

The Pirani tube was designed by extending the model presented in chapter 3 to the tube geometry. A three-masks process is used to realize this new geometry. The high stiffness of this geometry allows the fabrication of Pirani tubes with lengths up to 3 mm and with 1 μm gap, free of buckling and/or stiction. Pressure measurements could be resolved from approximately 0.1 Pa to 0.1 MPa. For the 0.4 mm long tube the measured pressure range goes from 2 Pa to 2 MPa, while for the tube of 1.6 mm it goes from 0.2 Pa to 0.2 MPa. Our longest Pirani gauge is 3 mm long and it has a footprint of only 0.012 mm^2. It shows a pressure range from 0.1 Pa to 0.1 MPa. The maximum sensitivity is 17.5 mV/decade. Measurements of the fabricated devices show a good agreement with the analytical model.

The possibility to fabricate Pirani gauges with low detection limit and extremely reduced footprint makes the device ideal for in-situ evaluation of MEMS vacuum packaging. The next chapter deals with the integration of such tube-shaped Pirani gauge with the thin film encapsulation process reported in chapter 2.

Chapter 5

Thin Film Encapsulation with in-situ Hermeticity Monitoring

5.1 Introduction

MEMS devices often require to be hermetically packaged under a certain environment (see Table 5.1) or to operate in vacuum [1]. This is needed for instance to achieve a reduction of damping and temperature effects, low power consumption, long term stability. In fact, the pressure of the cavity plays an important role in tuning the operating characteristics of the encapsulated MEMS device.

The vacuum level present inside a package is determined by two factors. The residual gas pressure, which is the pressure of the gases enclosed in the system just after the sealing step, and the flux of gases that over the lifetime of the device can change the initial vacuum level. The main contamination sources that cause vacuum degradation can be divided in three categories [1]:

- Leakage; the gas which penetrates into the package as a result of leaks. It is a flux of contaminants from the external environment due to micro-defects in the sealing process.

- Outgassing; the gas coming from the materials present in the package. The outgassing flux is a continuous releasing of contaminants from the internal surfaces that is relevant also at room temperature. In fact, the surfaces of the internal material work as sink due to the

Table 5.1: Vacuum requirements for MEMS [2]

Sensor type	Working pressure
Accelerometer	$\approx$ 300-700 mbar
Absolute pressure sensor	$\approx$ 1-10 mbar
Resonator (angular rate)	10^{-1} - 10^{-4} mbar
Gyroscope	10^{-1} - 10^{-4} mbar
RF switch	10^{-1} - 10^{-4} mbar
Microbolometer	$\leq 10^{-4}$ mbar
Optical MEMS	moisture free
DMD-DLP	moisture free

physisorption process [81] and slowly release the contamination cumulated during the previous exposition/treatment, thus increasing the internal pressure over time.

- Permeation; the gas entering the system through the capping layer. The permeation flux is a continuous influx of contaminants from the external environment due to the natural ability of the device encapsulation material to conduct molecules.

The internal pressure is a thermodynamic equilibrium condition in which the sorption of the contaminant is equilibrated by the natural desorption of the gas itself, that cannot be fixed by the solid during the residence time. For this reason, the choice of the materials used for the sacrificial layer, the capping layer and the sealing layer is crucial. For the hermeticity of thin film packages it is important not only to measure the pressures inside the package after the sealing step but it is also necessary to monitor it during long-term operation. Long-term stability and *in situ* vacuum measurements of micropackages are performed mostly by integrated sensors in the packages such as Pirani gauges [26, 40, 41, 54, 58–63, 66].

However, the integration of the Pirani gauges with the encapsulation process is challenging and not only in terms of process compatibility issues. It is noteworthy [24] that the encapsulation shell is the other heat sink of the Pirani gauge besides the silicon substrate. Its deflection, which changes the air gap between the Pirani gauge and the encapsulation shell, is dependent on the pressure of the environment. Since the calibration of the sensor is performed on an unsealed Pirani gauge placed inside a vacuum chamber, no shell deflection is present during calibration. This means that, the calibration curve cannot be used to perform accurate wafer-level measurements of the vacuum inside the micropackages. To overcome such problem, the sealed Pirani gauge is measured in a vacuum environment (die-level measurement),

where the deflection of the encapsulation shell is negligible [24].

In chapter 4 a new Pirani gauge employing a polysilicon tube buried inside the substrate was presented. The very low detection limit and reduced footprint make it ideal for hermeticity monitoring of micropackages. Moreover, since the Pirani gap is all around the tube and deep below the silicon surface, the encapsulation shell deflection is not a concern and wafer-level measurement of the device are possible.

The Pirani tube has been integrated inside micro-packages based on SiN thin-film encapsulation in order to measure the resulting vacuum level achieved after the encapsulation step. Particular emphasis is given to the fabrication process for the integration of the sensor with the encapsulation. The device is then calibrated and vacuum measurement for the fabricated micropackages shown. Furthermore the pressure is monitored over time to evaluate the vacuum degradation.

5.2 Encapsulation of the 3D Pirani tube

A sketch of the packaged sensor is depicted in Fig. 5.1. The gauge is encapsulated inside a microcavity, that consists of a rectangular plate clamped on a wall. The micropackage is designed to withstand 10 MPa (100 bar) of differential pressure. For this purpose, no pillars are needed because the footprint of the encapsulated Pirani is very small. In fact the distance between the opposite wall could be kept as small as 25 μm. A capping layer of 3.5 μm SiN was used. The sealing step was performed in a PECVD chamber at a deposition pressure of 400 Pa at 400°C. At room temperature a pressure of only about 180 Pa is expected in the micropackage if no vacuum degradation mechanisms are present. In order to measure different ranges of pressure, Pirani tubes with different lengths were designed.

The design of the sensors was performed according to the considerations presented in chapter 4. The tube consists of a stack of poly-Si and SiN layers. It is suspended on opposite ends with anchors at a depth of 5 μm under the silicon surface. The anchors provide mechanical stability and electrical contact for the Pirani gauge through the capping layer.

The tubes differ for their length, but they have the same thickness, gap size and tube radius. Considering the specifications on the required pressure range and the boundary conditions concerning the stress and the dissipated power, the geometrical parameters of the sensor were calculated. Since our Pirani consists of a stack of two different materials, the effective values for Young's Modulus, intrinsic stress and thermal conductivity were considered as explained in chapter 3; the main parameters are listed in Table 5.2.

The length L and the biasing current I for such Pirani tubes are listed in the Table 5.3. The longest Pirani gauge has been designed to measure a pressure range going from $p_l = 0.1$ Pa to $p_h = 0.1$ MPa, considering a voltage detection limit N of 50 μV. The critical stress for buckling σ_c for such Pirani tube is set at three times larger than the thermal induced stress. It is 1.6 mm long with $r = 20$ μm, $t = 1.8$ μm and biased by a current of 2.5 mA. The Pirani tubes of 0.8 and 0.4 mm have been designed for measuring ranges going from 0.2 Pa to 0.2 MPa and from 1 Pa to 1 MPa, respectively.

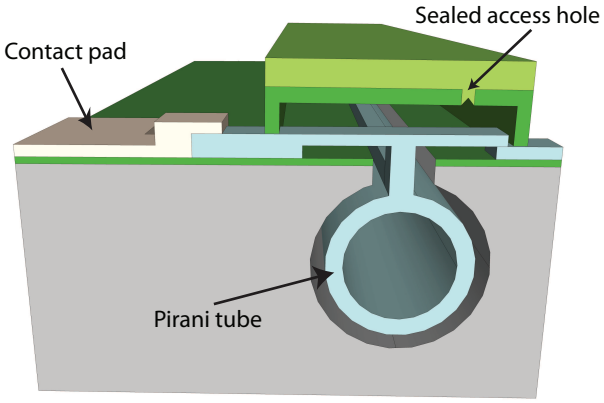

Figure 5.1: Sketch of the encapsulated Pirani gauge tube.

Table 5.2: Material parameters used in the model. Effective values are considered for Young's Modulus (E_{eff}), thermal conductivity (k_{eff}) and thermal expansion coefficient (c_T); ρ is the electrical resistivity of poly-Si and k_c is the thermal conductivity of nitrogen at atmospheric pressure.

c_T[-]	k_c[W/mK]	k_{eff} [W/mK]	ρ [Ω m]	E_{eff} [GPa]
2.7 μ	22 m	16	25 μ	230

Table 5.3: Biasing current and detection limit for Pirani tubes with three different lengths.

Length [mm]	0.4	0.8	1.6
Current [mA]	10	5	2.5
Detection limit [Pa]	1	0.2	0.1

5.3 Fabrication

The process flow is depicted in Fig. 5.2. The fabrication of the Pirani tube mostly follows the same process flow as presented in section 4.3. After the wet etching of the cylindric cavity in the silicon substrate (Fig. 5.2a), the masking silicon nitride is removed by H_3PO_4. A different sacrificial layer is used in this fabrication process. A 2 μm poly-Si layer is deposited by LPCVD (Fig. 5.2b). Note that the deposition is also performed inside the trenches and the tubes.

After this deposition a wet etching of the poly-Si layer is performed to define the area for anchoring the tubes and the placement of the electrical connections. Then, a 200 nm SiN layer and a 600 nm polySi layer are deposited by LPCVD to achieve a conformal stack defining the Pirani tube (Fig. 5.2c). The deposited poly-Si will be used as semiconductor for the pressure sensors. The poly-Si is then doped by $POCl_3$ process. A uniformly doped poly-Si layer is achieved.

In order to embed the poly-Si tube within a SiN layer, a dry etching of the poly-Si and a 1000 nm SiN deposition followed. The SiN is used to provide the Pirani with the sufficient mechanical support giving the tube an overall tensile intrinsic stress. Moreover it is needed to protect the polySi during the sacrificial etching step and to close completely the trenches of the tube. Then, an other dry etching step is performed to define the Pirani area, followed by a sacrificial wet etching using KOH (33%) at 85°C (Fig. 5.2d).

Once the tubes are released, a 2 μm PECVD TEOS is deposited to build a new sacrificial layer for the encapsulation process (Fig. 5.2e). Trenches for the walls and the columns are etched at the same time in the TEOS layer landing on SiN. For this etching step BHF 1:7 is used. Then, a 1000 nm SiN is deposited by LPCVD to define the walls and the pillars (Fig. 5.2f). The access holes are dry etched into the SiN layer landing into the second sacrificial layer (see Fig. 5.3). The sacrificial etching to release the packages is done using a BHF 1:7 solution (Fig. 5.2g).

Finally the sealing of the access holes is done by 2.5 μm PECVD SiN (see Figgs. 5.4-5.5). The pressure at which the deposition is performed will contribute to determine the quality of the vacuum inside the packages.

The contact opening for the electrical connections with the tube are realized with a dry etching step. The SiN is etched down landing on the poly-Si. Then aluminum is deposited by sputtering and it is patterned to define the shape of the aluminum pads and interconnections.

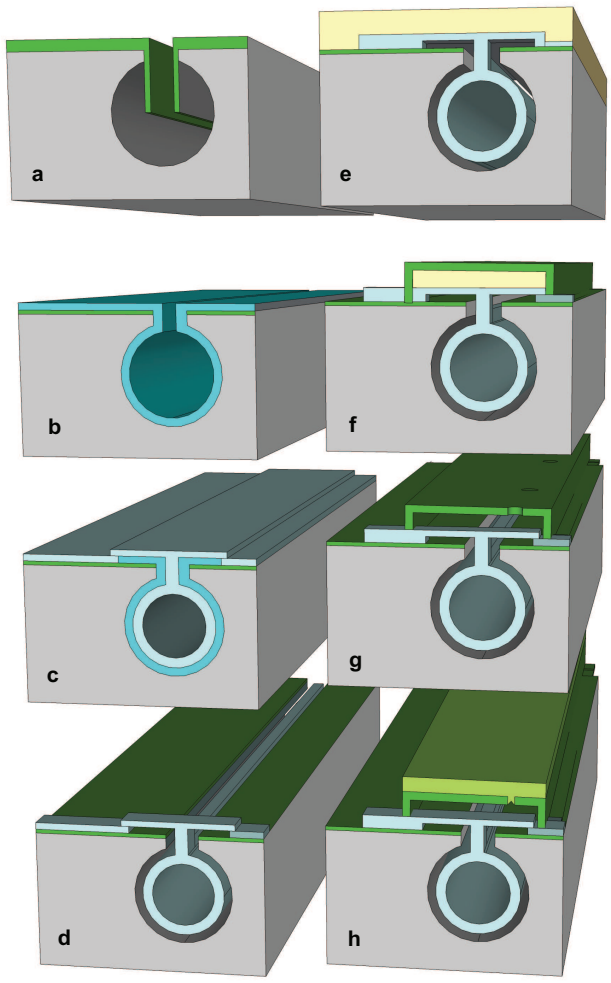

Figure 5.2: Schematic flowchart.

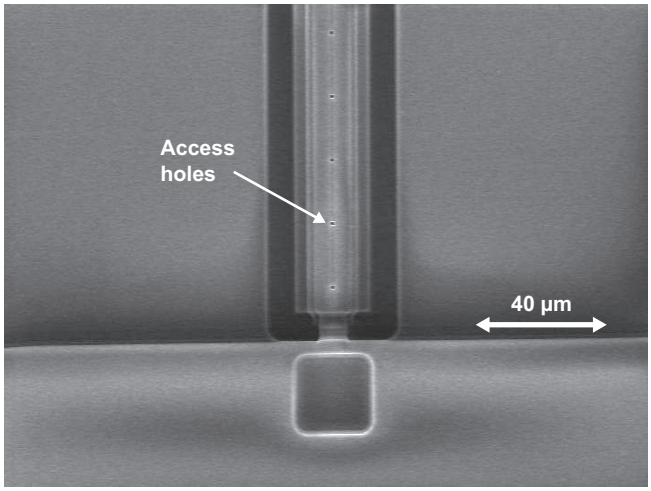

Figure 5.3: SEM top view of the encapsulated Pirani tube before sacrificial etching.

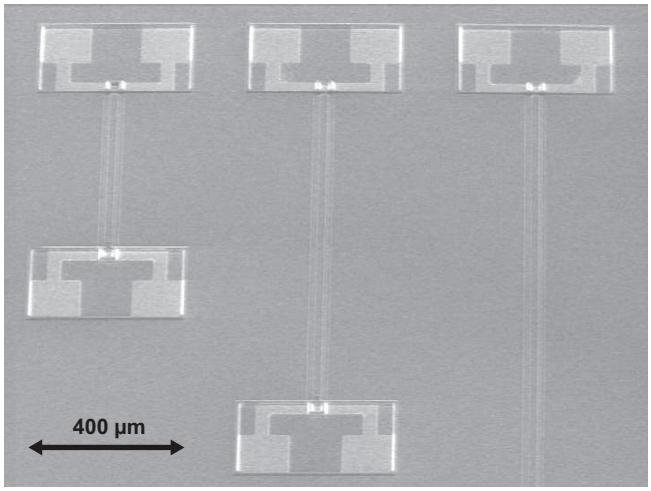

Figure 5.4: SEM top view of the encapsulated Pirani tube.

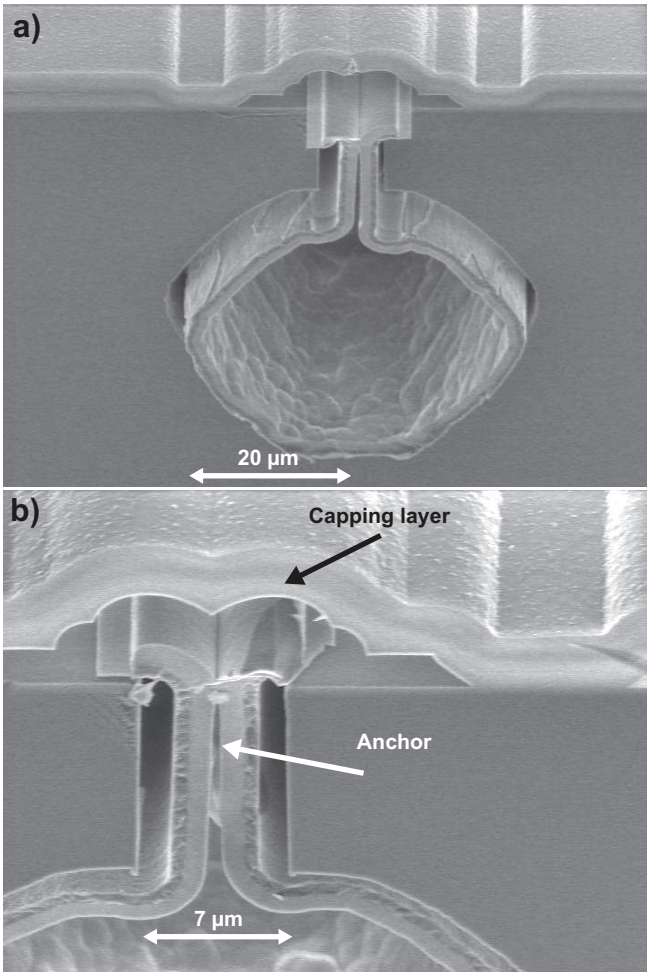

Figure 5.5: SEM images of the encapsulated Pirani tube. a) cross section and b) close-up of the anchor.

5.4 Measurement Results and Discussion

For pressure calibration the micropackages were vented by etching a hole into the SiN capping layer. The measurement setup presented in section 3.5 was used. A schematic of the calibration setup is depicted in Fig. 3.6. During the sealing step, a gas mixture comprising nitrogen, silane and ammonia ($N_2/SiH_4/NH_3$= 1000/280/1800 sccm) is used. Since ammonia and nitrogen are in a much larger quantity compared to silane and since they have very similar thermal conductivity, the calibration of the sensor was performed in nitrogen.

Considering the measured TCR values, the biasing current was chosen to generate the same average temperature across the tubes with different lengths in order to compare their performance. In Fig. 5.6 the calibration curves of the 0.4, 0.8 and 1.6 mm long Pirani tubes are reported in terms of fractional resistance change $\frac{R(p)-R_0}{R_0}$. The measurements of the nominal resistance of the Pirani tubes R_0 across the wafers show a deviation of about 2%. It is most probably due to a non-uniformity of the etching steps between the edge and the center of the wafer. This means that all the devices should be calibrated before usage to reduce measurement errors. Since the

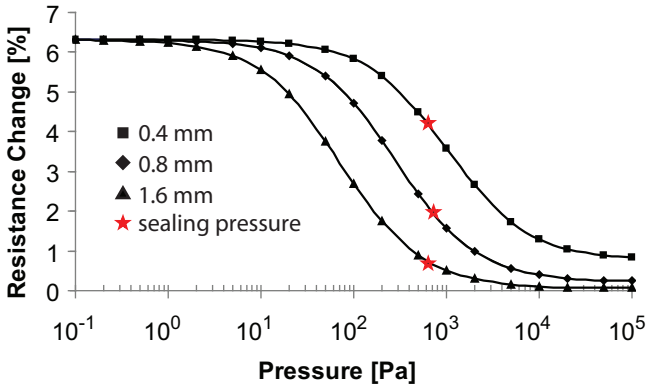

Figure 5.6: Calibration curves of the three Pirani tubes. The red marks (*) represent the fractional resistance change of the sealed Pirani gauges.

Pirani gap is below the silicon surface, the deflection of the capping layer of the micropackage due to the pressure difference is not influencing the gap size. For this reason, the encapsulated Pirani gauges does not need to be measured in vacuum but can be measured at wafer level (see Fig. 5.7). A Cascade probing station with an HP 4156C parameter analyzer was used for the pressure measurements on the encapsulated Pirani gauges. The vacuum

level achieved with the PECVD SiN sealing are reported in Fig. 5.6. By matching the resistance of the Pirani gauge while sealed with the calibration data obtained in the pressure-controlled chamber, the pressure inside the sealed micropackage was extracted to be around 0.7 kPa. It should also be noticed that the three tubes measure approximately the same vacuum level (from 0.65 to 0.75 kPa).

Since a vacuum level of 180 Pa was expected right after the PECVD SiN sealing step, a vacuum degradation occurred afterwards. In fact, during the further thermal processing steps like aluminum sputtering (350°C) and alloying (400°C) outgassing occurred affecting the vacuum level of the micropackage. This is also in agreement with a more fundamental study concerning the outgassing of hydrogen from PECVD SiN layer presented in [82].

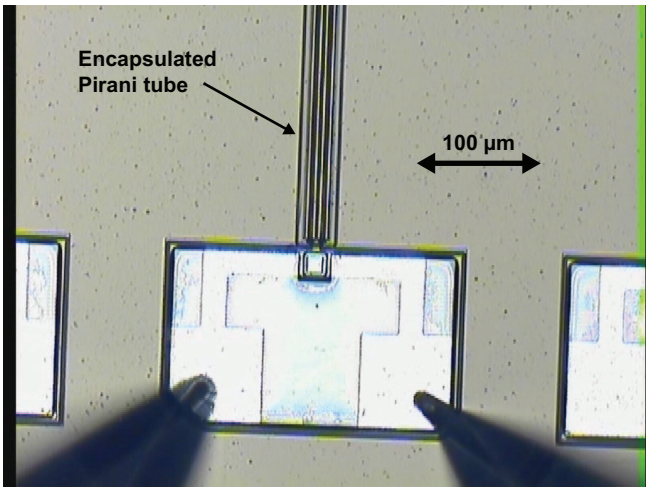

Figure 5.7: Optical microscope picture of a packaged Pirani tube.

In order to give an estimation of the vacuum degradation, the vacuum level was monitored over time. In Fig. 5.8 the fractional resistance change of the three Pirani tubes is plotted over time. The 0.4 mm long tube shows the highest change (0.8%) between the nominal resistance value and the one in vacuum compared to the other two Pirani tubes, because it has the largest sensitivity at the vacuum level that is inside the micropackage. This can be also deduced from Fig. 5.6. According to such measurement a slight degradation of the vacuum occurred in four months time and a pressure raise of about 0.3 kPa can be inferred from the calibration curve of the 0.4 mm long Pirani tube. This gives a leak rate of $8{\cdot}10^{-18}$Pa m^3 s^{-1},

considering a micropackage volume of approximately $2{\cdot}10^{-13}$ m^3. However, also the nominal value of the Pirani tube resistance changes over time of about 0.2%. This value represents the detection limit for the measurement of the tube resistance over four months time. In terms of leak rate, the detection limit is $2{\cdot}10^{-18}$Pa m^3 s^{-1}. This value is still more than six orders of magnitude below the detection limit of a regular Helium leak tester.

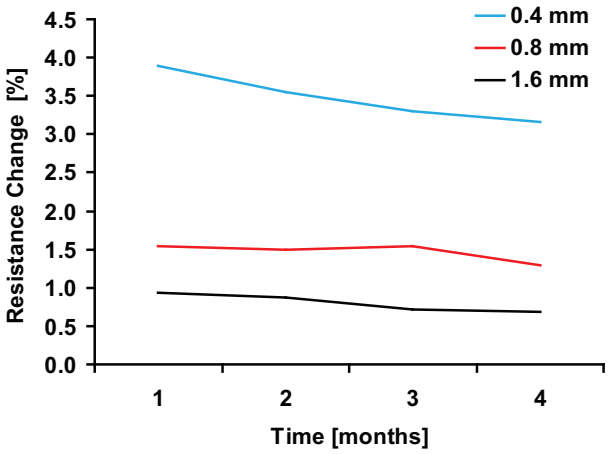

Figure 5.8: Vacuum degradation of the sealed micropackages. From the calibration curve a corresponding pressure change of 300 Pa is inferred.

5.5 Conclusions

The integration of the Pirani tube with the SiN encapsulation process was successfully demonstrated. Combining low detection limit and small footprint, the Pirani tube has proven to be suitable for in-situ evaluation of MEMS vacuum packaging. Pirani tubes with different lengths were encapsulated in order to measure different pressure ranges. The vacuum level achieved with the encapsulation was measured (0.7 Pa) and monitored over time. A leak rate of $8{\cdot}10^{-18}$Pa m^3 s^{-1} was measured over four months time.

PECVD SiN showed good sealing property for thin-film packaging. However, outgassing, at high temperature remains the main concern. When high vacuum is required, better sealing is obtained by using LPCVD deposition [16,19,20,24,25,27,28,30,31]. However, a significant amount of sealing material is deposited inside the microcavity, coating the device surface be-

cause such deposition technique is very conformal. In the next chapter, we describe a new technique for MEMS thin-film encapsulation that allows the LPCVD sealing without undesirable deposition of the sealing material on the inner surface of the microcavity.

Chapter 6

Sealing for thin-film encapsulation

6.1 Introduction

In the previous chapters, mechanical robustness and hermeticity monitoring of thin-film encapsulation were discussed. Another important issue to be addressed regards the sealing of sacrificial etching holes (see Fig. 6.1a-c). During this step a significant amount of sealing material could be deposited on the device surfaces (see Fig. 6.1a,b). For some devices, this can alter or deteriorate its proper working behavior. Thus small access holes are preferable if allowed by lithography and the structure or device function. In [24] a free-standing porous membrane was used as capping layer. The sacrificial layer is removed through the nanopores, which are sealed by a further deposition step. In this way the amount of material deposited inside the cavity is reduced.

For sealing techniques such as PECVD, although the vacuum achieved is not very high, the deposition is quite directional and as long as the access holes are not placed on top of the device area, no deposition will occur upon the device. In some cases instead of the access holes, channels are used and placed all around the device area (see Fig. 6.1c). However, this approach may require long etching time of the sacrificial layer, thus a sacrificial material that can be etched with very high etching selectivity must be chosen.

PECVD SiN was used for sealing the packages dedicated to the mechanical tests discussed in chapter 2. It showed very good mechanical robustness. Moreover, PECVD SiN was also used for the encapsulation of the Pirani

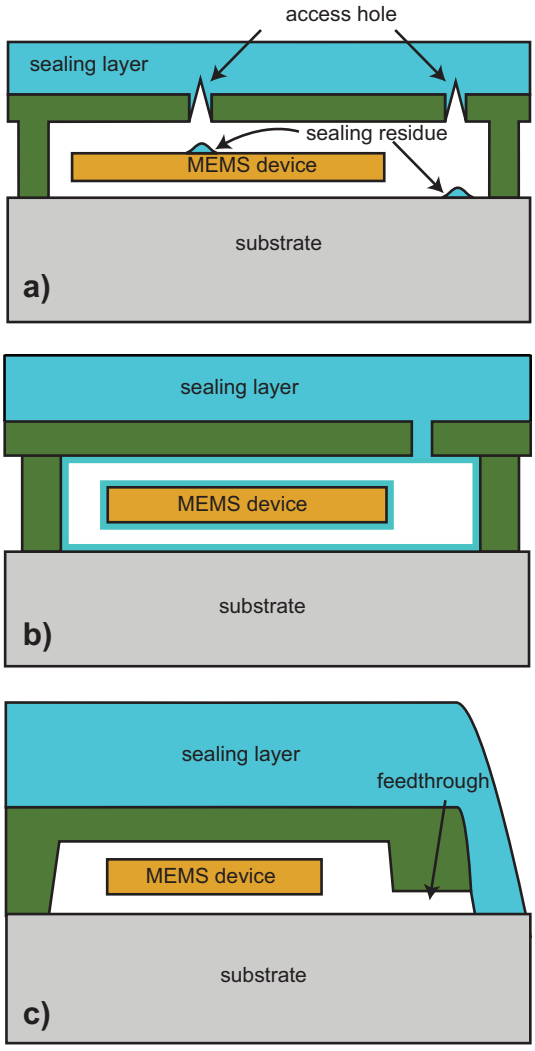

Figure 6.1: Sealing of access holes in thin-film encapsulation. a) Undesired material is deposited on the MEMS device. b) Sealing by means of conformal deposition technique such as LPCVD. c) Sealing of lateral access channel by non-conformal deposition technique such as PECVD.

tube, as showed in chapter 5. The vacuum measurements were acquired by the Pirani gauges and a vacuum level of 0.7 Pa was measured and monitored over time. This value is low enough for many applications (see table 5.1), showing that SiN has good sealing property for thin-film packaging.

However, when higher vacuum is required, a better sealing can be obtained by using LPCVD deposition [16,19,20,24,25,27,28,30,31]. The high temperature and high vacuum during the deposition ensure vacuum sealing with long term hermeticity. Besides the limitations due to the thermal budget, another drawback is the significant amount of sealing material deposited inside the microcavity and coating the device surface (see Fig. 6.1b). This is due to the high conformality that is achieved with this deposition technique: even using very small access holes, some deposition will occur inside the microcavity.

Furthermore, in any thin-film encapsulation approach presented in literature, the gas composition inside the microcavity is highly dependent on the gases used during the deposition of the sealing layer, as those gases remain trapped inside the microcavity. A new sealing technique for the thin-film encapsulation of MEMS under arbitrary pressure conditions and gas composition and with no deposition on the device surface, is presented.

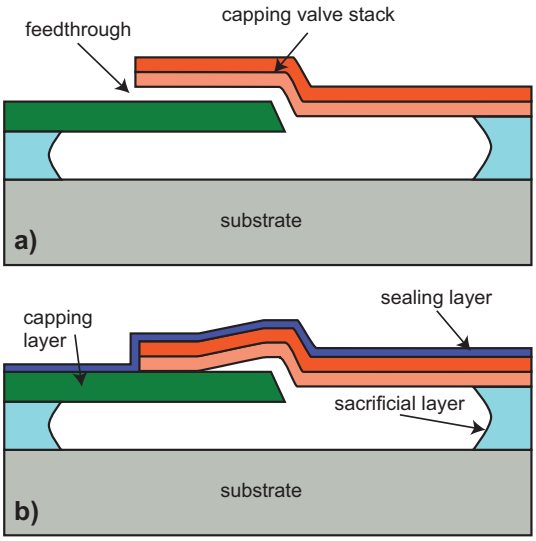

Figure 6.2: Schematic configuration of the self-sealing thin-film microcavity; a) before and b) after final sealing layer deposition.

Table 6.1: Young's modulus E, Poisson's ratio ν, intrinsic stress σ_i and thermal expansion coefficient C_{TE} of SiN and poly-Si.

Material	E [GPa]	ν [-]	σ_i [GPa]	C_{TE} [ppm/K]
SiN	329	0.3	0.2	3.3 [83]
poly-Si	160	0.3	-0.04	2.7 [84, 85]

6.2 Design

The new sealing technique is based on a capping layer containing thermally actuated valves to close the sacrificial holes before the deposition of the sealing layer (see Fig. 6.2). The capping layer consists of a stack of two layers with different thermal expansion coefficients. After performing the sacrificial etching, the device is released and sealing can be performed in any CVD chamber.

The sealing procedure consists of three steps and starts with a pumping down to provide the required vacuum (or more in general, the required gas environment) inside the microcavities. In this step the time should be sufficiently long to fully evacuate the air inside, prior to vacuum sealing. Then a thermal step follows, during which the capping layer bends down and the valves close. Finally a layer deposition will take place to improve the sealing. Since the valves are closed, no deposition occurs inside the microcavities during this final sealing step. This approach is compatible with most thin-film encapsulation processes and it is very versatile as different combinations of materials can be chosen for the thermal actuation layers stack.

6.2.1 Thermal actuation of the capping layer

A stack of poly-Si and SiN was chosen as capping layer. The thickness of the cap of the microcavity was chosen to be 1 μm (0.5 μm SiN and 0.5 μm poly-Si). The difference in the thermal expansion coefficient of the two materials generate a deflection of the capping layer. Finite element (FE) simulations were performed to better estimate the bending. The intrinsic stress of the layers was taken into account. Its value was measured on test wafers with the curvature method. The parameters used for the simulation are listed in Table 7.1. According to the simulation, the poly-Si/SiN stack should bend down by 0.5 μm along a distance of 25 μm with a temperature increase of about 400°C (Fig. 6.3). For this reason, the gap was designed to be only 0.5 μm. The length of the feedthrough was varied between 5 μm and 40 μm.

6.2.2 Evacuation time

One important design issue regards the amount of time required for the package to fully evacuate the air inside, prior to vacuum sealing. If not designed correctly the time to evacuate can be unreasonably large. To model evacuation times, the package can be treated as a fluidic capacitor, with the fluidic feedthrough as resistor, as was done in [21]. This approximation is valid only down to pressure levels of few millibars, because at lower pressure values the molecular flow regime should be considered since the fluid cannot be treated anymore as a continuous medium.

Under these simplifications, the system becomes a RC circuit. The time to evacuate the cavity is given as

$$\tau = RC, \quad R = \frac{12\mu L}{wt^3}, \quad C = \frac{V}{R_g T} \tag{6.1}$$

where μ is the viscosity of the air, L is the length of the feedthrough, w is the feedthrough width, t is the feedthrough height, V is the volume of the cavity, R_g is the air gas constant, and T is the temperature. An important point to note is that the fluidic resistance depends upon the third power of the feedthrough height. For this reason, if a thinner feedthrough gap is used, the evacuation time would easily become unreasonably long.

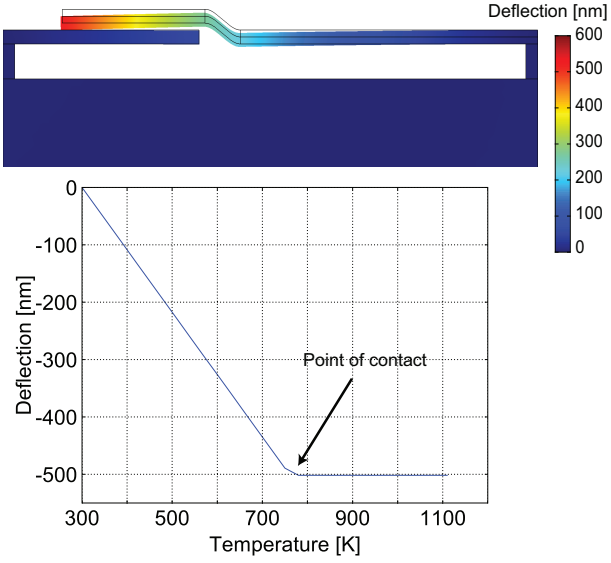

Figure 6.3: Finite element simulation of the actuation principle.

6.3 Fabrication

The fabrication process requires only one mask more than conventional thin-film encapsulation process. It is illustrated in Fig. 6.4. First a 2.5 μm silicon oxide sacrificial layer is deposited by PECVD (Fig. 6.4a). A lithographic step is then performed and the trenches for walls and pillars are etched into the sacrificial layer by RIE. Pillars and walls are defined by means of a LPCVD deposition of SiN (1 μm thick) in the trenches. Then a RIE etching step in the capping layer is performed (Fig. 6.4b) landing on the sacrificial layer defining the anchor of the valve, and a 0.5 μm silicon oxide sacrificial layer is deposited by LPCVD (Fig. 6.4c). At this stage, the thermally actuated capping layer is deposited (Fig. 6.4d). It consists of a layer stack made out of LPCVD poly-Si and SiN. This capping layer is then dry etched to define the shape of the thermally actuated valves.

The releasing of the structure is then performed in HF 40% solution for 40 minutes (Fig. 6.4e). Once the sacrificial etching is finished, the sealing is done by using an LPCVD furnace (Fig. 6.4f). As explained previously, the sealing procedure consists of 3 steps: first the pumping down is needed to fully evacuate the air inside the package prior to vacuum sealing. This suggests that the initial pressure inside the packages is around 10 Pa at room temperature. Then the temperature rose up to 850°C, so that the capping layer bends down and the valves close. Finally a 50 nm LPCVD SiN deposition is made to improve the sealing (Fig. 6.5).

6.4 Results

The surface profile of the capping layer was measured at different temperatures to characterize its actuation bending (Fig. 6.6) by means of white light interferometry. A bending of about 1.3 nm per degree was measured. This means that with the designed geometry it is possible to close a gap of more than 1 μm with a temperature increase of 800°C; this is in good agreement with the simulation results. This is also confirmed by the SEM inspection. Fig. 6.5 show the SEM cross sections after the sealing step. The 0.5 μm feedthrough gap is closed and no SiN deposition is observed inside the microcavity.

6.5 Conclusions

A new sealing technique for MEMS thin-film encapsulation was discussed. It allows to perform the encapsulation step under arbitrary pressure condi-

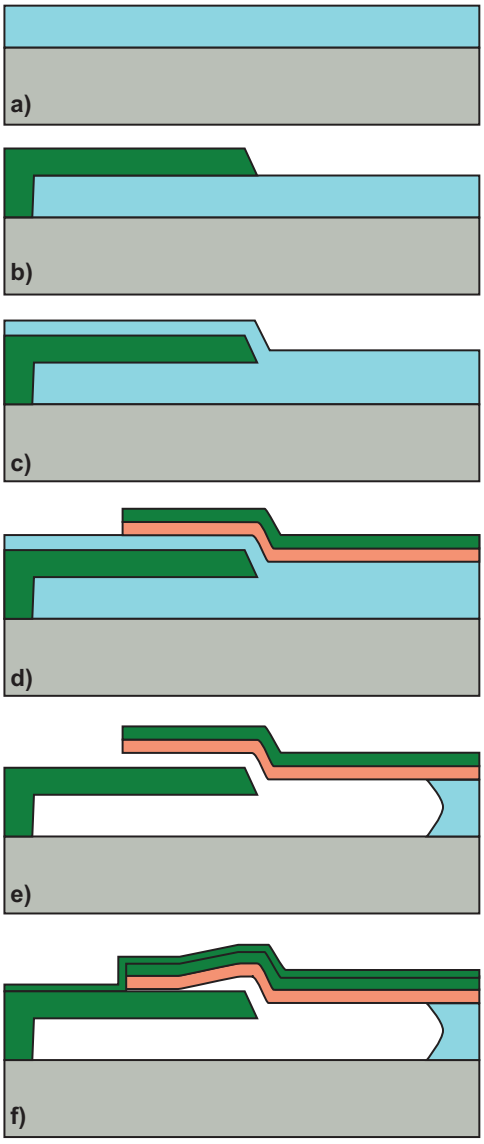

Figure 6.4: Main steps of the process flow.

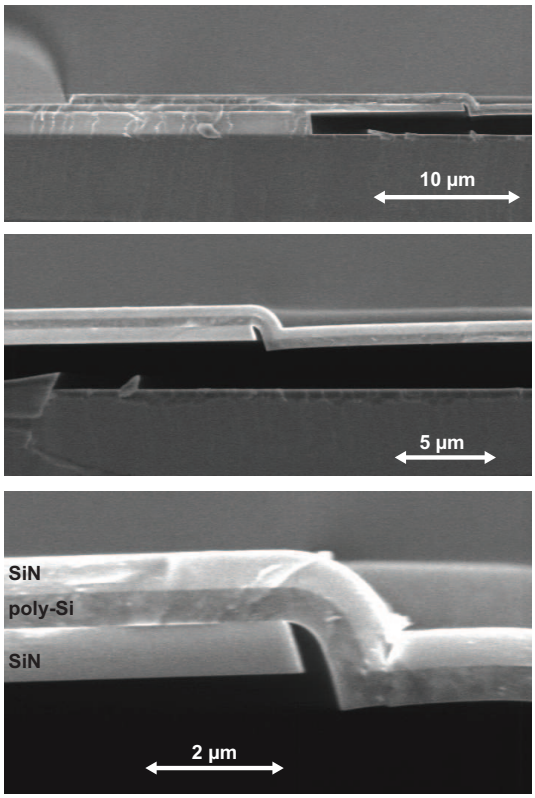

Figure 6.5: SEM cross section of the microcavity after sealing, showing the bending of the capping layer. No deposition inside the cavity is visible.

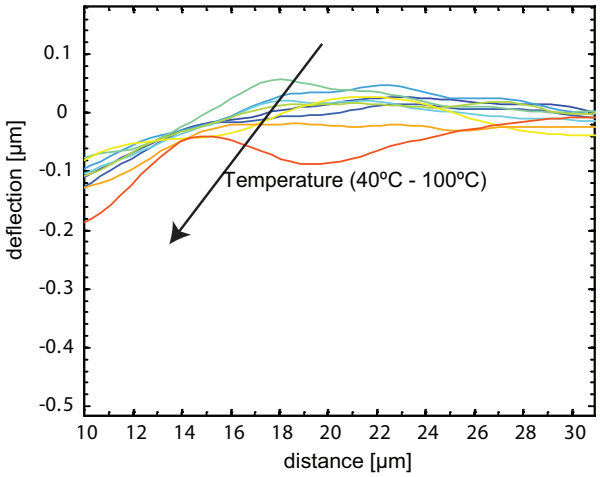

Figure 6.6: Deflection versus temperature. The measurement is affected by the surface measurement error from the white light interferometer (see [86]).

tions without unwanted deposition on the device surface. Compared to the conventional plugging techniques, it requires more fabrication steps. However, this approach becomes very useful when an LPCVD deposition needs to be used for the sealing step. Microcavities were designed and fabricated to validate the proposed concept. Package with a 0.5 μm feedthrough gap were closed and no deposition was observed inside the microcavity after SEM inspection. Deflection measurements versus temperature also confirmed the validity of the presented approach.

Chapter 7

Thin Film Encapsulation of MEMS devices

7.1 Introduction

In the previous chapters, both mechanical robustness and hermeticity monitoring for thin-film encapsulation were addressed. The goal was to provide the package designer with guidelines for the dimensioning of both the thin-film package and the Pirani gauge to be integrated into the package.

To illustrate the potential applicability, the next step is to provide examples of process integration of the presented encapsulation approach with different MEMS devices. The encapsulation design has to be performed together with the design of the MEMS device to be encapsulated. Two devices, a MEMS electron source and an infra-red detector are considered. These examples show how the developed thin-film approach can be applied to different applications with different requirements in terms of robustness and hermeticity.

First, a MEMS electron source built within a single silicon wafer is presented. This device consists of a hermetically sealed microcavity that encapsulates an array of field emission silicon tips and a reaction chamber to which the emitted electrons are accelerated.

Then, as second example, thin-film encapsulation of an infrared detector for microspectrometers is presented. A SiN layer deposited at high temperature is used both as capping and sealing layer. By encapsulating the device in vacuum an improvement of sensitivity can be achieved.

7.2 Encapsulation of a MEMS Electron Source

Free electron sources are needed in many applications like e-beam based material analysis [87], e-beam lithography [88], displays, but also sensing devices like vacuum gauges [89] and flow sensors [90], etc. However, for handling stable electron emissions, high vacuum conditions are needed, which require complex (and thus expensive) systems. Fabricating electron sources using MEMS leads to strongly miniaturized devices with performance and cost benefits. Consequently, the requirements for the vacuum are significantly relaxed. A schematic configuration of such a micromachined electron source is showed in Fig. 7.1.

A range of applications need emitted electrons traveling towards a region under controlled pressure and temperature conditions. Therefore, an electron source needs a vacuum chamber in which electrons are emitted, a reaction chamber to which the electrons are accelerated and an electron transparent membrane in between them [91].

In [87] a device without reaction chamber has been presented. The cavity was fabricated by wafer bonding. Here a sealed microcavity used as vacuum chamber, and a microfluidic device used as reaction chamber, have been integrated on a single substrate using an IC-compatible surface micromachining process [44, 92]. In comparison to the bonding technique [87] the thin film approach allows to achieve field emission at voltages that are two orders of magnitude lower because of the reduced distance between emitters and electrodes.

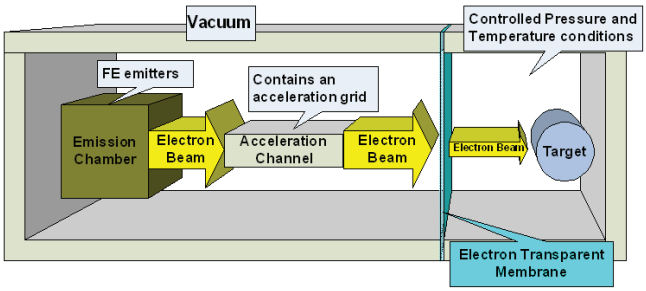

Figure 7.1: Schematic configuration of a micromachined free electron source consisting of a vacuum chamber containing the emitters and a reaction chamber to which the electrons are accelerated. The chambers are divided by an electron transparent membrane.

7.2.1 Design

A schematic configuration of the electron source device is shown in Fig. 7.2. The main elements of the device are the tip, the electron transparent membrane, the electrodes and the insulating pillars between them. Each tip is 3 μm high and has a base radius of 4 μm. SiN was selected as material for the membrane. The chosen membrane thickness is 20 nm, the diameter is 2 μm.

SiN pillars with a diameter of 3 μm were designed to support the microcavity structures, to control the distance between each tip and its corresponding membrane and to isolate the two electrodes. A thickness of 1 μm for the SiN capping layer and a distance of 20 μm between the pillars were chosen. This thickness is enough to neglect the current leakage through the nitride layer.

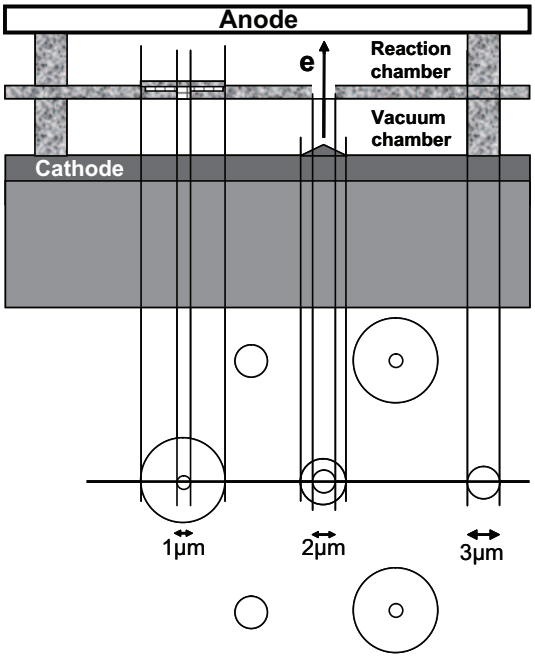

Figure 7.2: Schematic configuration (cross section and top view) of the device showing the electron emitter, the plugged access holes, and the pillars as circles.

7.2.2 Fabrication

The starting material is a silicon wafers with a 10 μm high- phosphor-doped epitaxial layer representing the cathode layer. The fabrication process starts with the tips definition (Fig. 7.3a-c). The doped layer is patterned with silicon dioxide circular pads and isotropically dry etched by using SF6 into a narrow neck column. The narrow-neck is then thermally oxidized until silicon tip is formed under the oxide layer. This extra oxidation step is used in order to sharpen the silicon tip [93].

To form the vacuum chamber (Fig. 7.3.d), thick PECVD borophosphosilicate glass (BPSG) is deposited on the oxidized narrow-neck structure and allowed to reflow. The previous oxidation step forms also a barrier to the diffusion of the dopants in the following high temperature steps. The BPSG deposition and reflow can be repeated in order to achieve a good planarization result. Using this technique a height difference of 5 μm was reduced down to 200 nm. The next step is the deposition of a thin LPCVD low-stress silicon nitride layer followed by a PECVD silicon dioxide layer. The SiN layer will serve as the electron transparent membrane and the SiO_2 layer will act as etch stop layer during the further membrane etching step.

To fabricate the pillars (Fig. 7.3.e-f), the stack of layers (SiO_2 + SiN + BPSG) is dry etched down to the silicon. Then low-stressed SiN to form the pillars and the capping layer was deposited. During the SiN deposition, cracks of the BPSG layer are observed. A good reflow/annealing step before the SiN deposition reduces the cracking issue suggesting that the cause of the cracks is a large amount of gases trapped into the BPSG layer. This thick SiN layer is then locally etched to form 1 μm diameter access holes for further sacrificial etching, reaching the underlying BPSG (Fig. 7.3.g). The device is then submerged in HF solution for sacrificial etching of the BPSG layer thus forming the vacuum chamber. During the drying step, no stiction was observed thanks to the support of the pillars distributed all around the chamber. The released chamber is loaded in a PECVD oxide deposition system for performing the plugging step (Fig. 7.3.h). The deposition recipe is tuned to specifically seal the 1 μm access hole gap, while minimize its deposition inside the chamber.

The PECVD oxide is etched away everywhere leaving the plug structure and a further LPCVD SiN layer is deposited on top of the oxide plug in order to improve the hermetic sealing. After the sealing step the membrane etching step is performed (Fig. 7.3.i). A window pattern aligned to the top of the tip is dry etched through the stack of sealing and capping SiN layers landing on the buried PECVD silicon dioxide layer. Then a further wet etch step in HF to expose the SiN membrane was performed. The microfluidic chamber (Fig. 7.3.l) was fabricated using PECVD silicon dioxide as sacrifi-

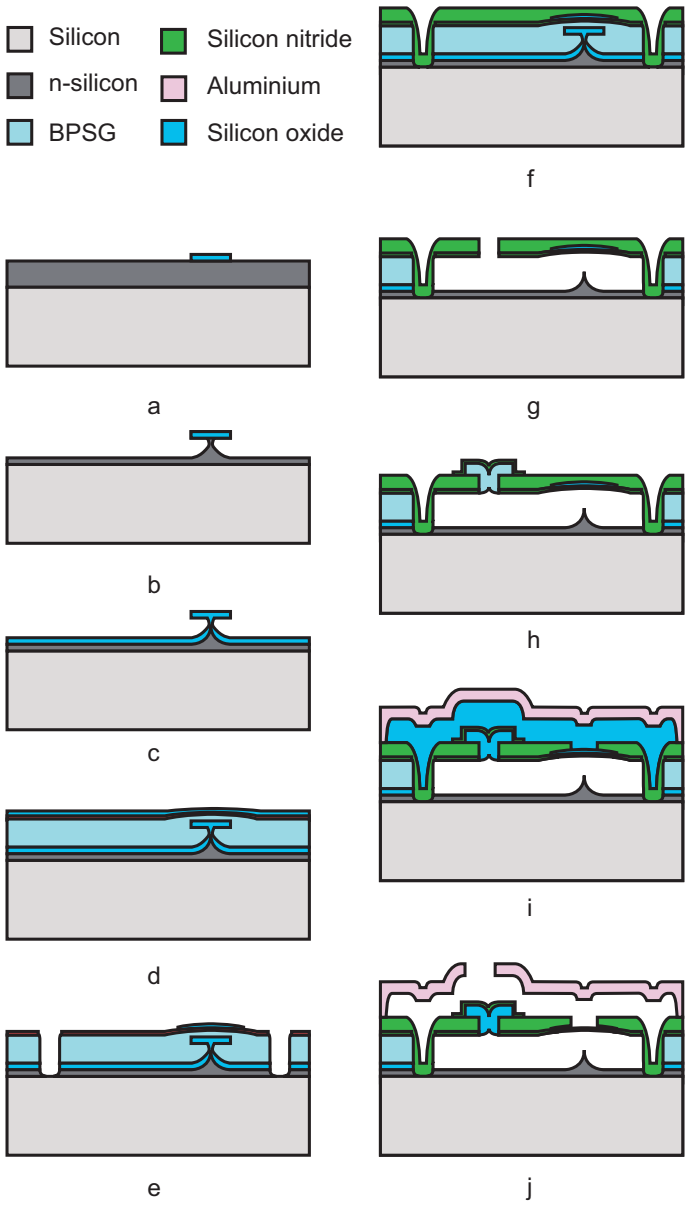

Figure 7.3: Main steps of the device process flow.

cial layer. An array of pillars was designed also for the reaction chamber in order to support the structure. Aluminum is used as anode for accelerating the emitted electrons from the vacuum chamber. A HF 73% solution was used to etch the sacrificial silicon dioxide because it is very selective towards aluminum. The Fig. 7.4 shows a SEM cross section of an encapsulated tip.

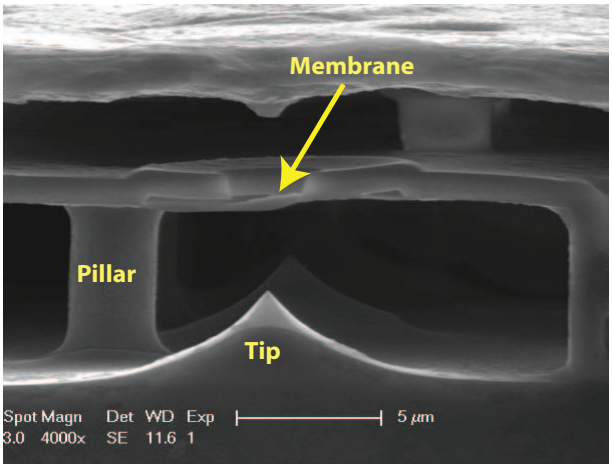

Figure 7.4: SEM cross section of encapsulated tips. The membrane window above the tip is in this case 50 nm thick here in order to withstand the cross section dicing process and to be visible in the SEM.

7.2.3 Measurements

To characterize the device, the emission characteristics of the electron source and the transmittance characteristics of the electron permeable membrane have to be studied. Here only the electrical characterization of the tips emission is reported. For this purpose test structures containing arrays with different number of tips, without permeable membranes, were considered. The experimental results are obtained using a Cascade probing station with an HP 4156C parameter analyzer. Field emission current versus anode-cathode voltage for a test structure containing 400 tips is shown in the Fig. 7.5.

For the single tip test structure, the cathode-anode voltage was varied from 0 to 70 V. The measured emission current at 60 V is about 0.1 A. The difference in the emission current between the single tip device and the one containing the tips array is about 100 times, and the array has overall less

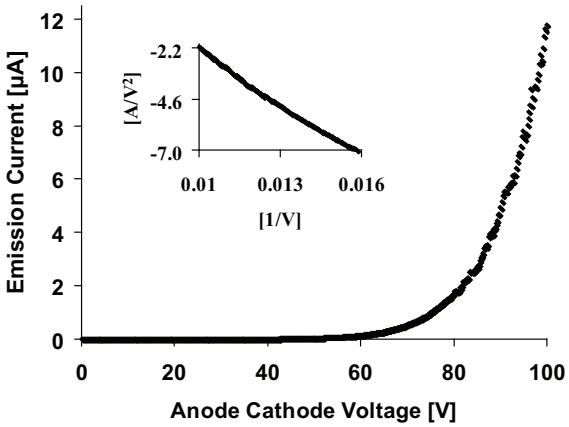

Figure 7.5: Field emission current versus anode-cathode voltage for a test structure containing an array of 400 tips. Inset: Fowler Nordheim plot.

fluctuation due to the effect of averaging. The Fowler-Nordheim plots shown in the inset of Fig. 7.5 demonstrates that the measured currents follow the Fowler-Nordheim tunneling model, proving that the encapsulation process did not negatively affect the emission properties of the tips. Fig. 7.6 shows an optical image of the working test structure containing the array of 400 tips. Long-term measurements were performed on a single-tip device to evaluate the stability of the field emission current (Fig. 7.7). An average emission current of 2.2 nA for 1 hour at 45 V cathode-anode voltage with a variation of 0.4 nA/hour was measured.

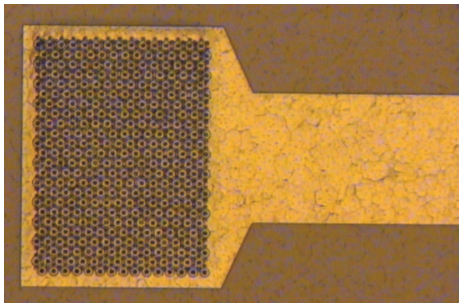

Figure 7.6: Optical image of the tested device (the tip array area is 260 μm*370 μm).

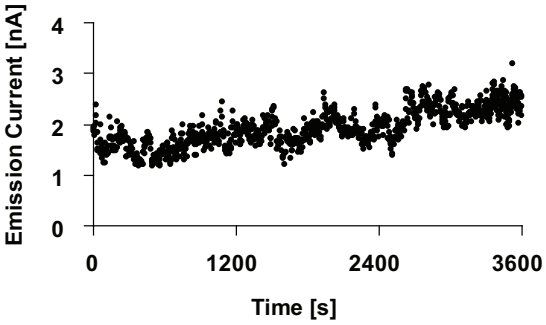

Figure 7.7: Stability measurement of a single tip test structure. The measured current is 2.2 ± 0.2 nA.

7.3 Encapsulation of an IR detector

IR micro-spectrometers, fabricated by IC-compatible MEMS technologies, are composed of an IR absorber, a temperature sensor and a grating or linear variable optical filter (LVOF) as the dispersive element (see Fig. 7.8). The temperature sensor consists of an array of thermopiles (TE) and the absorber is made out of a stack of thin-film layers.

The design of the elements in the thermopile-based IR detector for high performance requires a minimum thermal conductance between the absorber and the heat sink and also between adjacent absorber elements to reduce crosstalk [45, 94–96]. For this reason, micromachining technologies are generally employed for the removal of the bulk silicon or oxide underneath the TE detector so that the thermal shunt to the substrate is removed. Moreover, the absorbers are placed on adjacent beams rather than on the same membrane to reduce crosstalk. In this way the thermal conductivity through the layers is reduced to a minimum. However, in order to further improve the sensitivity, the thermal conductivity through the ambient gas has to be reduced as well. This can be done by encapsulating the detector array in vacuum.

For the thin-film encapsulation of the IR detector array, high temperature SiN was chosen for both the capping and sealing layer. The mechanical design of the encapsulation is done according to the approach presented in chapter 2. An array of columns are placed around the detector beams to increase the mechanical robustness of the structure. With vacuum an improvement of the performance is expected. Crosstalk should also enormously decrease when compared to devices operating in air.

7.3.1 Design

Thermopiles and absorber dimensioning

The design of the TE array and absorber were presented in [45]. Thermocouples are fabricated using n- and p-type polysilicon layers. The dimensions of each thermocouple leg are 190 μm $\cdot$ 4 μm. Five thermocouples form one thermopile on each TE element. The dimensions of the detector array are 1200 μm $\cdot$ 760 μm, with an absorber area at each TE element of 650 μm $\cdot$ 36 μm and spacing between elements of 46 μm. The width of a bridge was 36 μm and the spacing between bridges was 10 μm. The absorber is deposited in the middle position of the bridge with five thermocouples at the upper and lower side of the bridge. The interference absorber is composed of two metallic layers, a resonance cavity and a protection layer on top of the TE elements. The absorber is designed for maximum absorption in the

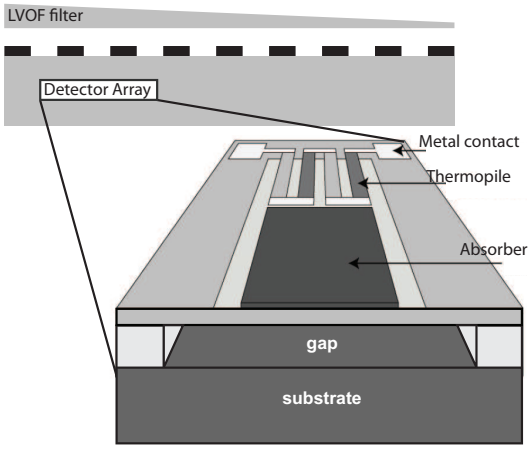

Figure 7.8: Schematic of a thermopile MEMS IR detector.

near- and mid-IR range from 1 to 5 μm [45]. The absorber consists of one dielectric center layer with thin-film metallic layers on either side. Titanium nitride (TiN) was chosen as the metallic layer of the absorber. The design requirements regarding mechanical robustness and vacuum sealing are here discussed in more detail.

Mechanical robustness of the encapsulation

Because of its way of operation the device requires a package that is transparent to the infrared light. A TO5 package is used for this purpose, thus a plastic overmolding is not needed for this device. For this reason, the constraints about the mechanical robustness are more relaxed. In fact, the device does not have to withstand a high pressure loading during the packaging process. A value of one bar was considered as loading pressure requirement. Although the loading pressure is low, a maximum deflection of only 1 μm can be allowed. In fact, if a bigger deflection would occur the optical path of the light would change affecting the proper behavior of the device.

Now that the requirements in terms of maximum load and deflection are identified, it is necessary to calculate the column diameter d, the plate thickness t and the distance between the columns L. The distance L mainly depends on the geometry of device to be encapsulated. In this case, columns can be positioned between the thermocouple bridges. This limits the minimum distance L to about 200 μm. In fact, the absorber design could have

been in such a way that columns could also have been inserted in the absorber area, but this would have decreased the absorber performance. The calculation of the capping layer thickness requires some parameters like the ultimate strength, the Young's modulus and the Poisson's ratio that are defined by the material chosen for the capping layer. SiN is chosen as capping material because it has a rather high tensile strength and a good gas tightness [49, 50].

As showed in chapter 2, the minimum thickness value is chosen between those two values given by the deflection at the center of the plate (Eq. 2.4) and the one calculated with the yield strength criterion (Eq. 2.12). In this case, the deflection criterion leads to a more strict condition on the capping layer thickness than the one related to the yield strength. In particular, Eq. 2.4 leads to a thickness of SiN capping layer of at least 4 μm.

Vacuum sealing

The sensitivity of the device improves by almost a factor of 20 when operated in vacuum, as compared to ambient pressure [45]. This is mainly due to the fact that conductive heat losses cause most of the heat flux to flow from the absorber to the substrate via the air path instead of through the suspension bridge. For this reason an hermetic encapsulation at low pressure is needed. As discussed in chapter 5, the vacuum inside a package depends on the pressure at which the sealing deposition is performed but, most importantly, on the outgassing. In order to address those mechanisms, SiN deposited at high temperature by LPCVD was chosen for both capping and sealing layers. In fact, this material is deposited at a pressure as low as 20 Pa. Furthermore, since the deposition is performed at high temperature (850°C), the deposited layer is much more densified. In fact, when compared to PECVD layers, they usually have a lower hydrogen content, which represents a source of outgassing.

7.3.2 Fabrication

Fabrication of the thermopile detector array is presented in [95]; in Fig. 7.9 a schematic topview of the device is shown. Here we describe in detail only the encapsulation process flow. Since the encapsulation consists of high temperature processing steps, the metal lines are made of a stack of Ti and TiN. A sacrificial layer of TEOS needed for the encapsulation step was deposited by PECVD (see Fig. 7.10a). Trenches for the walls and the columns are etched in the TEOS layer landing on SiN (see Fig. 7.10b). For this etching step DRIE is used. Then, a 1500 nm SiN is deposited by

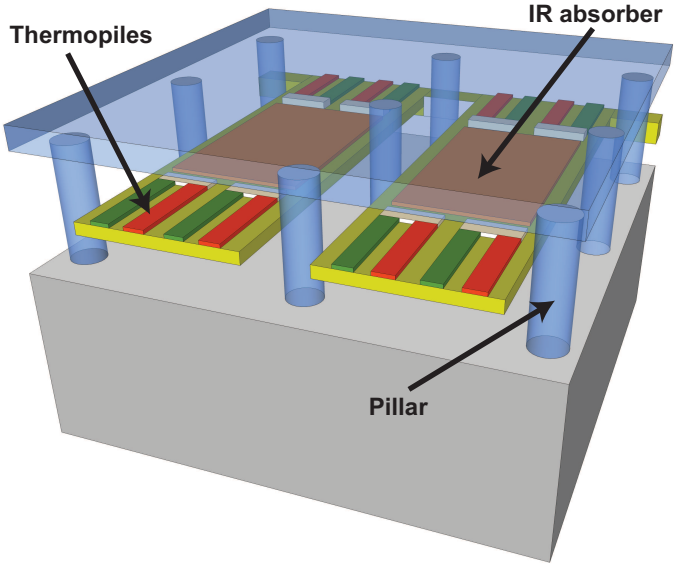

Figure 7.9: Schematic top view of the IR detector.

LPCVD to define the walls and the pillars (see Fig. 7.10c). The access holes are dry etched into the SiN layer landing into the sacrificial layer (see Fig. 7.10d). The sacrificial etching is done to release the packages using a BHF 1:7 solution (see Fig. 7.10e). After sacrificial etching, the wafer was rinsed in IPA. Freeze-drying was performed to avoid sticking of the released structures.

Then the sealing of the sacrificial holes is done by LPCVD SiN in order to achieve high vacuum sealing (see Fig. 7.10f). In order to make the contact opening for the electrical connections with the thermopiles, a dry etching step is then employed. The stack of SiN and TEOS is etched down landing on the Poly-Si. Then Aluminum is deposited by sputtering and it is patterned to define the aluminum pads and interconnections.

7.3.3 Inspection

Preliminary inspections confirmed that the encapsulation process did not affect the working behaviour of the IR device. Further characterization will provide a quantitative evaluation of the benefits of such vacuum sealing on the device sensitivity.

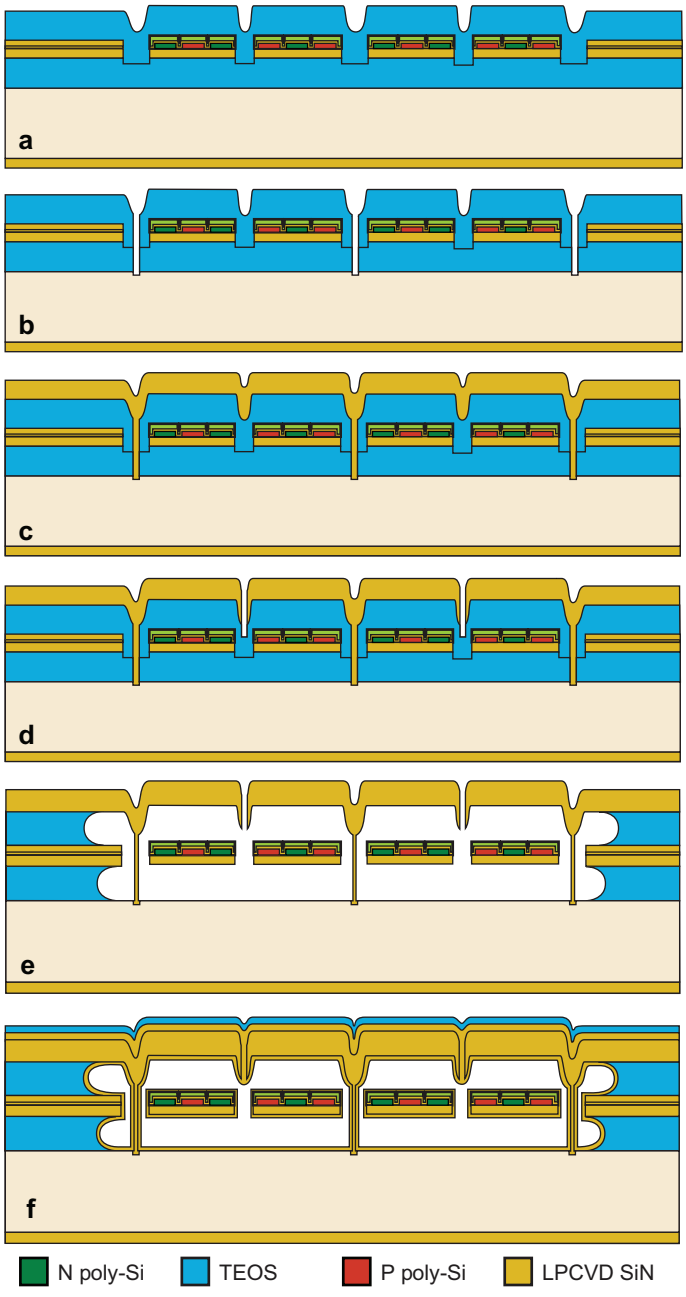

Figure 7.10: Process flow of the fabricated IR detector.

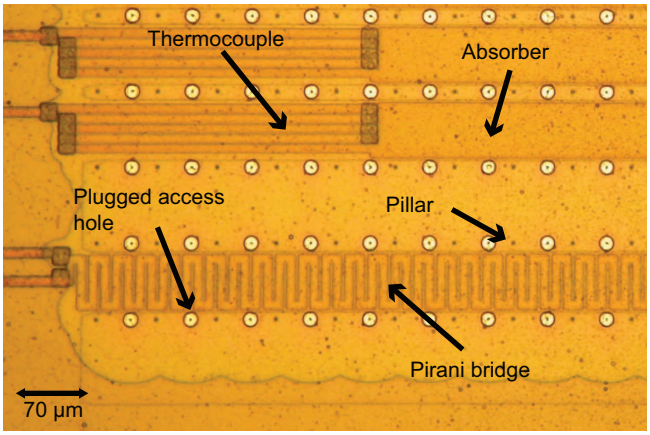

Figure 7.11: Image of the fabricated IR detector.

7.4 Conclusions

In this chapter, two example of process integration of the encapsulation approach were provided. A MEMS electron source and an infra-red detector were used as demonstrators. A SiN thin-film encapsulation process provided the required packaging solution for those devices, showing how the developed thin-film approach can be applied to different applications having different requirements in terms of robustness and hermeticity.

Chapter 8

Conclusions and Recommendations

8.1 Conclusions

It has been shown that although monolithic thin-film encapsulation has several advantages compared with hybrid wafer bonding, mechanical robustness, hermeticity and process integration still remain the main issues to be solved before this approach can actually be extensively used in industry. In this thesis, those issues have been addressed and the main findings are briefly summarized here.

8.1.1 Mechanical Robustness

A model to design MEMS thin-film encapsulation that is sufficiently strong for overmolding is presented. The basic geometry considered for the mechanical model is a flat slab structure supported by columns. For the mechanical dimensioning it was taken into account both the deflection of the capping layer and the stresses in the structure. Different packages based on the presented design were fabricated. The packages differ for the diameter of the columns, the distances between columns and the capping layer thickness. Packages made by high ($> 400°C$) and low ($< 400°C$) temperature encapsulation processes were both fabricated. The packages were pressure tested with different loads up to 12.5 MPa (125 bar). The tests confirm the validity of the mechanical model. Moreover, the packages were carried through wafer thinning, dicing, die-attaching and overmolding, demonstrating that the proposed thin-film encapsulation design is robust enough for

withstanding a commercial first-level packaging process.

8.1.2 Modeling of MEMS Pirani Gauges

A new analytical model for the design of MEMS Pirani gauges operating in constant current mode was developed. This model contains closed-form analytical expressions for the most important performance parameters, such as pressure range, sensitivity, output swing and power consumption. The model is verified with experimental results. Its main benefit is that it provides a rapid insight into the relations between the performance parameters and the design variables, such as length, width, thickness, gap and bias current. The model will therefore be very useful to designers of Pirani gauges who need to trade off the performance against the costs associated with chip area and biasing power.

8.1.3 Tube-shaped Pirani Gauge

A novel micromachined Pirani vacuum gauge with low detection limit but with a strongly reduced footprint was introduced. By employing a tube-shaped geometry buried in the substrate the structural rigidity is increased by approximately 10^4 times compared to a bridge-based Pirani gauge with the same footprint. The Pirani tube has been designed by extending the analytical model to the tube geometry. The largest Pirani gauge is 3 mm long and it has a footprint of only 0.012 mm^2. It shows a pressure range from 0.1 Pa to 0.1 MPa. The maximum sensitivity is 17.5 mV/decade.

8.1.4 Hermeticity Monitoring

The hermeticity of the presented thin film approach was tested by integrating the tube-shaped Pirani gauge inside micro-packages sealed by PECVD SiN. The vacuum level achieved is about 0.7 kPa and it slightly changes over time. PECVD SiN showed good sealing property for thin-film packaging. Combining low detection limit and small footprint, the Pirani tube has been proven to be suitable for in-situ evaluation of MEMS vacuum packaging.

8.1.5 Sealing for Thin Film Encapsulation

A new sealing technique for MEMS thin-film encapsulation was developed. It allows to perform the encapsulation step under arbitrary pressure conditions without unwanted deposition inside the micro-package. This is made possible by means of a capping layer containing thermally actuated valves that close the sacrificial holes before the deposition of the sealing layer. This

technique is compatible with most thin-film encapsulation approaches. Microcavities were designed and fabricated. Deflection measurements versus temperature confirmed the validity of the presented approach.

8.1.6 Examples of Process Integration

Two examples of integration of the presented thin-film encapsulation approach were shown. A MEMS electron source and an infrared detector were chosen to illustrate the capability of the packaging method introduced in this thesis. They have different requirements in terms of robustness, hermeticity and process integration. The encapsulation design is performed together with the design of the MEMS device to be encapsulated. Initial results show how the developed thin-film approach can be successfully applied to MEMS devices for different applications.

8.2 Recommendations

The results presented in this thesis underline the large potential of thin-film encapsulation for MEMS devices. However, further research and development is needed in order to verify its commercialization. Some interesting aspects of this encapsulation approach that merit to be further addressed are indicated in this section.

- An approach for mechanical design and characterization for thin-film encapsulation have been presented in chapter 2; it is based on the use of supporting columns. Although the mechanical robustness has been investigated with respect to overmolding, the influence of other back-end processing steps (such as wafer grinding, dicing and so on) should also be investigated. Furthermore, a statistical reliability analysis should also be performed. In fact, the failure mechanisms is dominated by randomly distributed defects in the materials and hence the fracture properties should be treated statistically. For this reason, an extensive amount of experiments should be carried out.
- The tube-shaped Pirani gauge can be used for the characterization of the vacuum level achieved in thin-film packages using different sealing layers. In this way the outgassing and leakage properties of different materials can be compared.
- Further development is needed when the Pirani tube has to be used as vacuum sensor to address applications areas different than hermeticity monitoring. In this case, in order to use the whole working range of

the sensor effectively a logarithmic amplifier should be employed, if the sensor is operated in constant current mode. In this way a signal is obtained that is linearly proportional to the logarithm of the pressure on the whole range between the noise limits. However, if the constant temperature mode is required, a feedback loop should be implemented to eliminate effects of thermal expansion.

- A new sealing technique for MEMS thin-film encapsulation has been described in chapter 6. It allows to perform the encapsulation step under arbitrary pressure conditions without unwanted deposition inside the micro-package. Since only the behavior principle has been proven in this thesis, additional research is needed to further characterize it. Different layers combinations can be tried to achieve more actuation displacement of the sealing cap. The pressure could be measured by integrating a Pirani gauge inside the micropackages; moreover the gas composition could be evaluated by means of residual gas analysis (RGA) [97–102].

Bibliography

[1] K. Gilleo, *MEMS/MOEMS packaging: concepts, designs, metarials, and processes*, McGraw-Hill, Ed., New York, NY, 2005.

[2] J. Lau, *Advanced MEMS Packaging.* McGraw-Hill, 2010.

[3] T.-R. Hsu, *MEMS packaging.* INSPEC, 2004.

[4] M. Esashi, "Wafer level packaging of MEMS," *Journal of Micromechanics and Microengineering*, vol. 18, no. 7, pp. 1–17, 2008.

[5] N. Miki, "Wafer bonding techniques for MEMS," *Sensors Letters*, vol. 3, no. 4, pp. 263–273, 2005.

[6] F. Theunis, T. Lisec, W. Reinert, J. Bielen, D. Yang, M. de Jongh, and P. Krusemann, "A novel and efficient packaging technology for rf-mems devices," in *Electronic Components and Technology Conference, 2007. ECTC '07. Proceedings. 57th*, 29 2007-june 1 2007, pp. 1239 – 1245.

[7] H.-A. Yang, M. Wu, and W. Fang, "Localized induction heating solder bonding for wafer level mems packaging," *Journal of Micromechanics and Microengineering*, vol. 15, no. 2, p. 394, 2005. [Online]. Available: http://stacks.iop.org/0960-1317/15/i=2/a=020

[8] H. Tilmans, H. Ziad, H. Jansen, O. Di Monaco, A. Jourdain, W. De Raedt, X. Rottenberg, E. De Backer, A. Decaussernaeker, and K. Baert, "Wafer-level packaged rf-mems switches fabricated in a cmos fab," in *Electron Devices Meeting, 2001. IEDM Technical Digest. International*, 2001, pp. 41.4.1 –41.4.4.

[9] B. Lee, S. Seok, and K. Chun, "A study on wafer level vacuum packaging for mems devices," *Journal of Micromechanics and Microengineering*, vol. 13, no. 5, p. 663, 2003. [Online]. Available: http://stacks.iop.org/0960-1317/13/i=5/a=318

[10] L. Lin, "Mems post-packaging by localized heating and bonding," *Advanced Packaging, IEEE Transactions on*, vol. 23, no. 4, pp. 608 – 616, nov 2000.

[11] J. Chae, J. Giachino, and K. Najafi, "Fabrication and characterization of a wafer-level MEMS vacuum package with vertical feedthroughs," *Journal of Microelectromechanical Systems*, vol. 17, no. 1, pp. 193–200, 2008.

[12] A. Jourdain, P. D. Moor, K. Baert, I. D. Wolf, and H. A. C. Tilmans, "Mechanical and electrical characterization of bcb as a bond and seal material for cavities housing (rf-)mems devices," *Journal of Micromechanics and Microengineering*, vol. 15, no. 7, p. S89, 2005. [Online]. Available: http://stacks.iop.org/0960-1317/15/i=7/a=013

[13] H. Tilmans, D. van de Peer, and E. Beyne, "The indent reflow sealing (irs) technique-a method for the fabrication of sealed cavities for mems devices," *Microelectromechanical Systems, Journal of*, vol. 9, no. 2, pp. 206 –217, jun 2000.

[14] T. Thompson, "Building small: notes from a mems watcher," *Chip Scale Review*, 2004. [Online]. Available: http://www.chipscalereview.com

[15] S. Dixon-Warren, "The evolution of three-axis mems inertial sensor packaging size does matter!" *I-Micronews - ADVANCED PACKAGING: 3D IC, WLP & TSV*, September 2009. [Online]. Available: http://www.i-micronews.com

[16] B. Kim, R. Candler, R. Melamud, S. Yoneoka, H. K. Lee, G. Yama, and T. Kenny, "Identification and management of diffusion pathways in polysilicon encapsulation for MEMS devices," in *21st IEEE International Conference on Micro Electro Mechanical Systems*, Tucson, AZ, USA, 2008, pp. 104–107.

[17] H. Guckel and D. Burns, "A technology for integrated transducers." in *3rd Int. Conf. Solid-State Sensors and Actuators (Transducers '85)*, 1985, p. 9092.

[18] R. Legtenberg and H. A. Tilmans, "Electrostatically driven vacuum-encapsulated polysilicon resonators part i. design and fabrication," *Sensors and Actuators A: Physical*, vol. 45, no. 1, pp. 57–66, 1994. [Online]. Available: http://doc.utwente.nl/14372/

[19] C. H. Mastrangelo, R. S. Muller, and S. Kumar, "Microfabricated incandescent lamps," *Applied Optics*, vol. 30, no. 7, pp. 868–873, 1991.

[20] L. Lin, K. M. McNair, R. T. Howe, and A. P. Pisano, "Vacuum-encapsulated lateral microresonators," in *International Conference on Solid-State Sensors and Actuators*, Yokohama, Japan, 1993, pp. 270–273.

[21] B. Stark and K. Najafi, "A low-temperature thin-film electroplated metal vacuum package," *Journal of Microelectromechanical Systems*, vol. 13, no. 2, pp. 147–157, 2004.

[22] D. Reuter, A. Bertz, T. Werner, M. Nowack, and T. Gessner, "Thin film encapsulation of microstructures using sacrificial CF-polymer," in *14th International Conference on Transducers and Eurosensors*, Lyon, France, 2007, pp. 343–346.

[23] K. Leedy, R. Strawser, R. Cortez, and J. Ebel, "Thin-film encapsulated RF MEMS switches," *Journal of Microelectromechanical Systems*, vol. 16, no. 2, pp. 304–309, 2007.

[24] R. He and C.-J. Kim, "On-wafer monolithic encapsulation by surface micromachining with porous polysilicon shell," *Journal of Microelectromechanical Systems*, vol. 16, no. 2, pp. 462–472, 2007.

[25] A. Partridge, A. Rice, T. Kenny, and M. Lutz, "New thin film epitaxial polysilicon encapsulation for piezoresistive accelerometers," in *14th IEEE International Conference on Micro Electro Mechanical Systems*, Interlaken, Switzerland, 2001, pp. 54–59.

[26] R. He and C.-J. Kim, "A low temperature vacuum package utilizing porous alumina thin film encapsulation," in *Micro Electro Mechanical Systems, 2006. MEMS 2006 Istanbul. 19th IEEE International Conference on*, 2006, pp. 126 –129.

[27] R. Candler, W.-T. Park, H. Li, G. Yama, A. Partridge, M. Lutz, and T. Kenny, "Single wafer encapsulation of MEMS devices," *IEEE Transactions on Advanced Packaging*, vol. 26, no. 3, pp. 227–232, 2003.

[28] W.-T. Park, R. Candler, S. Kronmueller, M. Lutz, A. Partridge, G. Yama, and T. Kenny, "Wafer-scale film encapsulation of micromachined accelerometers," in *12th International Conference on TRANSDUCERS, Solid-State Sensors, Actuators and Microsystems*, vol. 2, Boston, MA, USA, 2003, pp. 1903–1906.

[29] P. Helin, A. Verbist, J. De Coster, B. Guo, S. Severi, A. Witvrouw, L. Haspeslagh, H. Tilmans, Y. Naito, K. Nakamura, and K. Onishi,

"A wafer-level poly-sige-based thin film packaging technology demonstrated on a soi-based high-q mem resonator," in *Solid-State Sensors, Actuators and Microsystems Conference (TRANSDUCERS), 2011 16th International*, june 2011, pp. 982 –985.

[30] M. Bartek, J. Foerster, and R. Wolffenbuttel, "Vacuum sealing of microcavities using metal evaporation," *Sensors and Actuators A: Physical*, vol. 61, no. 1-3, pp. 364 – 368, 1997. [Online]. Available: http://www.sciencedirect.com/science/article/pii/S0924424797802907

[31] J. D. Zook, W. R. Herb, Y. Ahn, and H. Guckel, "Polysilicon sealed vacuum cavities for microelectromechanical systems," vol. 17, no. 4, pp. 2286–2294, 1999. [Online]. Available: http://dx.doi.org/doi/10.1116/1.581762

[32] Y. Naito, P. Helin, K. Nakamura, J. De Coster, B. Guo, L. Haspeslagh, K. Onishi, and H. Tilmans, "High-q torsional mode si triangular beam resonators encapsulated using sige thin film," in *Electron Devices Meeting (IEDM), 2010 IEEE International*, dec. 2010, pp. 7.1.1 –7.1.4.

[33] B. Guo, L. Wen, P. Helin, G. Claes, A. Verbist, R. Van Hoof, B. Du Bois, J. De Coster, I. De Wolf, A. Hadi Shahar, Y. Li, H. Cui, M. Lux, G. Vereecke, H. Tilmans, L. Haspeslagh, S. Decoutere, H. Osman, R. Puers, S. Severi, and A. Witvrouw, "Above-ic generic poly-sige thin film wafer level packaging and mem device technology: Application to accelerometers," in *Micro Electro Mechanical Systems (MEMS), 2011 IEEE 24th International Conference on*, jan. 2011, pp. 352 –355.

[34] B. Wang, S. Tanaka, B. Guo, G. Vereecke, S. Severi, A. Witvrouw, M. Wevers, and I. D. Wolf, "Outgassing study of thin films used for poly-sige based vacuum packaging of mems," *Microelectronics Reliability*, vol. 51, no. 9-11, pp. 1878 – 1881, 2011. [Online]. Available: http://www.sciencedirect.com/science/article/pii/S0026271411002216

[35] V. Rajaraman, L. Pakula, H. Yang, P. French, and P. Sarro, "Pecvd silicon carbide surface micromachining technology and selected mems applications," *International Journal of Advances in Engineering Sciences and Applied Mathematics*, vol. 2, pp. 28–34, 2010, 10.1007/s12572-010-0020-9. [Online]. Available: http://dx.doi.org/10.1007/s12572-010-0020-9

[36] M. Shahriar Rahman, M. Chitteboyina, D. Butler, Z. C andelik Butler, S. Pacheco, and R. McBean, "Device-level vacuum packaging for

rf mems," *Microelectromechanical Systems, Journal of*, vol. 19, no. 4, pp. 911 –918, aug. 2010.

[37] J. Zekry, D. Tezcan, J.-P. Celis, R. Puers, C. Van Hoof, and H. Tilmans, "Wafer-level thin film vacuum packages for mems using nanoporous anodic alumina membranes," in *Solid-State Sensors, Actuators and Microsystems Conference (TRANSDUCERS), 2011 16th International*, june 2011, pp. 974 –977.

[38] R. Candler, M. Hopcroft, B. Kim, W.-T. Park, R. Melamud, M. Agarwal, G. Yama, A. Partridge, M. Lutz, and T. Kenny, "Long-term and accelerated life testing of a novel single-wafer vacuum encapsulation for mems resonators," *Microelectromechanical Systems, Journal of*, vol. 15, no. 6, pp. 1446 –1456, dec. 2006.

[39] A. Jourdain, P. De Moor, S. Pamidighantam, and H. Tilmans, "Investigation of the hermeticity of bcb-sealed cavities for housing (rf-)mems devices," in *Micro Electro Mechanical Systems, 2002. The Fifteenth IEEE International Conference on*, 2002, pp. 677 –680.

[40] J. Mitchell, G. Lahiji, and K. Najafi, "An improved performance poly-si pirani vacuum gauge using heat-distributing structural supports," *Microelectromechanical Systems, Journal of*, no. 1, pp. 93 –102, feb. 2008.

[41] J. Chae, B. Stark, and K. Najafi, "A micromachined pirani gauge with dual heat sinks," *Advanced Packaging, IEEE Transactions on*, vol. 28, no. 4, pp. 619 – 625, nov. 2005.

[42] J. Zekry, B. Vandevelde, S. Bouwstra, R. Puers, C. Van Hoof, and H. Tilmans, "Thermomechanical design and modeling of porous alumina-based thin film packages for mems," in *Thermal, Mechanical Multi-Physics Simulation, and Experiments in Microelectronics and Microsystems (EuroSimE), 2010 11th International Conference on*, april 2010, pp. 1 –7.

[43] F. Santagata, J. Zaal, V. Huerta, L. Mele, Creemer, and P. Sarro, "Mechanical design and characterization for mems thin film packaging," *Microelectromechanical Systems, Journal of*, no. 3, june 2011.

[44] F. Santagata, C. Yang, J. Creemer, P. French, and P. Sarro, "Single wafer surface micromachined field emission electron source," in *Micro Electro Mechanical Systems, 2009. MEMS 2009. IEEE 22nd International Conference on*, jan. 2009, pp. 848 –851.

[45] H. Wu, S. Grabarnik, A. Emadi, G. de Graaf, and R. F. Wolffenbuttel, "Characterization of thermal cross-talk in a mems-based thermopile detector array," *Journal of Micromechanics and Microengineering*, vol. 19, no. 7, p. 074022, 2009. [Online]. Available: http://stacks.iop.org/0960-1317/19/i=7/a=074022

[46] S. P. Timoshenko and S. Woinowsky-Kreige, *Theory of Plates and Shells*, McGraw-Hill, Ed., 1959.

[47] A. C. Ugural, *Stresses in Plates and Shells*, McGraw-Hill, Ed., 1999.

[48] F. J. Loss and W. J. O'Donnell, "Circular plates with elastically built-in edges," *Journal of Mechanical Sciences*, vol. 5, pp. 399–413, 1963.

[49] J. G. E. Gardeniers, H. A. C. Tilmans, and C. C. G. Visser, "LPCVD silicon-rich silicon nitride films for applications in micromechanics, studied with statistical experimental design," *Journal of Vacuum Science Technology A: Vacuum, Surfaces, and Films*, vol. 14, no. 5, pp. 2879–2892, 1996.

[50] T. Alan and P. M. Sarro, "A comparative study of the strength of Si, SiN and SiC used at nanoscales," in *Materials Research Society Symposium, 2008, Microelectromechanical Systems - Materials and Devices*, Strasbourg, France, 2008, pp. 241–245.

[51] P. French, P. Sarro, R. Malle, E. Fakkeldij, and R. Wolffenbuttel, "Optimization of a low-stress silicon nitride process for surface-micromachining applications," *Sensors and Actuators A: Physical*, vol. 58, no. 2, pp. 149 – 157, 1997. [Online]. Available: http://www.sciencedirect.com/science/article/pii/S0924424796013970

[52] Q. Li, J. Goosen, F. van Keulen, and J. van Beek, "Gas ambient dependence of quality factor in mems resonators," in *Sensors, 2009 IEEE*, oct. 2009, pp. 1040 –1043.

[53] Q. Li, H. Goosen, F. van Keulen, J. van Beek, and G. Zhang, "Assessment of testing methodologies for thin-film vacuum mems packages," *Microsystem Technologies*, vol. 15, pp. 161–168, 2009, 10.1007/s00542-008-0651-y. [Online]. Available: http://dx.doi.org/10.1007/s00542-008-0651-y

[54] E. Topalli, K. Topalli, S. Alper, T. Serin, and T. Akin, "Pirani vacuum gauges using silicon-on-glass and dissolved-wafer processes for the characterization of mems vacuum packaging," *Sensors Journal, IEEE*, vol. 9, no. 3, pp. 263 –270, march 2009.

[55] J. O'Hanlon, *A user's guide to vacuum technology*, Wiley, Ed., 2003.

[56] K. Khosraviani and A. Leung, "The nanogap pirani - a pressure sensor with superior linearity in an atmospheric pressure range," *J. Micromech. Microeng., IOP*, vol. 19, no. 4, 2009.

[57] ——, "The nanogap pirani - a pressure sensor with superior linearity in atmospheric pressure range," in *Micro Electro Mechanical Systems, 2008. MEMS 2008. IEEE 21st International Conference on*, jan. 2008, pp. 900 –903.

[58] J.-S. Shie, B. Chou, and Y.-M. Chen, "High performance pirani vacuum gauge," *Journal of Vacuum Science Technology A: Vacuum, Surfaces, and Films*, vol. 13, no. 6, pp. 2972 –2979, nov 1995.

[59] B. Chou and J.-S. Shie, "An innovative pirani pressure sensor," in *Solid State Sensors and Actuators, 1997. TRANSDUCERS '97 Chicago., 1997 International Conference on*, vol. 2, jun 1997, pp. 1465 –1468 vol.2.

[60] B. C. S. Chou, Y. Chen, M. Ou-Yang, and J. Shie, "A sensitive pirani vacuum sensor and the electrothermal spice modeling," *Sens. Actuators A, Phys.*, vol. 53, no. 1, p. 273277, 1996.

[61] A. M. Robinson, P. Haswell, R. P. W. Lawson, and M. Parameswaran, "A thermal conductivity microstructural pressure sensor fabricated in standard complementary metal-oxide semiconductor," *Review of Scientific Instruments*, vol. 63, no. 3, pp. 2026 –2029, mar 1992.

[62] O. Paul, A. Haberli, P. Malcovati, and H. Baltes, "Novel integrated thermal pressure gauge and read-out circuit by cmos ic technology," in *Electron Devices Meeting, 1994. IEDM '94. Technical Digest., International*, dec 1994, pp. 131 –134.

[63] B. Stark, Y. Mei, C. Zhang, and K. Najafi, "A doubly anchored surface micromachined pirani gauge for vacuum package characterization," in *Micro Electro Mechanical Systems, 2003. MEMS-03 Kyoto. IEEE The Sixteenth Annual International Conference on*, jan. 2003, pp. 506 – 509.

[64] C. Mastrangelo and R. Muller, "Fabrication and performance of a fully integrated mu;-pirani pressure gauge with digital readout," in *Solid-State Sensors and Actuators, 1991. Digest of Technical Papers, TRANSDUCERS '91., 1991 International Conference on*, jun 1991, pp. 245 –248.

[65] ——, "Microfabricated thermal absolute-pressure sensor with on-chip digital front-end processor," *Solid-State Circuits, IEEE Journal of*, vol. 26, no. 12, pp. 1998 –2007, dec 1991.

[66] B. Stark, J. Chae, A. Kuo, A. Oliver, and K. Najafi, "A high-performance surface-micromachined pirani gauge in summit v trade;," in *Micro Electro Mechanical Systems, 2005. MEMS 2005. 18th IEEE International Conference on*, jan.-3 feb. 2005, pp. 295 – 298.

[67] F. Zhang, Z. Tang, J. Yu, and R. Jin, "A micro-pirani vacuum gauge based on micro-hotplate technology," *Sensors and Actuators A: Physical*, vol. 126, no. 2, pp. 300 – 305, 2006. [Online]. Available: http://www.sciencedirect.com/science/article/pii/S0924424705005947

[68] M. Doms, A. Bekesch, and J. Mueller, "A microfabricated pirani pressure sensor operating near atmospheric pressure," *Journal of Micromechanics and Microengineering*, vol. 15, no. 8, p. 1504, 2005. [Online]. Available: http://stacks.iop.org/0960-1317/15/i=8/a=018

[69] R. Kuljic, J. Chang, N. Jayapratha, T. Dankovic, K. Banerjee, A. Feinerman, and H. Busta, "Microelectromechanical system-based vacuum gauge for measuring pressure and outgassing rates in miniaturized vacuum microelectronic devices," vol. 29, no. 2, p. 02B114, 2011. [Online]. Available: http://dx.doi.org/doi/10.1116/1.3562271

[70] C. H. Mastrangelo, "Thermal applications of microbridges," Ph.D. dissertation, Univ. Calif., Berkeley, 1991.

[71] F. Santagata, E. Iervolino, L. Mele, A. W. van Herwaarden, J. F. Creemer, and P. M. Sarro, "An analytical model and verification for mems pirani gauges," *Journal of Micromechanics and Microengineering*, vol. 21, no. 11, p. 115007, 2011. [Online]. Available: http://stacks.iop.org/0960-1317/21/i=11/a=115007

[72] G. Baker and P. R. Graves-Morris, *Pade' approximants*, C. U. Press, Ed., 1996.

[73] J. M. Gere and S. P. Timoshenko, *Mechanics of Materials*, Chapman and Hall, Eds., 1991.

[74] M. Thirumaleshwar, *Fundamentals of Heat and Mass Transfer*. Pearson Education, 2006.

[75] L. La Spina, A. van Herwaarden, H. Schellevis, W. Wien, N. Nenadovic, and L. Nanver, "Bulk-micromachined test structure for fast and reliable determination of the lateral thermal conductivity of thin films," *Microelectromechanical Systems, Journal of*, vol. 16, no. 3, pp. 675 –683, june 2007.

[76] E. Iervolino, A. v. Herwaarden, and P. Sarro, "Temperature calibration of fast scan calorimeter chips," in *Proc. Eurosensors 2008*, 2008, pp. 773–776.

[77] W. J. Alvesteffer, D. C. Jacobs, and D. H. Baker, "Miniaturized thin film thermal vacuum sensor," *Journal of Vacuum Science Technology A: Vacuum, Surfaces, and Films*, vol. 13, no. 6, pp. 2980 –2985, nov 1995.

[78] F. Santagata, J. Creemer, E. Iervolino, L. Mele, A. van Herwaarden, and P. Sarro, "A tube-shaped buried pirani gauge for low detection limit with small footprint," *Microelectromechanical Systems, Journal of*, vol. 20, no. 3, pp. 676 –684, june 2011.

[79] F. Santagata, E. Iervolino, J. Laros, J. Groeneweg, J. Creemer, A. van Herwaarden, and P. Sarro, "A novel 3-d tube-shaped buried poly-si pirani gauge for extended dynamic range with small footprint," in *Micro Electro Mechanical Systems (MEMS), 2010 IEEE 23rd International Conference on*, jan. 2010, pp. 643 –646.

[80] M. de Boer, R. Tjerkstra, J. Berenschot, H. Jansen, G. Burger, J. Gardeniers, M. Elwenspoek, and A. van den Berg, "Micromachining of buried micro channels in silicon," *Microelectromechanical Systems, Journal of*, vol. 9, no. 1, pp. 94 –103, mar 2000.

[81] K. Oura, *Surface Science, An Introduction.* Springer, 2003.

[82] Q. Li, J. Goosen, J. van Beek, F. van Keulen, and G. Zhang, "Outgassing of materials used for thin film vacuum packages," in *Electronic Packaging Technology High Density Packaging, 2009. ICEPT-HDP '09. International Conference on*, aug. 2009, pp. 802 –806.

[83] G. Meijer and A. v. Herwaarden, *Thermal Sensors.* IOP Publishing, 1994.

[84] Q.-A. Huang and N. K. S. Lee, "Analysis and design of polysilicon thermal flexure actuator," *Journal of Micromechanics and Microengineering*, vol. 9, no. 1, p. 64, 1999. [Online]. Available: http://stacks.iop.org/0960-1317/9/i=1/a=308

[85] C. S. Pan and W. Hsu, "An electro-thermally and laterally driven polysilicon microactuator," *Journal of Micromechanics and Microengineering*, vol. 7, no. 1, p. 7, 1997. [Online]. Available: http://stacks.iop.org/0960-1317/7/i=1/a=003

[86] F. Gao, R. K. Leach, J. Petzing, and J. M. Coupland, "Surface measurement errors using commercial scanning white light interferometers," *Measurement Science and Technology*, vol. 19, no. 1, p. 015303, 2008. [Online]. Available: http://stacks.iop.org/0957-0233/19/i=1/a=015303

[87] J. E. Feldman, J. Z. Wilcox, T. George, D. N. Barsic, and A. Scherer, "Elemental surface analysis at ambient pressure by electron-induced x-ray fluorescence," *Review of Scientific Instruments*, vol. 74, no. 3, pp. 1251 –1254, mar 2003.

[88] W. Cho, T. Ono, and M. Esashi, "Micro proximity electron source with apertured electron window for nanolithography in atmosphere," in *Solid-State Sensors, Actuators and Microsystems Conference, 2007. TRANSDUCERS 2007. International*, june 2007, pp. 1581 –1584.

[89] I.-M. Choi, S.-Y. Woo, and H.-W. Song, "Improved metrological characteristics of a carbon-nanotube-based ionization gauge," *Applied Physics Letters*, vol. 90, no. 2, pp. 023 107 –023 107–3, jan 2007.

[90] B. Ghodsian, M. Parameswaran, and M. Syrzycki, "Gas detector with low-cost micromachined field ionization tips," *Electron Device Letters, IEEE*, vol. 19, no. 7, pp. 241 –243, jul 1998.

[91] F. Haase, P. Detemple, and S. Schmitt, "Electron permeable membranes for mems electron sources," *Sens. Actuators A, Phys.*, vol. 132, no. 1, p. 98103, 2006.

[92] F. Santagata, C. Yang, J. Creemer, P. French, and P. Sarro, "Thin film encapsulation of silicon field emission array," in *EUROSENSORS XXII, Dresden, Germany, 2008.*, September 2008, pp. 625–628.

[93] M. Alves, D. Takeuti, and E. Braga, "Fabrication of sharp silicon tips employing anisotropic wet etching and reactive ion etching," *Microelectronics Journal*, vol. 36, pp. 51–54, 2005.

[94] H. Wu, S. Grabarnik, A. Emadi, G. de Graaf, and R. F. Wolffenbuttel, "A thermopile detector array with scaled te elements for use in an integrated ir microspectrometer," *Journal of Micromechanics and Microengineering*, vol. 18, no. 6, p. 064017, 2008. [Online]. Available: http://stacks.iop.org/0960-1317/18/i=6/a=064017

[95] H. Wu, A. Emadi, P. M. Sarro, G. de Graaf, and R. F. Wolffenbuttel, "A surface micromachined thermopile detector array with an interference-based absorber," *Journal of Micromechanics and Microengineering*, vol. 21, no. 7, p. 074009, 2011. [Online]. Available: http://stacks.iop.org/0960-1317/21/i=7/a=074009

[96] H. Wu, "Mems-based linear thermopile detector arrays for ir microspectrometers," Ph.D. dissertation, TUDelft, 2011.

[97] L. Mele, F. Santagata, G. Pandraud, B. Morana, F. D. Tichelaar, J. F. Creemer, and P. M. Sarro, "Wafer-level assembly and sealing of a mems nanoreactor for in situ microscopy," *Journal of Micromechanics and Microengineering*, vol. 20, no. 8, p. 085040, 2010. [Online]. Available: http://stacks.iop.org/0960-1317/20/i=8/a=085040

[98] W. Kim, Q. Wang, J. Hwang, M. Lee, K. Jung, S. Ham, C. Moon, K. Baeks, B. Ha, and I. Song, "A low temperature, hermetic wafer level packaging method for rf mems switch," in *Electronic Components and Technology Conference, 2005. Proceedings. 55th*, may-3 june 2005, pp. 1103 – 1108 Vol. 2.

[99] W. Kim, Q. Wang, K. Jung, J. Hwang, and C. Moon, "Application of au-sn eutectic bonding in hermetic rf mems wafer level packaging," in *Advanced Packaging Materials: Processes, Properties and Interfaces, 2004. Proceedings. 9th International Symposium on*, 2004, pp. 215 – 219.

[100] Q. Wang, S.-H. Choa, W. Kim, J. Hwang, S. Ham, and C. Moon, "Application of au-sn eutectic bonding in hermetic radio-frequency microelectromechanical system wafer level packaging," *Journal of Electronic Materials*, vol. 35, pp. 425–432, 2006, 10.1007/BF02690529. [Online]. Available: http://dx.doi.org/10.1007/BF02690529

[101] G. Longoni, A. Conte, M. Moraja, and A. Fourrier, "Stable and reliable q-factor in resonant mems with getter film," in *Reliability Physics Symposium Proceedings, 2006. 44th Annual., IEEE International*, march 2006, pp. 416 –420.

[102] S.-J. Ham, B.-G. Jeong, J.-H. Lim, K.-D. Jung, K.-D. Baek, W.-B. Kim, and C.-Y. Moon, "Characterization and reliability verification of wafer-level hermetic package with nano-liter cavity for rf-mems applications," in *Electronic Components and Technology Conference, 2007. ECTC '07. Proceedings. 57th*, 29 2007-june 1 2007, pp. 1127 –1134.

Summary

Many Micro-Electro-Mechanical-Systems (MEMS) require encapsulation, to prevent delicate sensor structures being exposed to external perturbations such as dust, humidity, touching, and gas pressure. An upcoming and cost-effective way of encapsulation is zero-level packaging or thin-film encapsulation. With this method, MEMS are already sealed during wafer processing. Thin-film encapsulation poses a number of challenges, in particular to hermeticity, mechanical robustness, and compatibility with the other fabrication steps. In this thesis, we have worked out the following aspects:

- An analytical model for the strength of pillar-based thin-film encapsulations. The model provides guidelines for design. It is supported by experiments with high pressures and a commercial overmoulding process.
- A tube-shaped Pirani gauge for measuring vacuum levels with a low detection limit and a very small footprint. It consists of a tube-shaped resistor that is buried in the silicon substrate. It can be used to monitor the hermeticity of a thin-film encapsulation in situ. Alternatively, it could be employed as a cost-effective stand-alone sensor in vacuum equipment.
- A new analytical model for micromachined Pirani gauges. This model expresses the pressure range as a closed-form analytical function of the design variables like geometry and biasing. Furthermore it yields simplified expressions for performance parameters such as the sensitivity, output swing and power consumption. The model will be very useful to designers who need to trade off performance against the costs of chip area and biasing power.
- The integration of the tube-shaped Pirani gauge inside micro-packages to test the hermeticity of the presented thin film approach. Packages

containing Pirani tubes have been sealed by PECVD SiN. The vacuum level achieved is about 0.7 kPa and it slightly changes over time. PECVD SiN showed good sealing property for thin-film packaging.

- A new sealing technique for MEMS thin-film encapsulation employing the bimorph effect. It allows to perform the encapsulation step under arbitrary pressure conditions without unwanted deposition inside the micro-package.
- A thin-film encapsulation process, employing LPCVD SiN as the structural layer. Two examples of application of the presented thin-film encapsulation approach were shown. A MEMS electron source and an infrared detector were chosen to illustrate the capability of the packaging method introduced in this thesis.

Samenvatting

Vele Micro-Electro-Mechanische-Systemen (MEMS) hebben encapsulatie nodig om het blootstellen van delicate sensor structuren aan externe perturbaties zoals, stof, vocht, aanraking en gasdruk te voorkomen. Een opkomende en kost-effectieve manier van verpakken is het nulde-niveau verpakken of dunne film encapsulatie. Met deze methode, worden MEMS al afgedicht tijdens de wafer verwerking. Dunne-film encapsulatie heeft een aantal uitdagingen, in het bijzonder de hermeticiteit, de mechanische robuustheid, en de compatibiliteit met andere fabricage stappen. In dit werk, hebben we de volgende aspecten uitgewerkt:

- Een analytisch model voor de sterkte van op pilaar gebaseerde dunne-film encapsulaties. Het model geeft ook richtlijnen voor het ontwerp. Het wordt ondersteund door experimenten met hoge drukken en een commercieel overgiet proces.

- Een naar een buis gevormde Pirani meter voor het meten van vacum niveaus met een lage detectie limiet en een zeer kleine voetafdruk. Het bestaat uit een naar een buis gevormde weerstand welke is begraven in een silicium substraat. Het kan worden gebruikt voor het gadeslaan van de hermeticiteit van een dunne film in situ. Als alternatief, zou het gebruikt kunnen worden als een kost-effectieve en een opzichzelfstaande sensor in vacum apparatuur.

- Een nieuw analytisch model voor micro gefabriceerde Pirani meters. Dit model beschrijft de druk range als een gesloten-form analytische functie van ontwerp variabelen zoals geometrie en voorinstellingen. Verder geeft het model vereenvoudigde uitdrukkingen voor prestatie parameters zoals gevoeligheid, uitgang schommeling en stroomverbruik. Het model zal erg nuttig kunnen zijn voor ontwerpers die behoefte hebben aan een afweging tussen prestatie tegen chip oppervlakte en voorinstelling vermogen.

- De integratie van de naar een buis-gevormde Pirani meter in micro-verpakkingen, om de hermeticiteit van de dunne film benadering te testen. Verpakkingen met Pirani meters worden gesloten met PECVD SiN. Het bereikte vacum niveau is ongeveer 650 Pa en verandert licht over de tijd. PECVD SiN als dunne-film verpakking, toonde een goed sluitende eigenschap.
- Een nieuwe sluit techniek voor MEMS dunne-film encapsulatie gebruikmakende van het bimorf effect. Het laat de encapsulatie stap toe onder willekeurige druk condities, zonder ongewenste depositie in de micro-verpakking.
- Een dunne-film encapsulatie proces, waar LPCVD SiN als de structurele laag wordt toegepast. Twee voorbeelden van toepassingen van de gepresenteerde dunne-film encapsulatie benadering werden gedemonstreerd. Een MEMS elektronen bron en een infrarood detector werden gekozen om de mogelijkheden van de verpakking methode te demonstreren in dit werk.

List of publications

Patents

1. J.F. Creemer, G. Pandraud, F. Santagata. Method of manufacturing a micro unit and micro unit for use in a microscope. no P87953NL00.

Journal Papers

1. F. Santagata, J. Zaal, V. Huerta, L. Mele, J.F. Creemer, and P.M. Sarro. Mechanical design and characterization for MEMS thin-film packaging, Journal of Microelectromechanical Systems, DOI10.1109 JMEMS.2011.217-0817.
2. F. Santagata, E. Iervolino, J.F. Creemer, A. v. Herwaarden, and P.M. Sarro. An analytical model and verification for MEMS Pirani gauges Journal of Micromechanics and Microengineering, 2011, 21, 115007.
3. F. Santagata, J.F. Creemer, E. Iervolino, L. Mele, A. van Herwaarden, and P.M. Sarro. A tube-shaped buried pirani gauge for low detection limit with small footprint, Journal of Microelectromechanical Systems, vol. 20, no. 3, pp. 676-684, june 2011.
4. L. Mele, F. Santagata, G. Pandraud, B. Morana, F.D. Tichelaar, J.F. Creemer and P.M. Sarro. Wafer-level assembly and sealing of a MEMS nanoreactor for in situ microscopy. Journal of Micromechanics and Microengineering, 2010, 20, 85040.
5. L. Mele, F. Santagata, E. Iervolino, M. Mihailovic, T. Rossi, A. T. Tran, H. Schellevis, J.F. Creemer and P.M. Sarro. A molybdenum MEMS microhotplate for high temperature operation, Sensors and Actuators A: Physical, accepted for publication
6. F. Santagata, J.F. Creemer, E. Iervolino, A.W. van Herwaarden, P.M. Sarro. Tube-shaped Pirani Gauge for Hermeticity Monitoring of SiN Thin Film Encapsulation, Journal of Micromechanics and Microengineering, IOP, submitted.

7. F. Santagata, R.H. Poelma, J.F. Creemer and P.M. Sarro. Self-sealing Thin-film Encapsulation of MEMS under Arbitrary Pressure Conditions and Gas Composition, Sensors and Actuators A: Physical, submitted.
8. F. Santagata, J.F. Creemer, B. Morana, T. Alan, G. Pandraud, and P.M. Sarro. An all-in-one nanoreactor for high-resolution microscopy on nanomaterials at high pressures, Journal of Micromechanics and Microengineering, IOP, to be submitted.

Conference Proceedings

1. B. Morana, G. Pandraud, F. Santagata, J.F. Creemer and P.M. Sarro. Stiction-driven self-sealing of surface micromachined channels, 25th IEEE International Conference on Micro Electro Mechanical Systems - MEMS12, 29 Jan- 02 Feb. 2012, Paris, France. IEEE, Piscataway, NJ, USA.
2. J.F. Creemer, F. Santagata, B. Morana,L. Mele, T. Alan, E. Iervolino, G. Pandraud, and P.M. Sarro. An all-in-onenanoreactor for high-resolution microscopy on nanomaterials at high pressures,24th IEEE International Conference on Micro Electro Mechanical Systems - MEMS11, 23-27 Jan. 2011, Cancun, Mexico. IEEE, Piscataway,NJ, USA, pp. 1103-1106.
3. B. Morana, F. Santagata, L. Mele, M. Mihailovic, G. Pandraud, J.F. Creemer and P.M. Sarro. A siliconcarbide MEMS microhotplate for nanomaterial characterization in TEM, 24th IEEEInternational Conference on Micro Electro Mechanical Systems - MEMS 11, 23-27Jan. 2011, Cancun, Mexico. IEEE, Piscataway,NJ, USA, pp. 380-383.
4. E. Iervolino, L. Mele, F. Santagata, A.W. van Herwaarden, W. van der Vlist, J.F. Creemer, P.M. Sarro. Self-cleaning mass calibration of a thermogravimetric device using a thin-film molybdenum. In Technical Digest of the 16th International Solid-State Sensors, Actuators and Microsystems Conference (TRANSDUCERS 2011), Beijing, China, pp. 1038-1041.
5. L. Mele, F. Santagata, E. Iervolino, M. Mihailovic, T. Rossi, A. T. Tran, H. Schellevis, J.F. Creemer and P.M. Sarro. Sputtered molybdenum as conductive material for high-temperature microhotplates. In Technical Digest of the 16th International Solid-State Sensors, Actuators and Microsystems Conference (TRANSDUCERS 2011), Beijing, China, pp. 2690-2693.
6. C. Shen, V.R.S.S. Mokkapati, F. Santagata, A. Bossche and P.M. Sarro. Low temperature encapsulation of nanochannels with water inside. In Technical Digest of the 16th International Solid-State Sensors, Actuators and Microsystems Conference (TRANSDUCERS 2011), Beijing, China, pp. 854-857.
7. J.J.M. Zaal, F. Santagata, W.D. van Driel, G.Q. Zhang, J.F. Creemer and P.M. Sarro. Co-design of wafer level thin film package assembly. In 12th Internat. Conf. on Thermal, Mechanical and Multi-Physics Simulation and Experiments in Microelectronics and Microsystems (EuroSimE 2011), pp. 1-6.

8. F. Santagata, E. Iervolino, J.M.W. Laros, J. Groeneweg, J.F. Creemer, A.W. Herwaarden and P.M. Sarro. A novel 3-D tube shaped buried poly-Si Pirani gauge for extended dynamic range with small footprint. In Y Suzuki and M Wong (Eds.), Proceedings 2010 IEEE 23rd International Conference on Micro Electro Mechanical Systems (MEMS 2010). Piscataway, NJ, USA, pp. 643-646.
9. B. Morana, J.F. Creemer, F. Santagata, C.C. Fan, H.T.M. Pham, G. Pandraud, F.D. Tichelaar and P.M. Sarro. LPCVD amorphous SiCx for free-standing electron transparent windows. In Y Suzuki and M Wong (Eds.), Proceedings 2010 IEEE 23rd International Conference on Micro Electro Mechanical Systems. Piscataway, NJ, USA, pp. 572-575.
10. F. Santagata, C.K.Yang, J.F. Creemer, P. French, and P.M. Sarro. Single wafer surface micromachined field emission electron source. In P.M. Sarro and C. Hierold (Eds.), Proceedings 2010 IEEE 22nd International Conference on Micro Electro Mechanical Systems (MEMS 2009). Piscataway, NJ, USA, pp. 848-851.
11. F. Santagata, L. Mele, M. Mihailovic, B. Morana, J.F. Creemer and P.M. Sarro. Wafer Level Encapsulation Techniques for a MEMS Microreactor with integrated Heat Exchanger. In s.n. (Ed.), Proceedings of IEEE Sensors 2009 Conference, Christchurch (New Zealand), pp. 799-802.
12. F. Santagata, C.K. Yang, J.F. Creemer and P.M. Sarro. Thin-film encapsulation of a silicon field emission electron source. In s.n. (Ed.), Proceedings Eurosensors XXII, Dresden, Germany, pp. 625-628.
13. L. La Spina, V. d'Alessandro, F. Santagata, N. Rinaldi and L.K. Nanver. Electrothermal Effects in Bipolar Differential Pairs. In s.n. (Ed.), IEEE BCTM 2007, Boston, USA, pp. 1-4.

Workshops

1. V.G. Huerta, F. Santagata, L. Mele, M.R. Poot, J.F. Creemer and P.M. Sarro. Mechanical model and characterization of thin-film encapsulation for MEMS. In P French et al (Ed.), Proceedings of the 13th SAFE Workshop of the STW.ICT Conference 2010, pp. 85-88.

Acknowledgments

I am very grateful to many people who have helped me, both directly and indirectly, to complete this dissertation. I know this sound a bit like a cold start but it will make the rest sound much better.

First of all, I want to thank you interested readers who are patient enough to go through this book exploring the results of my PhD research. However, if you are just reading the acknowledgments, do not worry because I want to thank you anyway. After all, it could be that you are reading the acknowledgments because you expect to be thanked. Now, if you are a friend or colleague or a committee member, you will be probably thanked again in few lines. If not, please accept my deepest acknowledgments, because it means that I probably have forgotten to do it, and for this I apologize.

I want to thank my promoter Lina Sarro for the endless support in all ways imaginable. It has been an honor to be one of your Ph.D. students. The joy and enthusiasm you have for research was for me always extremely contagious. You are such a source of inspiration and a rare example to follow. And, most importantly, you are the only person who could make me doing things so happily that most of the time I was forgetting that I did not even want to do them.

I am also very grateful to Fredrik Creemer for his great supervision. I learned a lot during our brainstorming sessions and discussions. Throughout my thesis-writing period, he provided encouragement, sound advice, good teaching, and lots of good ideas. I would have been lost without him.

For this dissertation I would like to thank my committee members for their time, interest, and helpful comments.

I will never forget the people who have shared my same belief (and troubles) in some new crazy projects we were running to: Chun Kay Yang, Luigi Mele, Huaiwen Wen, Rene' Poelma, Jeroen Zaal, Andrea Ingenito, Viktor Gonzales Huerta and Ellen Christopherson, thank you so much also for all the fun.

I would also like to thank the members of the Nanoreactors group,

although I was never "officially" part of it: Fredrik Creemer, Luigi Mele, Gregory Pandraud, Bruno Morana, Tuncay Alan and Jan Cornelis Wolff.

Having the chance to perform research at DIMES does not only mean making use of a high tech facility, but especially having the possibility to access all the valuable experience of the DIMES ICP staff that covers the whole design-fabrication-characterization chain of a device. I owe all of them a lot of thanks. I would like to start with Mario Laros who was always available to help me for any kind of processing related issue, especially during the long evenings in the clean room, during which most of my achievements were reached. And then, Charles de Boer, Alex van den Bogaard, Jan Groeneweg and Wim van der Vlist who among the others were always there to help me right away. The list continues with Koos van Hartmgsveldt, Ruud Klerks, Sebastiaan Maas, Hugo Schellevis, Tom Scholtes, Loek Steenweg, Peter Swart, Wim Tiwon, Robert Verhoeven, Ron van Viersen, Cassan Visser, Jan Warmerdam, Wim Wien, Johannes van Wingerden, Jan Cornelis Wolf, Michiel van der Zwan, and Henk van Zeijl. Thank you all for all your support.

Special thanks also go to the secretarial staff for their excellent administrative support always accompanied with beautiful smiles: Marian Roozenburg, Marysia Lagendijk, Bianca Knot and Rosario Salazar Lozano.

Some people use to surf on Internet during time breaks, I always liked to go around the corridors and have "small" chats. I want to thank those chat mates for wasting part of their time with me talking about everything. Thanks to Aslihan Arslan for showing us the Turkish part of life; Alessandro Baiano is acknowledged for his metaphorical way of speaking, Luigi La Spina for continuing supervising me even after the master thesis just because "it is always a pleasure"; Luigi Mele because this is already the third time that I mention him in these acknowledgments and it is not even the last. Marko Mihailovic for being "Grrrrrrranddddissssssssimo" in anything. Thanks to Daniel Tajari Mofrad and Sten Vollebregt for giving me always political asylum in their office and hosting my PhD countdown on their white-board. Special thanks to Francesco Vitale (alias Fazio Francio) and Andrea Ingenito (alias o'bbalordo) for reminding me how is hunting girls and generally for being so cool. Thank you all for being such very good friends.

I would like to express my gratefulness also to all my colleagues with whom I shared all the pleasant moments, the cakes of the coffee++, the talks on the dimes terrace, the queues in front of the coating track and the chats during the cleanings in the cleanroom: Tao Chen, Yann Civale, Jaber Derakhshandeh, Pablo Estevez, Giuseppe Fiorentino, Negin Golshani, Lei Gu, Olindo Isabella, Vladimir Jovanovic, Ruoxuan Li, Gianpaolo Lorito, Sabrina Magnani, Parastoo Maleki, Thomas Moh, Vahid Mohammad, Car-

oline Mok, Sharma Mokkapati, Sander Paalvast, Amir Sammak, Francesco Sarrubi, Sebastian Sosin, Agata Sakic, Sima Tarashioon, An Tran, Daniel Vidal, Michael Wank, Jia Wei, Joke Westra, Jin Zhang and Theodoros Zoumpoulidis. Thank you all for providing a stimulating and fun environment in which to learn and grow.

One of the biggest achievements during the past four and half years is surely the winning of the football championship. I will never forget the competitiveness, adrenaline and overall the joy that accompany all the matches. And also all the endless discussions we used to have for the coming week during lunch time. Whether those discussions helped me finish this dissertation I do not know, but I want to thank you anyway. Thanks to Marco Spirito, Hooman and Michele Squillante for keeping the goal. Thanks to Mauro Marchetti, Alessandro Baiano, Andrea Ingenito and Marko Mihailovic for their ultimate defense. Thanks to Yann Civale, Marcel, Giacomo and Sadek: even if you are not in the team anymore, your spirit is always with us. Thanks to Gennaro Gentile who even if he never played football before, is still our best striker ever. Breathless thanks to Luigi Mele for running around the field with me. Thanks to Benjamin Mimoun because he cannot do without playing with us and to Daniel Tajari Mofrad for pretending to enjoy the "catenaccio" tactics. Thanks to the latest purchases, Francesco Vitale, Federico Buja, Hugo Perez and Gianpaolo Lorito; thanks for joining the team even if we were in the second division.

Special thanks go to Chenggang Shen, Tao Chen and Rene' Poelma with whom I had the pleasure to share the office.

I am also indebted to Sander van Herwaarden, managing director of Xensor Integration, Delfgauw, and colleagues from that company, for all of our fruitful discussions and vacuum measurements.

For this physical book to appear, I am indebted to Rene Poelma and Sten Vollebregt for translating the summary and the propositions into Dutch.

Many thanks go to all my friends in Italy because I know I could always count on them. Especially thanks to Marco, Sara, Francesco, Romina and Tommaso for bringing here a piece of Naples during their visits.

I would like to thank my family in Italy for all their love and encouragement. Especially my parents Carmela Capuano and Salvatore Santagata and my sister Roberta who always supported me in all my pursuits.

Lastly, and most importantly, I want to thank my wife, Elina, and my son Salvatore, the only persons I can imagine dedicating this book and the rest of my life. I love you.

Biography

Fabio Santagata was born in Naples, Italy, in 1981. He received his Bachelor and Master of Science degree (cum laude) in electronics engineering from the University of Naples Federico II, Italy, in 2005 and 2007, respectively. During his master thesis work he attended the Delft University of Technology, The Netherlands, for working on the self-heating effects in bipolar transistors fabricated in Silicon on Glass technology.

In July 2007 he joined the Faculty of Electrical Engineering, Mathematics and Computer Science, Delft University of Technology, Delft, the Netherlands, where he worked towards the Ph.D. degree within the Laboratory of Electronic Components Technology and Materials, in the Microsystems/MEMS Technology group of P.M. Sarro. His research interests include wafer-level packaging for MEMS devices, micromachined vacuum sensors, microfluidic systems and MEMS microreactors for in situ microscopy.

In November 2011, he was appointed with the Delft University of Technology, working as PostDoc researcher in the Micro/Nano System Integration and Reliability group of Prof. Dr. G.Q. Zhang.

Stellingen

behorende bij het proefschrift

Mechanical Robustness and Hermeticity Monitoring for MEMS Thin Film Encapsulation

Door

Fabio SANTAGATA

Delft, 6 december, 2011

Stellingen

1. Bij het ontwerpen van MEMS moet de inkapseling als een integraal onderdeel van het apparaat worden gezien.

2. Atoomlaag-depositie (ALD) zou een goede barrière tegen uitgassen kunnen vormen voor dunne-laag inkapseling

3. De technologie die in dit proefschrift wordt beschreven is niet beperkt tot MEMS inkapseling, maar kan ook voor andere toepassingen worden gebruikt, zoals zonnecellen en nanoreactoren.

4. In vergelijking met wafer bonding bestaat dunne-laag inkapseling uit meer processtappen, maar kan goedkoper zijn.

5. Een Pirani-buis is een voorbeeld van ‘begraven oppervlakte-microbewerking’ dat aanzienlijk sterkere structuren dan zijn ‘oppervlakte micro-fabricage’ equivalent toelaat.

6. De bereidheid voor het uitvoeren van een zorgvuldige eindige-elementen analyse komt nogal eens voort uit onwil het fenomeen met analytische modellen te bestuderen.

7. Gestructureerde orde en planning leiden niet noodzakelijk tot een efficiënt onderzoek. Immers de evolutie kwam voor uit chaos.

8. Kostuums zijn het kleermakers-equivalent van de glimlach van een baby.

9. Niets is zo langdurig als een tijdelijke oplossing.

10. 'O purpo s'adda cocere cu' l'acqua soja. (De octopus moet met zijn eigen vocht gekookt worden).

Deze stellingen worden opponeerbaar en verdedigbaar geacht en zijn als zodanig goedgekeurd door de promotor Prof. dr. P. M. Sarro.

Propositions

1. In the design of MEMS the encapsulation should be considered as an integral part of the device.

2. Atomic layer deposition (ALD) could represent a good barrier coating against outgassing for thin-film encapsulation.

3. The technology presented in this thesis is not restricted to MEMS encapsulation but can be applied also to other applications, such as solar cells and nanoreactors.

4. Compared to wafer bonding, thin-film encapsulation consists of more processing steps but can be much more cost-effective.

5. A Pirani tube is an example of "buried surface micromachining" that allows significantly stronger structures than their “surface micromachining” equivalent.

6. The willingness of performing a meticulous finite element analysis often derives from the unwillingness of studying the phenomenon by analytical models.

7. Structured order and planning do not necessarily lead to efficient research. After all, evolution came out of chaos.

8. Suits are the sartorial equivalent of a baby's smile.

9. No such thing is as long-lasting as a temporary solution.

10. 'O purpo s'adda cocere cu' l'acqua soja. (The octopus should be cooked with its own fluid).

These propositions are regarded as opposable and defendable, and have been approved as such by the supervisor Prof. dr. P. M. Sarro.

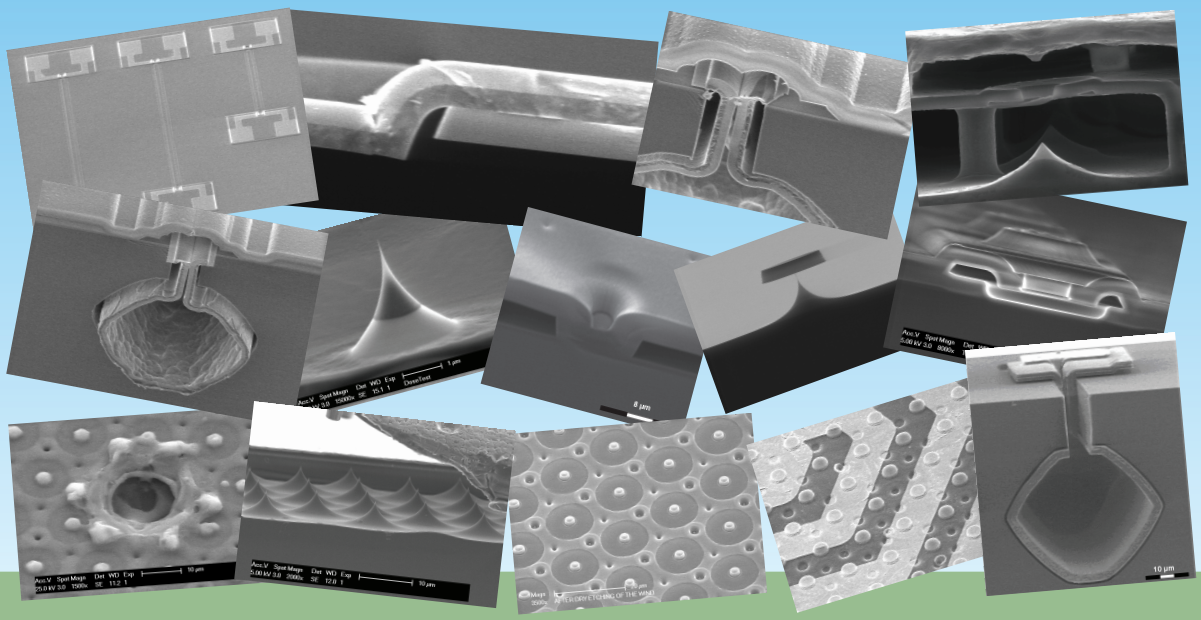

Many MEMS require encapsulation, to prevent delicate sensor structures being exposed to external perturbations such as dust, humidity, touching, and gas pressure. An upcoming and cost-effective way of encapsulation is thin-film encapsulation. With this method, MEMS are already sealed during wafer processing.

Thin-film encapsulation poses a number of challenges in terms of mechanical robustness, hermeticity monitoring and process integration. In this thesis, these issues have been addressed and a new approach for thin-film encapsulation is presented.

TU Delft

dimes